Markus Bainschab, BSc

Multiphoton Ionization Channels in Molecules Investigated by Photoelectron-Photoion-Coincidence Spectroscopy

MASTER'S THESIS

to achieve the university degree of

Diplom-Ingenieur

Master's degree programme: Technical Physics

submitted to

Graz University of Technology

Supervisor

Ass.Prof. Dipl-Ing. Dr.techn. Markus Koch

Institute of Experimental Physics

Graz, June 2016

AFFIDAVIT

I declare that I have authored this thesis independently, that I have not used other than the declared sources/resources, and that I have explicitly indicated all material which has been quoted either literally or by content from the sources used. The text document uploaded to TUGRAZonline is identical to the present master‘s thesis.

Date

Signature

Abstract

An ultrafast femtosecond laser pump-probe setup is used to study photoinduced molecular relaxation and ionization dynamics. Molecules in gas phase are multiphoton-ionized inside a spectrometer. Time-of-flight measurements provide information about ion masses and the kinetic energies of electron. For the electron detection a magnetic bottle scheme is applied. The spectrometer allows us to detect the ions and electrons of the same ionization events which is the novelty of this work. Using the PhotoElectron-PhotoIon-COincidence (PEPICO) method allows to associate ions of a certain mass with their electron spectra. This gives a deeper insight on the ionization process compared to the separate detection of ions and electrons. The photoion and photoelectron spectra were characterized and calibrated using noble gas atoms. A software for processing and analyzing the PEPICO data was implemented. The PEPICO setup and software were tested by comparing our data to recently published results on n-butane. Above-threshold-ionization (ATI) experiments on acetone and perylene were performed using 800 nm laser pulses. Multiphoton ionization measurements on acetone using 400 nm and 266 nm pulses reveal two different ionization channels. One channel yielding the unfragmented parent ion and the other one leading to fragmentation. The performed experiments show the strengths of PEPICO in investigating molecular dynamics and fragmentation behaviors.

Kurzfassung

Mithilfe eines Femtosekundenlaser-Pump-Probe-Setups werden photoinduzierte Relaxationsdynamiken in Molekülen untersucht. Moleküle in Gasphase werden im Spektrometer multiphotonenionisiert. Flugzeitmessungen geben Informationen über die Masse der Ionen und die kinetische Energie der Elektronen. Für die Elektronendetektion wird ein Magnetic Bottle Setup angewandt. Mithilfe des Spektrometers ist es möglich Ionen und Elektronen desselben Ionisationsevents zu detektieren, worin die Novität dieser Arbeit besteht. Durch die PhotoElectron-PhotoIon-COincidence (PEPICO) Methode werden Ionen einer bestimmten Masse mit Elektronen Spektren in Verbindung gebracht. Dies ermöglicht einen tieferen Einblick in den Ablauf des Ionisationsprozesses als durch die getrennte Detektion von Ion und Elektronen. Die Ionen- und Elektronenspektren wurden mithilfe von Edelgasen charakterisiert und kalibriert. Der PEPICO Aufbau und die Software wurden getestet, indem Daten von Experimenten an n-Butan mit Ergebnissen aktueller Publikationen verglichen wurden. Es wurden Above-Threshold-Ionization (ATI) Experimente, wobei Aceton und Perylen mit 800 nm Pulsen ionisiert wurden, durchgeführt. Multiphotonenionisations-Experimente mit 400 nm und 266 nm Pulsen an Aceton zeigen die Präsenz zweier Ionisationskanäle. Der eine Kanal führt zur Fragmentation des Moleküls, beim anderen liegt das geladene Ausgangsmolekül vor. Die durchgeführten Experimente veranschaulichen die Stärken der PEPICO Methode beim Untersuchen von Molekulardynamiken und Fragmentationsverhalten.

Contents

Introduction

Ultrafast laser spectroscopy has been a very intensively studied field of research for more than two decades now. Ultrashort laser pulses are used to study dynamics on very short time scales. New insights on the processes at these short timescales led to the Nobel Prize for Ahmed H. Zewail "for his studies of the transition states of chemical reactions using femtosecond spectroscopy" in 1999. There is a variety of methods which are applied for these investigations. Time-resolved photoelectron spectroscopy (TRPES) and time-resolved photoion spectroscopy (TRPIS) are very common among them. A molecule is excited by a pump pulse and ionized by a probe pulse. The electron energy spectra or ion mass spectra for different time delays between pump and probe pulse build up a picture how the molecule relaxes over time.

In continuous wave single photon ionization experiment the fragmentation dynamics of molecules depending on the amount of energy deposited in the molecules is studied using the PhotoElectron-PhotIon-COincidence (PEPICO) method and vacuum ultraviolet radiation provided by synchrotrons or other sources. Experiments with this technique have been done since the 1960s. The combination of times-of-flights of electrons and ions provides insights on the dissociative ionization processes. The ion spectra show the fragmentation behavior and the correlated photoelectron spectra provide information about the ionization channel.

The combination of ultrafast laser spectroscopy and the PEPICO method is a very promising approach to obtain a comprehensive picture of molecular dynamics and fragmentation processes on a femtosecond time scale. The setup including a femtosecond laser system and a time-of-flight spectrometer characterized and applied within this thesis has been used to perform experiments that show the power of this combination. The investigations discussed within this work were done with single pulse experiments. Time resolved pump-probe experiment are covered within the master's thesis of Paul Maierhofer [1].

CHAPTER 1

Fundamentals

1.1 Multiphoton Ionization (MPI)

By absorbing multiple photons an atom can be ionized despite the energy of a single photon $\hbar\omega$ is lower than the ionization potential IP. This is schematically illustrated in figure 1.1. The absorption of N photons corresponds to N-th order perturbation theory. The kinetic energy E_{kin} of the liberated electron is:

$$E_{kin} = N\hbar\omega - IP \tag{1.1}$$

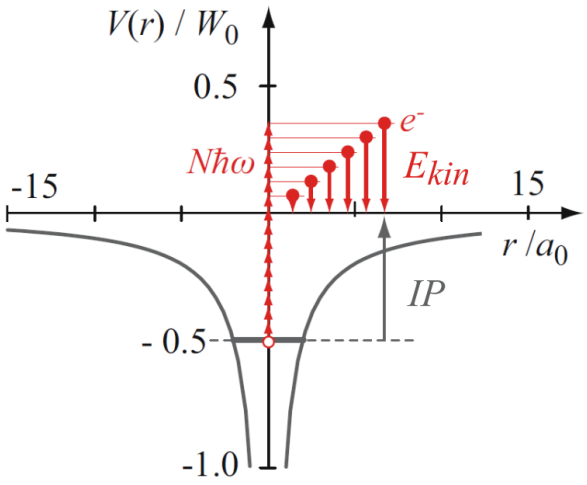

Figure 1.1: Illustration of 800 nm multiphoton ionization of hydrogen. Figure taken from [2].

The transition rate $R^{(N)}_{k_\epsilon \leftarrow a}$ of the bound initial state $|a\rangle$ to the continuum state $|\epsilon\rangle$ can be described as [2]:

$$R^{(N)}_{k_\epsilon \leftarrow a} = \sigma^{(N)}\Phi^N \propto I^N \tag{1.2}$$

with the photonflux $\Phi = I/\hbar\omega$, the generalized cross section $\sigma^{(N)}$ and N the order of the process. The slope in a double logarithmic plot (yield with respect to power ($P \propto I$)) gives the order of the ionization process (number of photons).

$$\log\left(R^{(N)}_{k_\epsilon \leftarrow a}\right) = N \cdot \log(I) + const. \tag{1.3}$$

1.1.1 Ponderomotive Potential

The force on a free electron in an oscillating electric field is given by the following equation:

$$m_e \frac{\mathrm{d}v}{\mathrm{d}t} = eE_0 \cos \omega t \tag{1.4}$$

m_e... electron mass ($9.11 \cdot 10^{-31}$ kg)

e... electron charge ($1.60 \cdot 10^{-19}$ C)

E_0... amplitude of the oscillating electric field

ω... oscillation frequency of the electric field

The velocity of the electron is:

$$v\,(t) = \frac{eE_0}{m_e \omega} \sin \omega t \tag{1.5}$$

This yields the following term for the kinetic energy:

$$\frac{1}{2} m_e v^2 = \frac{e^2 E_0^2}{2 m_e \omega^2} \sin^2 \omega t \tag{1.6}$$

The mean energy in this quiver motion is called ponderomotive potential (U_p):

$$U_p = \overline{\frac{1}{2} m_e v^2} = \frac{e^2 E_0^2}{4 m_e \omega^2} \tag{1.7}$$

This can be written as a function of the intensity I and the wavelength λ.

$$U_p = \frac{e^2 I \lambda^2}{8 \pi^2 \epsilon_0 c^3 m_e} \propto I \lambda^2 \tag{1.8}$$

The intensity of a focused femtosecond laser pulse can be very high ($\approx 10^{14} \frac{\mathrm{W}}{\mathrm{cm}^2}$). The wavefunctions and the term energies of bound electrons show severe changes in these strong laser fields. The ponderomotive potential has to be compared with the binding energy of the electron in atom. In moderate fields a shift of the term energies appears. For very high and long-wave laser fields the picture of bound states collapses. The system gets highly relativistic if $U < m_e c^2$ and the electric field exceeds the atomic field E_H (field which an electron in a H-atom at a distance of a_0 is attracted by) for intensities higher than I_H:

$$I_H = \frac{\epsilon_0 c}{2} E_H^2 = \frac{\epsilon_0 c}{2} \left(\frac{e}{4 \pi \epsilon_0 a_0^2} \right)^2 \tag{1.9}$$

1.1.2 Keldysh Parameter

The Keldysh parameter γ characterizes a transition from a situation *atom with laser field* ($\gamma > 1$) to a situation *laser field with atom* ($\gamma < 1$). It is defined as a function of the ponderomotive potential U_p and the ionization potential IP:

$$\gamma = \sqrt{\frac{IP}{2U_p}} = \sqrt{\frac{\epsilon_0 c m_e \omega^2 IP}{e^2 I}} \propto \sqrt{\frac{IP}{I\lambda^2}} \tag{1.10}$$

The Keldysh parameter γ decreases with increasing intensities I. When the atomic energy is comparable to the energy provided by the laser field the Keldysh parameter is close to unity ($\gamma \approx 1$).

1.1.3 Tunnel Ionization

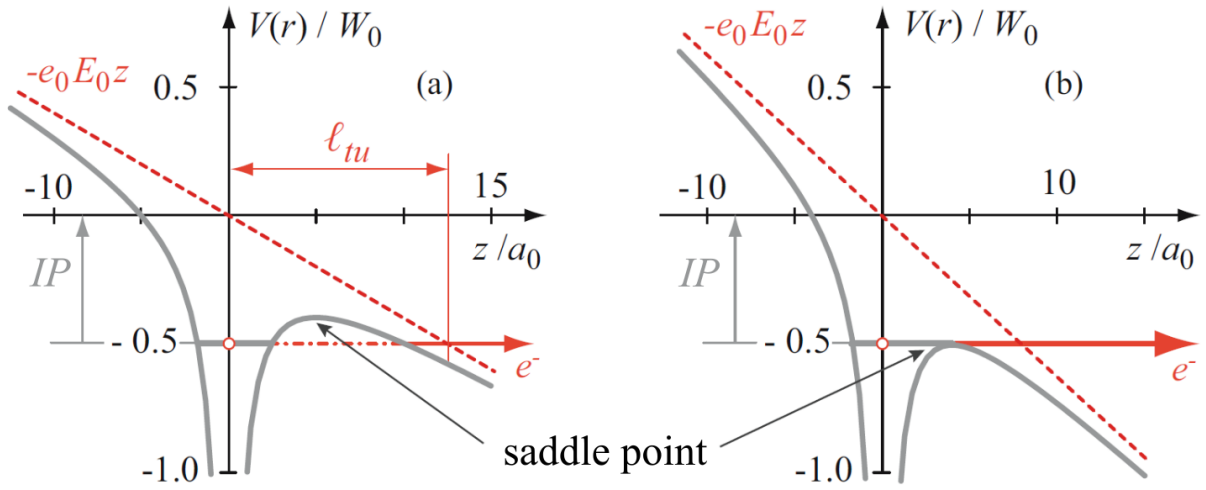

Figure 1.2: Model of the strong field ionization of an atom. Cut through the potential energy surface parallel to the direction of the $\vec{E}$-field at the moment the z-component of the field is maximal. **(a)**: tunnel process **(b)**: *"above-barrier"* electron emission. Figure taken from [2].

The atomic electric field can be severely influenced by high external (oscillating) electric fields. The electron of an atom (atomic number Z) in the field of a z-polarized laser pulse "feels" the following time dependent potential:

$$V(r,t) = \frac{-Ze^2}{4\pi\epsilon_0 r} - eE(t)\,z \tag{1.11}$$

This potential is depicted in figure 1.2 for the maximum of the oscillation. Tunnel ionization (**a**) or *"above-barrier"* electron emission (**b**) may occur. The saddle point of the

potential has to be as low as the negative ionization potential ($V = -IP$) for the *"above-barrier"* emission. Typical intensities to fulfill this requirement are $I \approx 10^{14} \frac{\mathrm{W}}{\mathrm{cm}^2}$. These intensities can be reached by focusing femtosecond laser pulses. For the tunneling process it is essential that the tunneling time is shorter than half the oscillation period ($t_{tu} < \frac{1}{2\omega}$). This criterion can help to quantify the transition to the tunneling regime. With the term for the tunneling time

$$t_{tu} = \sqrt{\frac{\epsilon_0 c m_e IP}{4e^2 I}} \tag{1.12}$$

the Keldysh parameter can be defined as

$$\gamma = 2\omega t_{tu} = \sqrt{\frac{\epsilon_0 c m_e \omega^2 IP}{e^2 I}} \tag{1.13}$$

in agreement with equation 1.10.

1.1.4 Transition from MPI to Tunnel Ionization

There is a gradual transition between the regime of moderate intensities where multi-photon ionization appears and perturbation theory applies and the regime of very high laser fields where tunnel ionization and a massive shift of the term energies due to the ponderomotive potential is observed. An experiment by Larochelle et al. [3] shows this transition very well. Xenon ($IP = 13.44\,\mathrm{eV}$) was ionized using $800\,\mathrm{nm}$ ($\hbar\omega = 1.55\,\mathrm{eV}$) femtosecond laser pulses. Nine photons ($\frac{IP}{\hbar\omega} = 8.67$) are needed for the ionization. So a slope of $N = 9$ is expected in a double logarithmic plot (ion yield as a function of the intensity), which is depicted in figure 1.3.

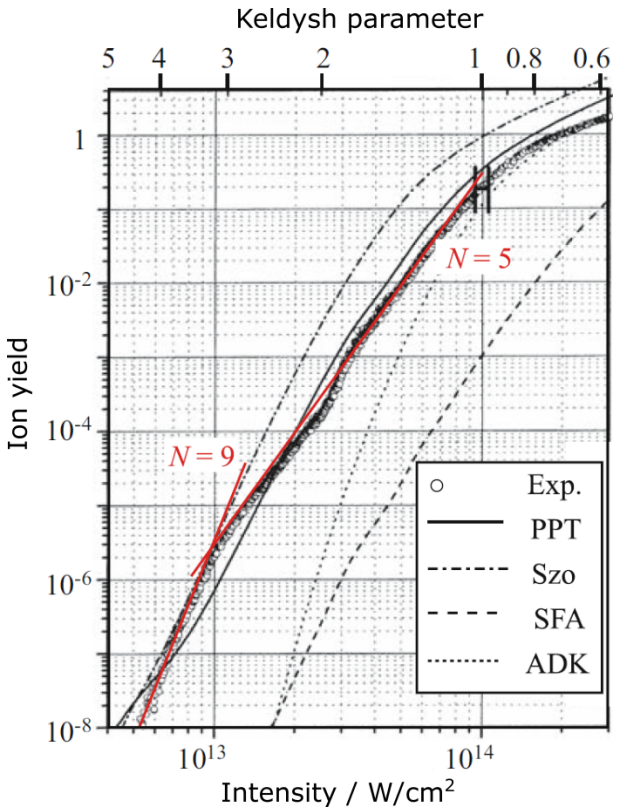

Figure 1.3: 800 nm multiphoton ionization of xenon. Double logarithmic plot of the ion yield with respect to the intensity. The horizontal axis on the top of the plot shows the Keldysh parameter. The experimental data is compared with different theories. Figure taken from [3]

The expected slope of $N = 9$ can be observed at low intensities. Going to higher intensities the experimental data is very well approximated by a slope of $N = 5$. Five photons are needed to populate the first excited state of xenon. When the intensity is high it is obviously sufficient to make this first excitation step. The excited state ionizes with a very high probability. The process of a resonant absorption of a single or multiple photons and a sequential ionization is called resonant enhanced multi photon ionization (REMPI). At intensities higher than $10^{14}\ \frac{\mathrm{W}}{\mathrm{cm}^2}$ the slope decreases dramatically. All atoms in the laser focus are ionized. The increase of the signal is caused by an enlargement of the effective ionization volume. The saturation regime is reached at a Keldysh parameter of $\gamma \approx 1$.

1.1.5 Above Threshold Ionization (ATI)

When an atom or a molecule is ionized with a larger number of photons than energetically required one speaks of above threshold ionization. This usually happens when the Keldysh parameter is close to unity. In this regime the ponderomotive potential can not

be neglected. The kinetic energy of the electron is:

$$E_{kin} = N\hbar\omega - IP - U_p \tag{1.14}$$

Energy from electromagnetic radiation can only be transferred to an electron near a core as a consequence of momentum conservation. The absorption of different numbers of photons leads to the equidistant peaks in figure 1.4. When an electron is separated from an atom by a strong field it can return to the atom. This happens if the sign of the oscillating field reverses when the electron is still close to the atom. The maximum energy of these rescattered electrons is $3.17 \cdot U_p$ (marked with black arrows in figure 1.4) as calculations show. In ATI spectra kinetic energies are measured up to a cutoff at $10 \cdot U_p$ [4,5]. The existence of these high energy electrons can be interpreted as photon absorption near the core after the rescattering process although this is a very simple classical picture for a very complex process.

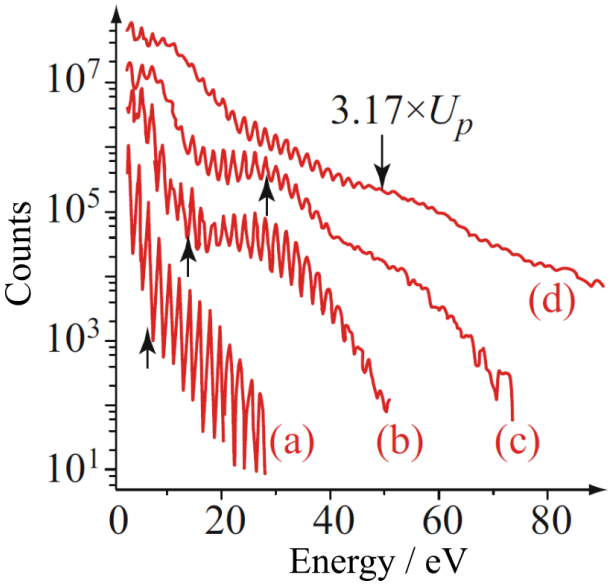

Figure 1.4: ATI spectra from argon ionized with 40 fs, 630 nm pulses. The intensities are: $6 \cdot 10\,\frac{\mathrm{W}}{\mathrm{cm}^2}$ (a), $1.2 \cdot 10\,\frac{\mathrm{W}}{\mathrm{cm}^2}$ (b), $2.4 \cdot 10\,\frac{\mathrm{W}}{\mathrm{cm}^2}$ (c), and $4.4 \cdot 10\,\frac{\mathrm{W}}{\mathrm{cm}^2}$ (d). Figure taken from [4].

1.2 Fragmentation upon Multiphoton Ionization

The mass spectrum of a gaseous specimen can be determined using multi photon ionization and time-of-flight measurements as described in section 2.3. Molecules can fragment upon multi photon ionization so the spectrum often not only shows a peak at the mass corresponding to unfragmented parent molecules but also peaks at lighter masses that are assigned to fragments. The fragmentation behavior of molecules and the involved ionization channels are extensively studied topics of current research. Photoelectron-photoion-coincidence (PEPICO) detection (described in section 2.4) is a very suitable method for this topic. Photoelectron spectra provide information about the ionization channel and ion spectra show the fragmentation behavior. The coincidence detection allows to obtain a deep insight on the processes that lead to ionization and fragmentation. Fragmentation upon multiphoton ionization can be triggered by different processes:

- **Direct population of a dissociative ionic state**
  If the ionic state which is populated upon ionization is not stable, the ion fragments. Experiments on n-butane [6] show that the fragmentation behavior depends on which ionic state is populated. Theses experiments are described in detail in section 3.1.

- **Subsequent resonant population of an excited ionic state**
  Fragmentation can be caused by ionization to the ionic ground state and the subsequent resonant population of an excited ionic state. The molecule is ionized with the energy of a certain number of photons. The ion is in a stable state. A dissociative excited ionic state can be populated by the resonant absorption of an additional photon which which provides enough energy to overcome the dissociation energy [7]. Note that the corresponding electron's kinetic energy is the one which is determined by the initial MPI into the stable state. Photoelectron-photoion-coincidence (PEPICO) detection allows to associate ion masses with electron energy bands. Energy bands which appear in both the spectrum corresponding to the parent ion and the spectrum corresponding to a fragment ion are ascribed to the subsequent resonant population of an dissociative ionic state. Bands which only appear in the fragment spectrum are assigned to the direct population of a dissociative ionic state described above [8, 9].

- **Deposition of vibrational energy in the course of relaxation dynamics**
  An electronically excited state of a molecule is resonantly populated by single or multi photon transition. The minimum energy geometry of this excited state in

general differs from the ground state geometry. A geometry relaxation takes place. In the course of this relaxation electronic energy is converted into vibrational energy. If this energy is stored in vibrations that facilitate fragmentation, like a C-C bond stretch in acetone (described in detail in section 3.2.1), the molecule is very likely to fragment upon the ionization by an additional photon. The ion is in an electronic state that is stable in the vibrational ground state but in the excited vibrational state it is dissociative. The influence of the ionization pulse duration on this effect is discussed in section 1.2.

- **Dissociation in a neutral, excited state**
  Molecules can fragment without being ionized as a consequence of (multi) photon excitation into a neutral dissociative state or excitation into a stable state and subsequent intersystem crossing in a dissociative state. One example for this process is the Norrish type I reaction which is a photoinduced neutral dissociation of aldehydes and ketones. A photon is absorbed by the carbonyl group which yields a population of a singlet state. A triplet state is populated by intersystem crossing. A C-C bond break yields two radical fragments [10]. The neutral radicals can be ionized by additional photons and appear in the time-of-flight mass spectrum. A dissociation in a neutral, excited states results in a PEPICO electron energy band that only appears in the spectrum corresponding to the fragment.

To understand ionization and fragmentation processes it is essential to know whether the fragmentation happens in the neutral or the ionic state. PEPICO detection provides information about in which state the molecule fragments. The information which electron energy band correlates with which ion is not accessible if electrons and ions are not detected in coincidence. This information is crucial to distinguish between different fragmentation processes [8, 9].

The investigations discussed within this work were done with single pulse experiments. Time resolved pump-probe experiment are covered within the master's thesis of Paul Maierhofer [1].

The influence of the pulse duration on the ionization process has been studied in recent experiments [11]. CH_2IBr, CH_2BrCl, and C_6H_5 have been ionized with femtosecond laser pulses. A shortening of the pulse from about 40 fs to less than 10 fs causes a dramatic change in the photoelectron spectrum. For pulse durations below 10 fs the vibrational dynamics of the ionized molecule is frozen. This is called the impulsive limit. An example

for the dependence of the spectrum on the pulse duration is depicted in figure 1.5.

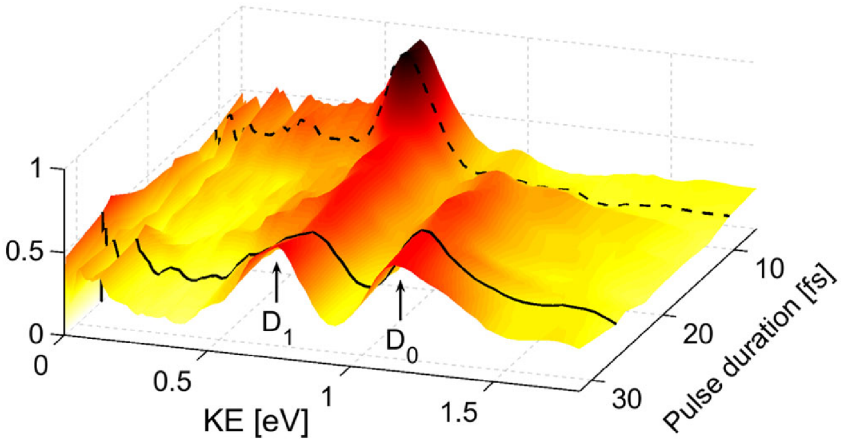

Figure 1.5: Photoelectron spectra [yield vs photoelectron kinetic energy (KE)] for ionization CH_2IBr with different pulse durations. Figure taken from [11].

The photoelectron spectrum of CH_2IBr ionized with 30 fs pulses shows two major peaks. These peaks are assigned to the first two states of the molecular cation (D_0 and D_1). Vibrational dynamics and nonadiabatic coupling between resonant intermediate states lead to both ionic states being populated. For pulse durations shorter than 12 fs the D_1 peak becomes dominant and the D_0 peak diminishes. Here the pulse is shorter than the time scale for the molecular dynamic so only a single ionic state is populated.

CHAPTER 2

Apparatus

2.1 Components of the Experimental Setup

In this section an overview of the experimental setup and its components is given. The ways of operating the setup and the influences of the components on the spectra are described in the sections 2.2, 2.3 and 2.4.

2.1.1 Optical Setup

The optical setup used is depicted schematically in figure 2.1. A commercial laser system is used (Coherent Vitara oscillator and Legend Elite Duo amplifier) which produces 25 fs pulses with a center wavelength of 800 nm. The repetition rate is 3 kHz and the pulse energy is 4.3 mJ. The beam is split into two paths. One of them includes a delay stage. This makes time resolved pump-probe experiments possible. The measurements for this thesis are based on ionization from the ground state and therefore do not make use of the two beam paths and the delay stage. The optical setup and time resolved experiments are described in detail within the thesis of Paul Maierhofer [1]. The output frequency can be doubled or tripled using BBO crystals.

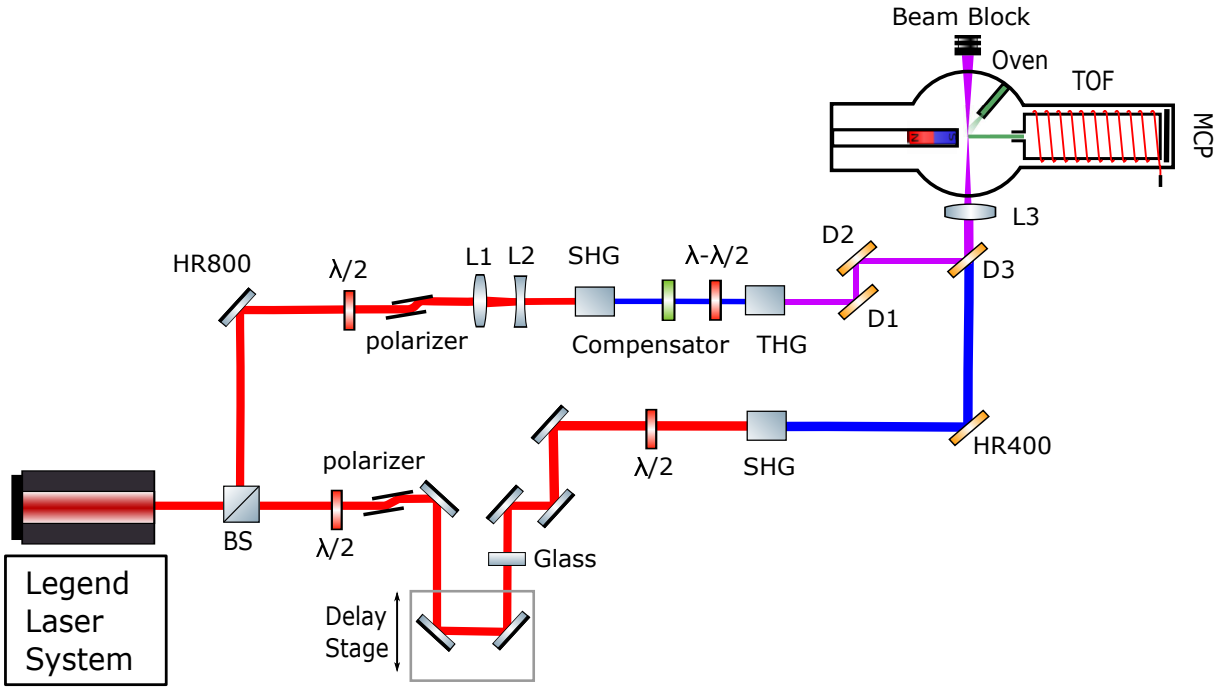

Figure 2.1: Sketch of the optical setup used for the experiments. The setup and its components are described in detail within the master's thesis of Paul Maierhofer [1]

2.1.2 Spectrometer

The spectrometer was designed by Markus Koch. A picture of and a drawing of the spectrometer is shown in figure 2.2. It includes the following components:

- **Drift tube**:
  The drift tube is used for time-of-flight measurements that give information about the mass-to-charge ratio of ions and the kinetic energy of electrons. The tube has a length of $\approx 56\,\mathrm{cm}$. It is surrounded by a solenoid which provides a magnetic field for the magnetic bottle scheme described in section 2.1.5. The solenoid is covered with a mu-metal plate to shield the earth's magnetic field.

- **Micro channel plate (MCP) detector**: At the end of the drift tube there is a MCP detector which detects ion and electron hits. It is described in detail in section 2.1.3.

- **Repeller**: The repeller (light blue part in figure 2.2, photo in figure 2.9) is a copper stick with a stack of neodymium magnets which provide a strong magnetic field for the magnetic bottle setup (section 2.1.5). Depending on the voltage applied to the repeller either ions ($\approx +2\,\mathrm{kV}$) or electrons ($\approx -3\,\mathrm{V}$) are pushed into the flight tube.

A high voltage switch which is described in section 2.1.4 allows to detect ions and electrons in coincidence.

- **Oven (optional)**: There is the possibility of installing an oven to evaporate solid specimen. The oven is described in detail within the bachelor's thesis of Franz Koberg [12].
- **Quadrupole mass spectrometer QMS**: The Pfeiffer Vacuum Prisma Plus QMS allows to take mass spectra of the investigated specimen using impact ionization.
- **Vacuum pumps**: A scroll pre vacuum pump and two turbomolecular pumps provide ultra high vacuum conditions ($5{\cdot}10^{-10}$ mbar).
- **Dosing Valve**: Gaseous specimen are measured as background gas and are introduced into the chamber via a dosing valve.
- **Pressure Gauge**: A combined Bayard Alpert hot cathode ionization and Pirani measurement system (PBR 260 Compact FullRange^{TM}BA Gauge) is used to measure the pressure inside the vacuum chamber. It can be used in the pressure range $(5 \cdot 10^{-10} - 1000)$ mbar.

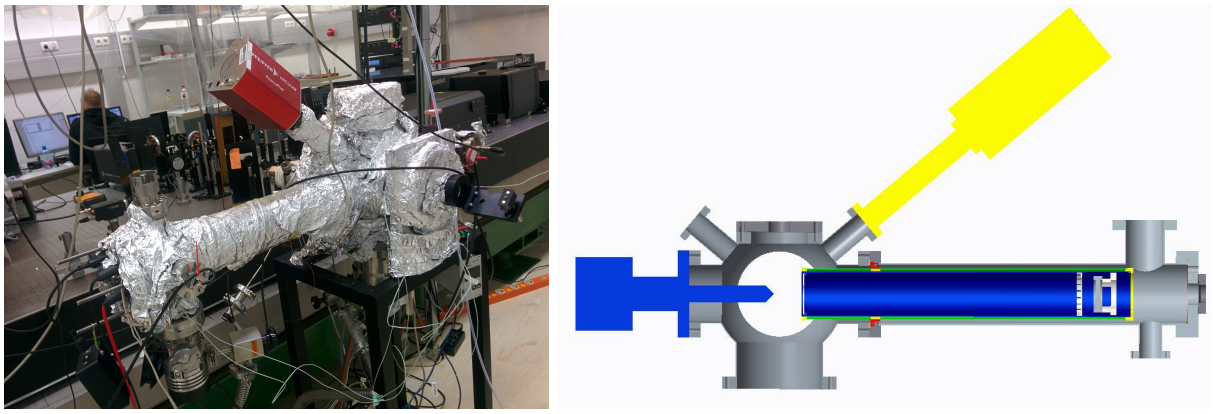

Figure 2.2: Left: Picture of the spectrometer. It is wrapped with aluminum foil for bake out. **Right:** CAD drawing of the spectrometer. Vertical cut along the flight tube. The light blue part is the repeller and its manipulator. The mu-metal plate is the green part surrounding the flight tube. at the and of the tube there is the detector and a mesh in front of it. The yellow part is the QMS.

2.1.3 Detector

A micro-channel plate (MCP) detector with a phosphor screen is used to detect electrons and ions at the end of the flight tube. A drawing of the detector is depicted in figure 2.3.

The electric signal is visualized at a scope or it is digitized using a high-speed digitizer (Gage Cobra,Dynamic Signals LLC). The detector is a so called chevron MCP. It consists of two MCPs with angled channels rotated 180° from each other forming a chevron shape. This arrangement gives the chevron MCP the advantage of much more gain than a single MCP at a given voltage.

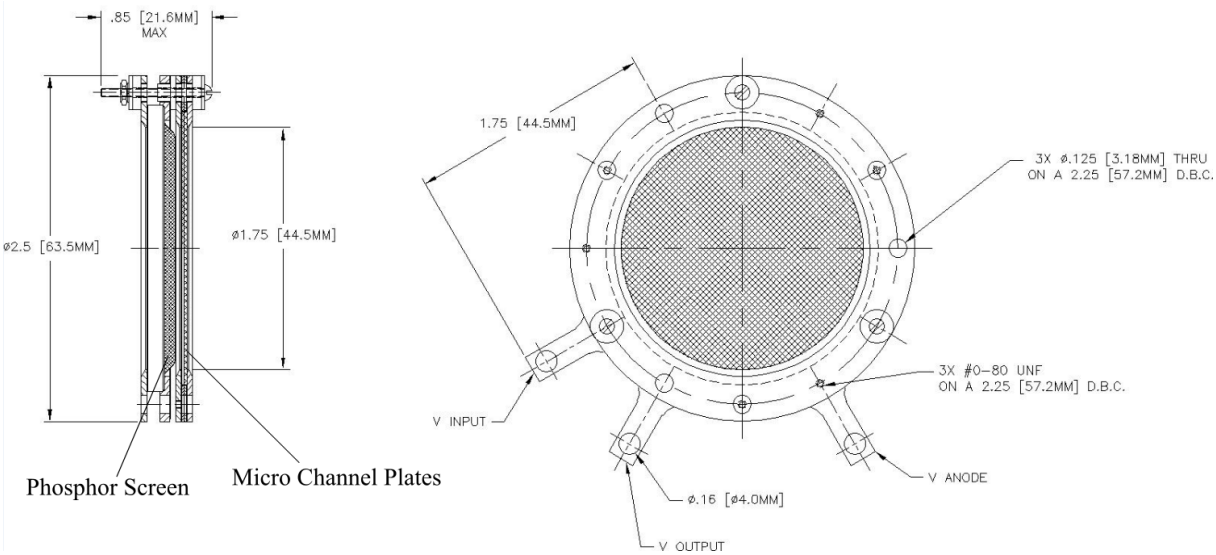

Figure 2.3: Drawing of the MCP detector

The detector is operated using 2100 V MCP-back voltage and 2500 V MCP-phosphor voltage. There is a mesh in front of the MCP to define a ground level. The MCP-front voltage was varied to see its influence on the electron detection efficiency (section 2.2.4). The ion detection efficiency is not significantly influenced by applying the MCP-front voltage (<100 V) because their mass is too high to be accelerated significantly by the applied voltage. The voltage pulses are decoupled from the MCP using the the in-house-made device depicted in figure 2.4.

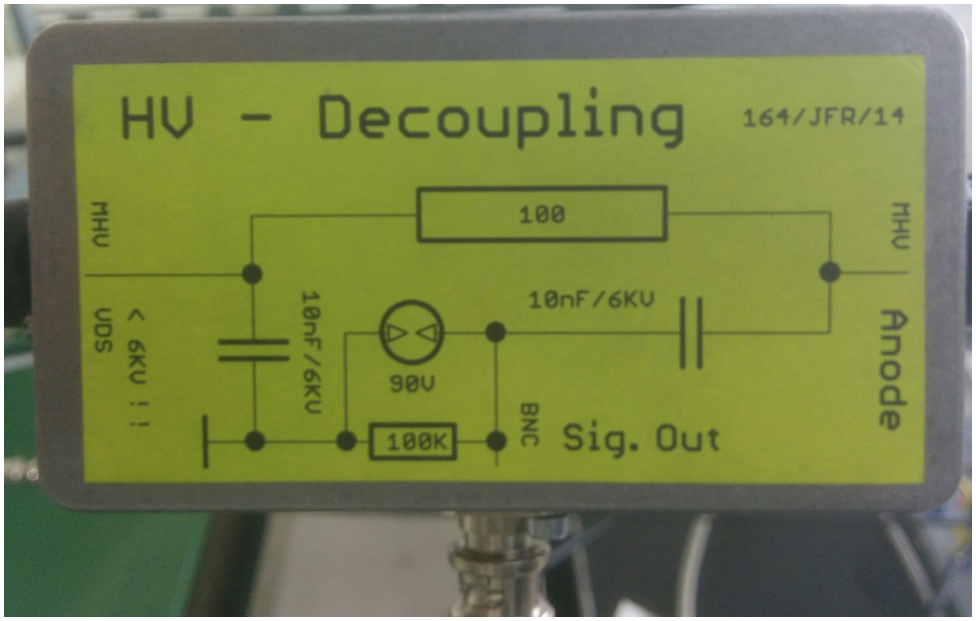

Figure 2.4: Picture of the decoupling box. A schematic wiring diagram is depicted on the cover.

2.1.4 High Voltage Switch

Being able to make photo-electron-photo-ion-coincidence (PEPICO) (described in section 2.4) measurements it is necessary to detect ions and electrons which are formed by one ionization event. Switching the repeller voltage from a small negative voltage ($\approx$ -3 V) to a high positive voltage (2 kV) in a very short time enables us to detect both species [13]. This is realized by an in-house built device using a solid state high voltage switch (Behlke HTS 31-03-GSM) that switches between these two voltages within 50 ns. The device with removed cover is shown in figure 2.5. A wiring diagram and a description of the inputs and outputs is depicted in figure 2.6.

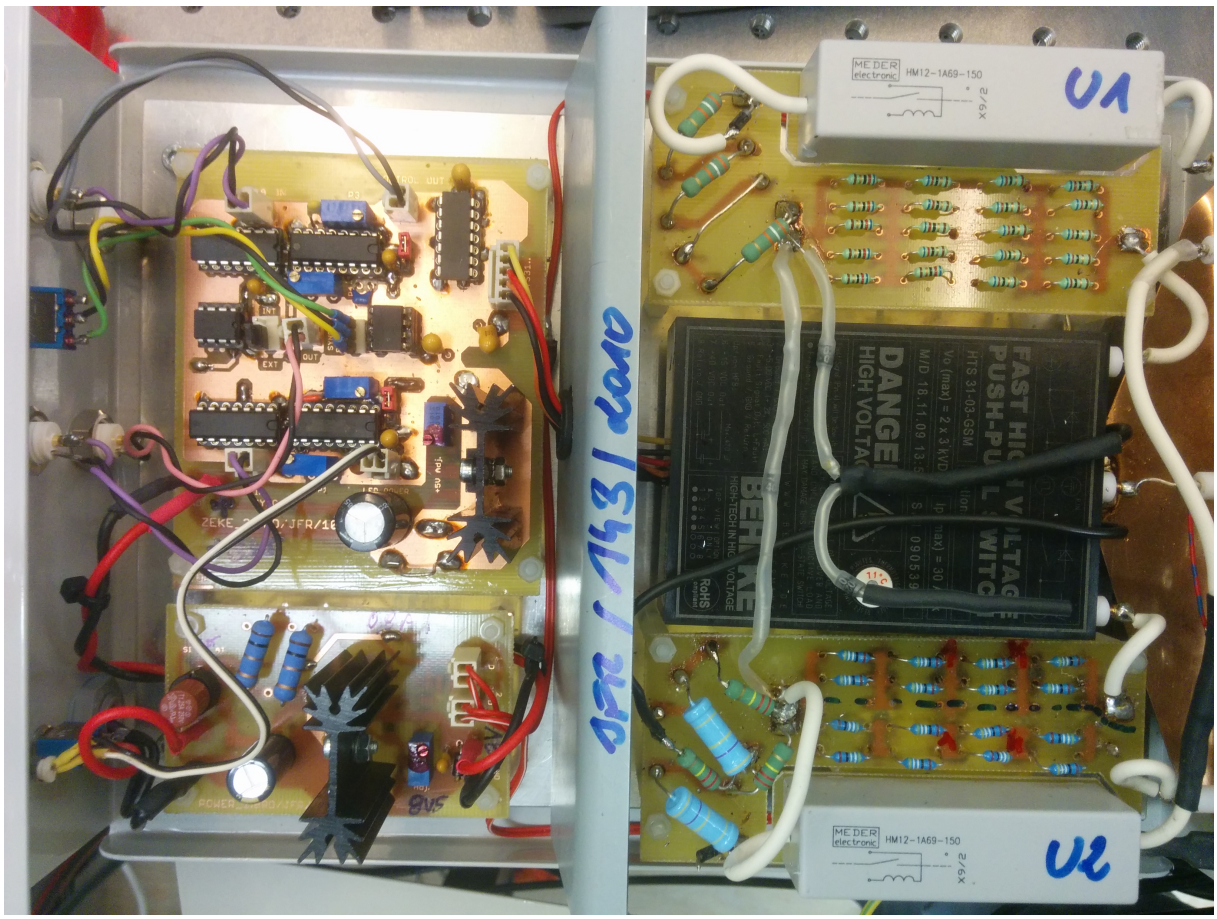

Figure 2.5: Picture of the HV switch device

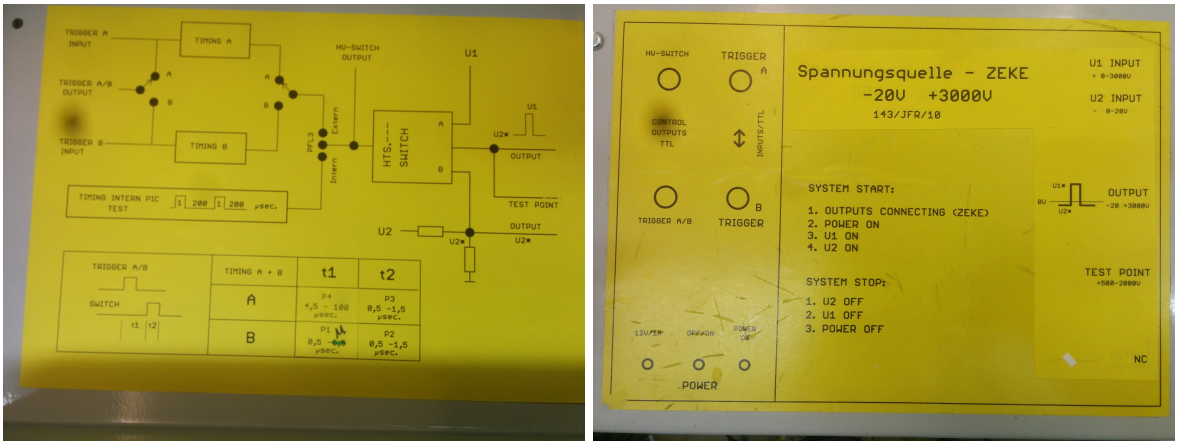

Figure 2.6: Wiring diagram of the device (left) and a description of the inputs and outputs (right)

The voltage range for the input of the positive voltage (U1) is (0-3000) V. The range for the negative voltage (U2) is (0-20) V. Applying voltages that are out of the specified ranges of U1 and U2 may damage the HV switch.

An artifact in the signal appears when the HV-switch is operating. This artifact is caused by switching the high voltage on and off. The switching causes a electrostatic induction in the flight tube, the solenoid and the mu-metal. If the repeller voltage is negative the charge carriers inside these conducting items are repelled. If the voltage is positive they are attracted to the repeller. A current is induced which causes a signal in the MCP detector. The artifact is affected mostly by the cable from the power supply to the solenoid [12]. The plug of this cable grounds the flight tube. Bending this cable has an influence on the shape of the signal. The same is true for the cables from the HV switch to the repeller and the cables to the HV switch but with a weaker effect. When the HV switch is turned off the signal vanishes. When the solenoid is not connected to the power supply and grounded the signal also vanishes. The MCP voltages (front, back, phosphor) don't influence the artifact. The amplitude seems to vary rather randomly. The discriminator level of the counter has to be adjusted to avoid it to misinterpret the artifact as electron counts.

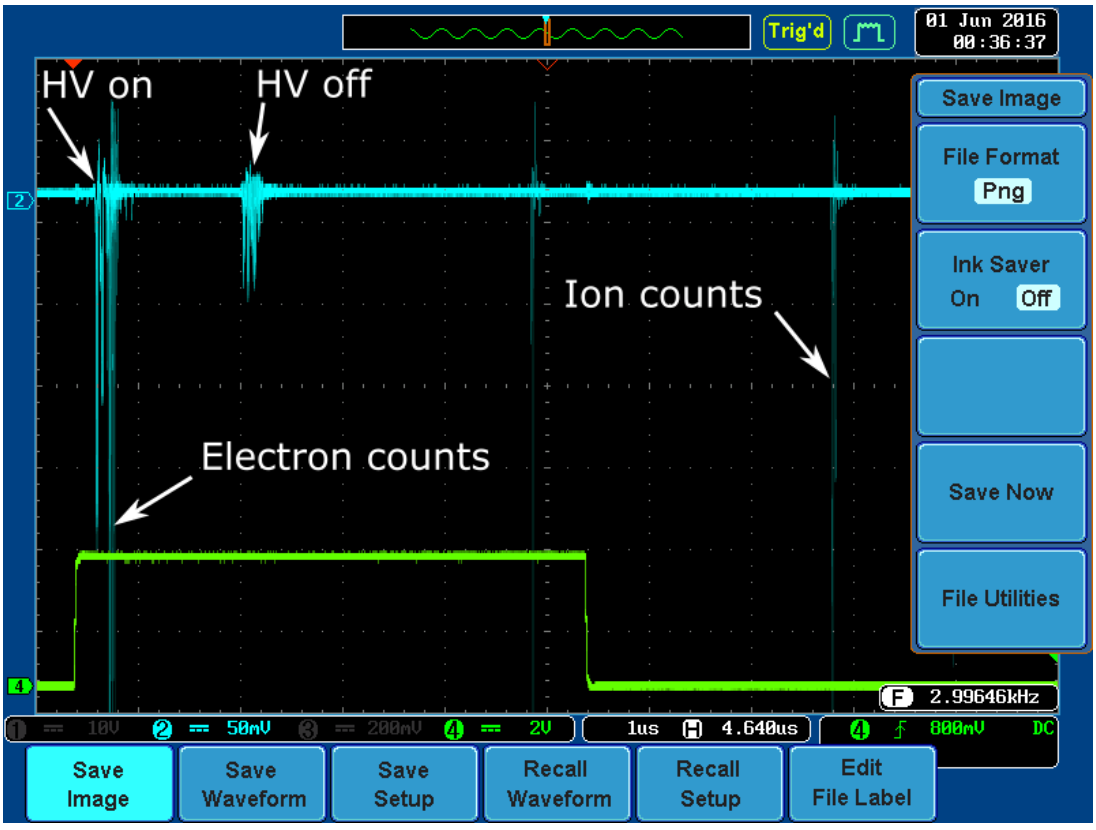

Figure 2.7: PEPICO signal (cyan) of acetone lionized with 400 nm pulses on the scope including the artifact at the times the HV is switched on and off, electron counts and ion counts. The green line is the trigger signal of delay 4.

A PEPICO signal of acetone lionized with 400 nm pulses on the scope including the artifact

at the times the HV is switched on and off, electron counts and ion counts is depicted in figure 2.7. Typical amplitudes of the artifact are 50 mV to 150 mV. As long as it is in this range it does not cause a problem in the data analysis as this is still much lower than typical peaks that are caused by electron hits ($\approx 300\,\mathrm{mV}$). The discriminator level can be set high enough not to misinterpret the artifact as electrons without impairing the electron gain too much.

2.1.5 Magnetic Bottle Spectrometer

After the ionization of an atom or a molecule the directions of the electrons' momenta are distributed over a large solid angle range. If the electrons' directions would not be influence by a force only a small fraction of the electrons would find the way to the detector. The detection efficiency would be very low. To be able to collect not only the electrons with momenta pointing towards the detector, a magnetic bottle setup [14] is used when operating the setup in the electron mode (section 2.2) or the PEPICO mode (section 2.4). With the help of this scheme and a small negative voltage at the repeller the solid angle of collection can be increased to almost $4\pi\,\mathrm{sr}$. The magnetic bottle scheme makes use of a high magnetic field at the spot of ionization and a lower magnetic field inside the flight tube to turn the momenta of the electrons towards the detector. The electrons' trajectories are parallelized. This is schematically illustrated in figure 2.8.

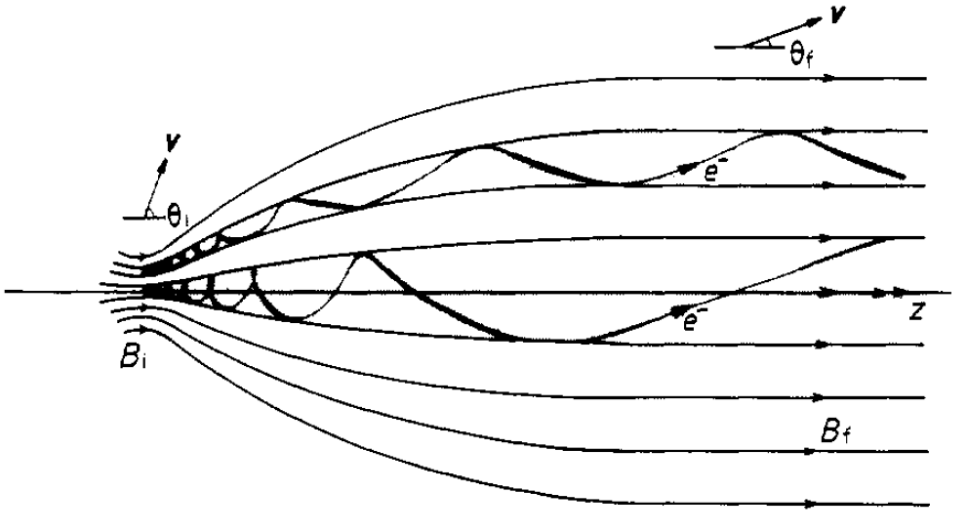

Figure 2.8: Illustration of the motion of electrons in the magnetic bottle with the strong magnetic field B_i on the left and the weak field B_f on the right site. Figure taken from [14]

The strong field at the interaction region is realized by a stack of neodymium magnets topped with a soft iron truncated cone at the repeller. The low magnetic field can be manipulated by different currents through the solenoid around the flight tube. In order to obtain good energy resolution three conditions must be satisfied:

Figure 2.9: Picture of the repeller with the soft iron truncated cone and the tip of the oven, which is used to evaporate solid specimen.

- the magnetic field at the source must be much stronger than the field in the flight tube, to give a high degree of parallelization of the trajectories
- the reduction in field must take place in a distance short compared to the length of the flight tube to ensure a small spread in the flight times
- the reduction in field must take place in a smooth way to avoid the harmful effects of strongly nonadiabatic behaviour

A characterization of the magnetic field for the magnetic bottle setup has been done by Franz Koberg as part of his bachelor's thesis [12]. The following values were found:

$$B_\mathrm{i} \;=\; 400\,\mathrm{mT} \text{ next to the repeller}$$
$$B_\mathrm{f} \;=\; 2.2\,\mathrm{mT} \;@\; 3\,\mathrm{A} \text{ solenoid current}$$

B_i... strong magnetic field at the interaction area
B_f... weak uniform magnetic field in the flight tube

The magnetic bottle system has similarities to an optical microscope, where a picture is magnified. The magnification M for a magnetic bottle setup is given by [14]:

$$M \;=\; \left(\frac{B_\mathrm{i}}{B_\mathrm{f}}\right)^{\frac{1}{2}} \tag{2.1}$$

This is important for electron signal considerations. The influence of the solenoid current on the electron spectra is discussed in section 2.2.5.

2.2 Electron Mode

In the electron mode the spectrometer is operated with a low negative repeller voltage ($\approx 3\,\mathrm{V}$). A current of $\approx 3\,\mathrm{A}$ is applied to the solenoid of the magnetic bottle setup. Time traces of 1000 ns are recorded. Ions are not detected.

2.2.1 Spectra Calibration

The signal coming from the MCP is digitized using a high speed digitizer (Gage Cobra, Dynamic Signals LLC). Then a peak finder program (described in section 2.5) detects peaks in the time traces. As we are interested in spectra (kinetic energy spectra for electrons) rather than the number of hits as a function of time, the corresponding energies have to be calculated. A calibration of the spectra must be done. The kinetic energy of an electron that hits the detector at a certain time t is:

$$E_{\mathrm{kin}} = \frac{m_{\mathrm{e}} \cdot L^2}{2(t + t_0)^2} \cdot \frac{1}{e} \tag{2.2}$$

E_{kin}...kinetic energy of the electron / eV
m_{e}... mass of the electron ($9.11 \cdot 10^{-31}\,\mathrm{kg}$)
L... length of the flight tube / m
t... time the electron hits the detector / s
t_0... time offset of trigger for the digitizer and the time of ionization / s
e... the elementary charge ($1.6 \cdot 10^{-19}\,\mathrm{C}$)

The length of the flight tube L and the time offset t_0 are not known. They have to be determined in order to calibrate the spectrum. The facts that ATI peaks appear equidistantly in energy and that the distance is the photon energy of the ionization wavelength, are used to determine L and t_0. An ATI measurement on argon was performed using the settings given in the caption of figure 2.10.

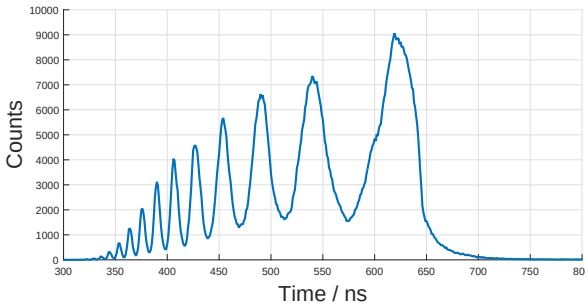

Figure 2.10: Time trace of the ATI spectrum of Ar. Laser wavelength: 800 nm; Laser power: 220 mW; Solenoid current: 3 A; Pressure: $4{\cdot}10^{-6}$ mbar Argon; Repeller voltage : -3 V ; (eiTOF_0955)

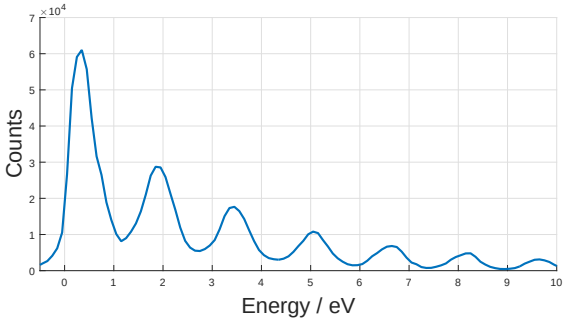

Figure 2.11: ATI photoelectron spectrum of argon. The times-of-flights signal shown in figure 2.10 were converted into kinetic energies using the calculated values for L and t_0. (eiTOF_0955)

The plot in figure 2.10 shows argon ATI peaks. As the counts are plotted as a function of time the peaks are not equidistant. Twelve ATI peaks are visible in this plot. The positions of these peaks were determined. The distance of one peak to the next one has to be 1.55 eV (photon energy for 800 nm). A function (DE.m;optimize_L_dt.m) was defined in Matlab which sums up the squared deviations of the 1.55 eV distance for all eleven neighboring pairs of peaks in energy space. Using *fminsearch* the parameters L and t_0 were determined. The calculation yields:

$$\underline{L = 0.5471\,\mathrm{m}}$$
$$\underline{t_0 = -133\,\mathrm{ns}}$$

The calculated length of the flight tube is in good agreement with measurements using a measuring tape. The length could not be determined exactly enough this way because the spot where the ionization takes place and the position of the detector are inside the vacuum chamber and therefore not accessible. The time trace depicted in figure 2.10 was converted into a kinetic energy spectrum using the calculated values for L and t_0. This spectrum is shown in figure 2.11.

Another way of determining t_0 yields a value that is in good agreement with the value calculated as discussed above. If the third harmonic (266 nm) of the fundamental (800 nm) is focused inside the vacuum chamber, photons are scattered at the repeller or at the walls of the chamber. Some of these photons eventually hit the MCP and are detected similar to electrons. A measurement has been performed to see at which time this prompt hits

the detector. To guarantee that only photons are detected the pressure was below 10^{-9} mbar, the solenoid current was set to 0 A and the repeller voltage was set to 0 V.

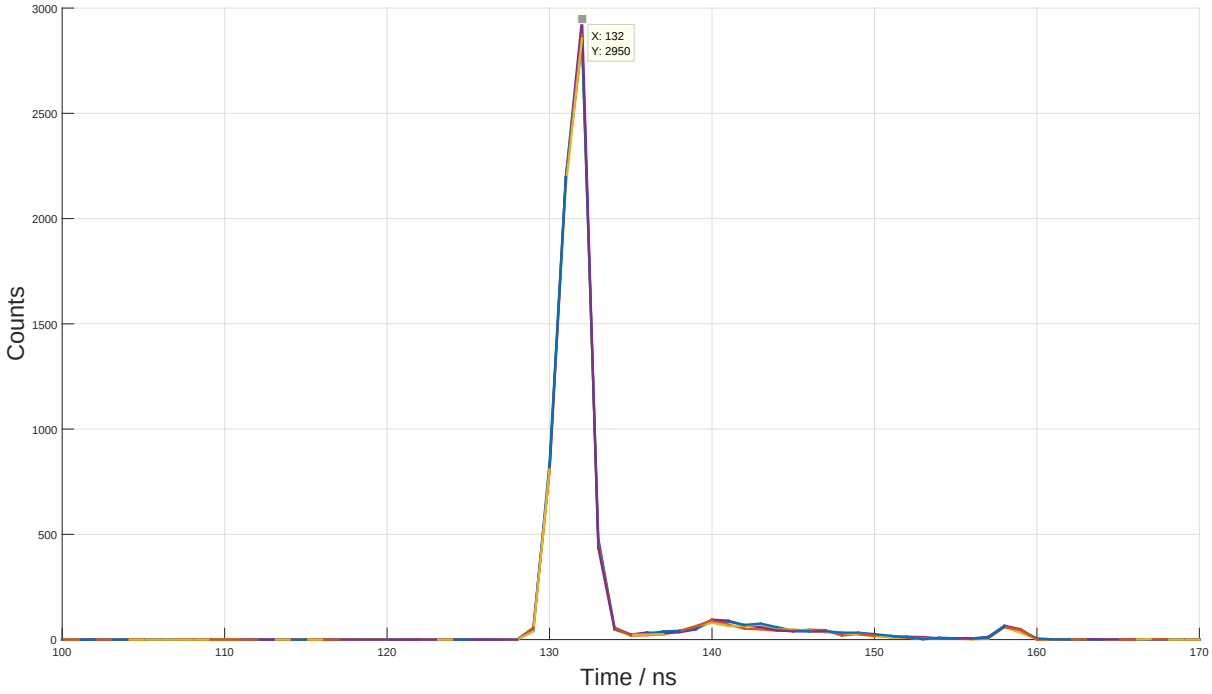

Figure 2.12: Number of counts caused by 266 nm photons with respect to time for four measurements. (eiTOF_1015-eiTOF_1018)

The plot in figure 2.12 shows that the prompt hits the detector 132 ns after the trigger pulse for the digitizer arrives. This is in very good agreement with the 133 ns calculated using the Argon ATI spectrum.

A small negative voltage (≈ -3 V) is applied to the repeller to improve the collection efficiency of the magnetic bottle scheme. The ionization takes place at a distance of $\approx$ 2 mm to the repeller. The electrons' electric potential is dependent on this distance and the repeller voltage. The voltage was varied to determine the potential of the electrons for certain repeller voltages.

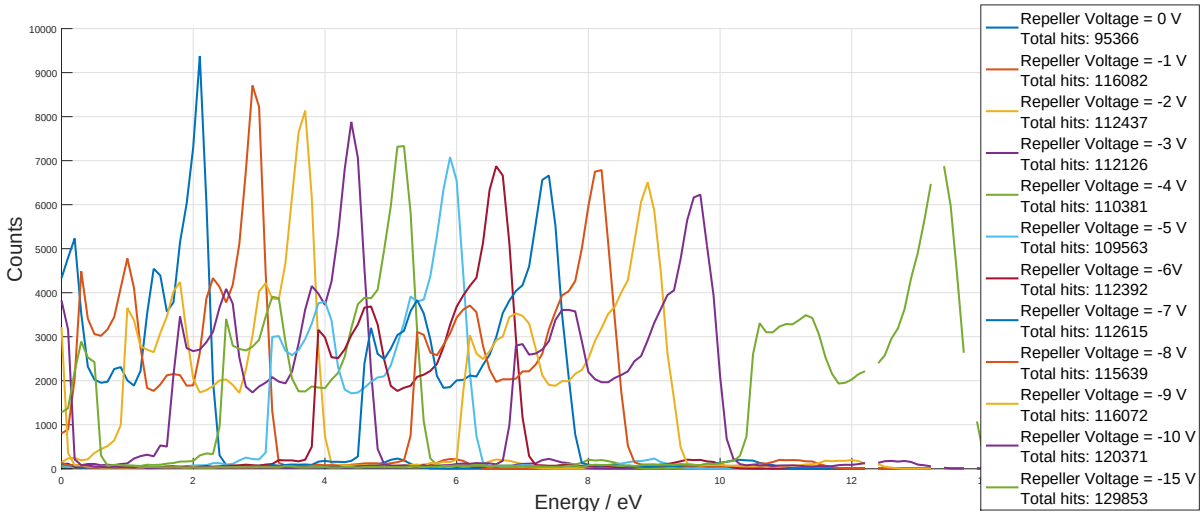

Figure 2.13: Acetone photoelectron spectra for different repeller voltages. Laser wavelength: 400 nm; Laser power: 45 mW; Solenoid current: 3 A; Pressure: $5 \cdot 10^{-6}$ mbar; (eiTOF_0767-eiTOF_0778)

Acetone photoelectron spectra for different repeller voltages are depicted in figure 2.13 . The total counts for each scan are given in the legend. The total hits show that the collection efficiency can be improved by applying a negative voltage in comparison to applying 0 V. The total hits do not significantly rise between -1 V and -10 V applied to the repeller. Applying -15 V gives an improvement of another $\approx$ 10% of electron gain. The height of the main peak decreases for higher voltages in spite of the increasing total counts. The reason is that the peak width rises due to the worse absolute resolution at short times (high energies). The spectrum taken with -15 V repeller voltage shows interruptions. At high energies there are sections where no time bin is correlated with certain energy bins. There cannot be any signal at these energies. To tackle this the time resolution has to be improved or a wider energy binning must be applied.

The expected linear shift of the spectra can be seen. The distance between the peaks of two spectra with a difference of 1 V repeller voltage amounts to 0.7-0.8 eV. The distance between the peak in the 0 V spectrum and the -10 V spectrum is 7.6 eV. This gives a electric potential of (0.76 ± 0.01) V per 1 V repeller voltage. This factor is called f for the sake of convenience. The uncertainty is given by the energy binning of the spectrum (0.1 eV). Taking into account that the distance of the interaction area and the repeller cannot be adjusted exactly the same every time gives a much higher uncertainty. We estimate that we adjust the distance of 2 mm with an accuracy of 0.2 mm (10%). Assuming

a linear dependence of f on the distance yields:

$$f \;=\; 0.76 \pm (10\% + 0.01) = 0.76 \pm 0.09 \tag{2.3}$$

Looking at the 0 V spectrum shows that the adjustment using f still does not yield a correct calibration as parts of this spectrum are not visible. There is still an offset of $\approx 1\,\mathrm{eV}$. This varies by about 0.2 eV from day to day. It has to be adjusted manually by measuring a known spectrum and shifting it the way distinctive structures match the known spectrum. This offset appears because the contact of the flight tube to the ground is bad. The flight tube is charged so the electrons are influenced by it. The charge of the tube varies and the distance of the spot of ionization to the repeller may vary due to a beam drift. So this adjustment has to be done before taking an electron energy spectrum to compensate the variation of the charge and the distance to the repeller.

2.2.2 Resolution

The intrinsic limit of the electron kinetic energy resolution of the magnetic bottle setup is given by the ratio of the magnetic fields [15]:

$$\left.\frac{\Delta E}{E}\right|_{MB} \;=\; \frac{B_f}{B_i} \tag{2.4}$$

This yields $\left.\frac{\Delta E}{E}\right|_{\mathrm{MB}} \;=\; 0.55\,\%$ for the operation with 3 A solenoid current according to the values of B_f and B_i determined by Franz Koberg [12].
The real electron energy resolution of the TOF (length = 0.55 m) is estimated to be $\frac{\Delta E}{E} \approx 4\%$. This value was obtained by the comparison with documented literature values ($\approx 4\%$, $\approx 3.3\%$ and $\approx 1.6\%$ for spectrometer with 0.46 m, 0.60 m and 2.6 m length [16–18]).
The spectral width of the ionizing laser pulse also has an influence on the resolution of the electron energy spectra. The center wavelengths and the spectral widths of the fundamental, the second harmonic and the third harmonic are given in table 2.1.

Table 2.1: Fundamental, SHG, THG specifications. The characterization was done by Paul Maierhofer [1].

Fundamental				
	/nm	/eV	/Hz	/cm^{-1}
central wave length	800	1.55	3.75E+14	12500
FWHM	80	0.16	3.75E+13	1253
SHG				
	/nm	/eV	/Hz	/cm^{-1}
central wave length	405	3.06	7.40E+14	24691
FWHM	14	0.11	2.56+13	854
THG				
	/nm	/eV	/Hz	/cm^{-1}
central wave length	269	4.61	1.12E+15	37175
FWHM	4	0.07	1.66E+13	553

For a certain spectral width of the ionization pulsethe spectral resolution is given by:

$$\Delta E = \sqrt{(0.04 \cdot E)^2 + \Delta E_\lambda^2} \tag{2.5}$$

This is an estimate for ΔE considering a one photon process. For a process of the order of n, ΔE_λ rises by a factor of $\sqrt{n}$:

$$\Delta E = \sqrt{(0.04 \cdot E)^2 + \left(\sqrt{n}\Delta E_\lambda\right)^2} \tag{2.6}$$

For the calculations above the spectral distributions are being considered to be Gaussian.

2.2.3 Influence of the Ionization wavelength

If the ionization potential (IP) of an atom or a molecule is very close to an integer multiple of the photon energy of the ionization wavelength, small deviation of this wavelength can cause major changes in the structure of the electron spectrum. The reason is that the number of photons needed for the ionization can vary by 1. For example if there is a peak in the electron energy spectrum at the energy just below the photon energy and the wavelength is decreased by a small amount, this peak vanishes and emerges at very low energies. The IP can be exceeded with the energy of one photon fewer. This effect has been observed ionizing argon ($IP = 15.76\,\text{eV}$) using 397 nm (3.13 eV) laser pulses.

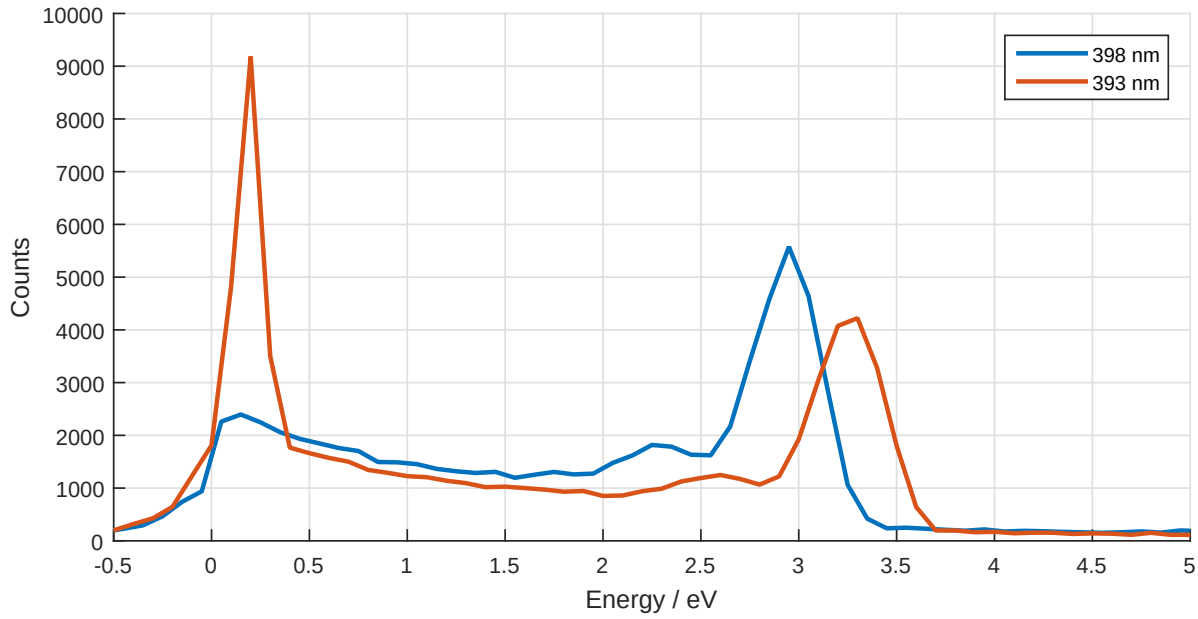

Figure 2.14: Argon electron energy spectrum using 398 nm laser pulses (blue line) and 393 nm pulses (orange line) (eiTOF_0951, eiTOF_0959)

When Argon is ionized with 398 nm (3.115 eV), six photons are needed and the resulting electron energy is 3.02 eV ($6 \cdot 3.115\,\text{eV} - 15.760\,\text{eV} = 2.930\,\text{eV}$) . This is what the blue line in the figure 2.14 shows. There is also some signal at lower energy that does not show any pronounced structure. This signal is assigned to background, which could be caused by perylene or water.

If the center wavelength is 393 nm (3.155 eV) the electron spectrum changes drastically. The deviation of the wavelength can be caused by a variation of the tilt angle of the SHG crystal. A different tilt angle changes the phase matching conditions and the origination of different wavelengths is favored. With 393 nm only five photons are needed and the electron energy is 0.015 eV ($5 \cdot 3.155\,\text{eV} - 15.760\,\text{eV} = 0.015\,\text{eV}$). The orange line in figure 2.14 shows the electron spectrum of argon for 393 nm ionization wavelength. This spectrum shows the peak at low energies as mentioned above. There is a big peak at 3.3 eV, which is assigned to a combination of two effects. The lower energy part of the structures appears because of the spectral distribution of the ionizing pulses. If photons from the low energy region of the spectrum are involved in the ionization still six photons

are needed to ionize argon and the electron energy is about the photon energy (3.155 eV). The higher energy part of the peak is explained by ATI. So six photons from the high energy region are absorbed although five would be sufficient for the ionization as the low energy peak shows.

2.2.4 Influence of the MCP-Front Voltage

Measurements on argon using 400 nm pulses were performed to monitor the effect of the MCP-front voltage on the photoelectron spectra. The measurements' settings are given in the caption of figure 2.15.

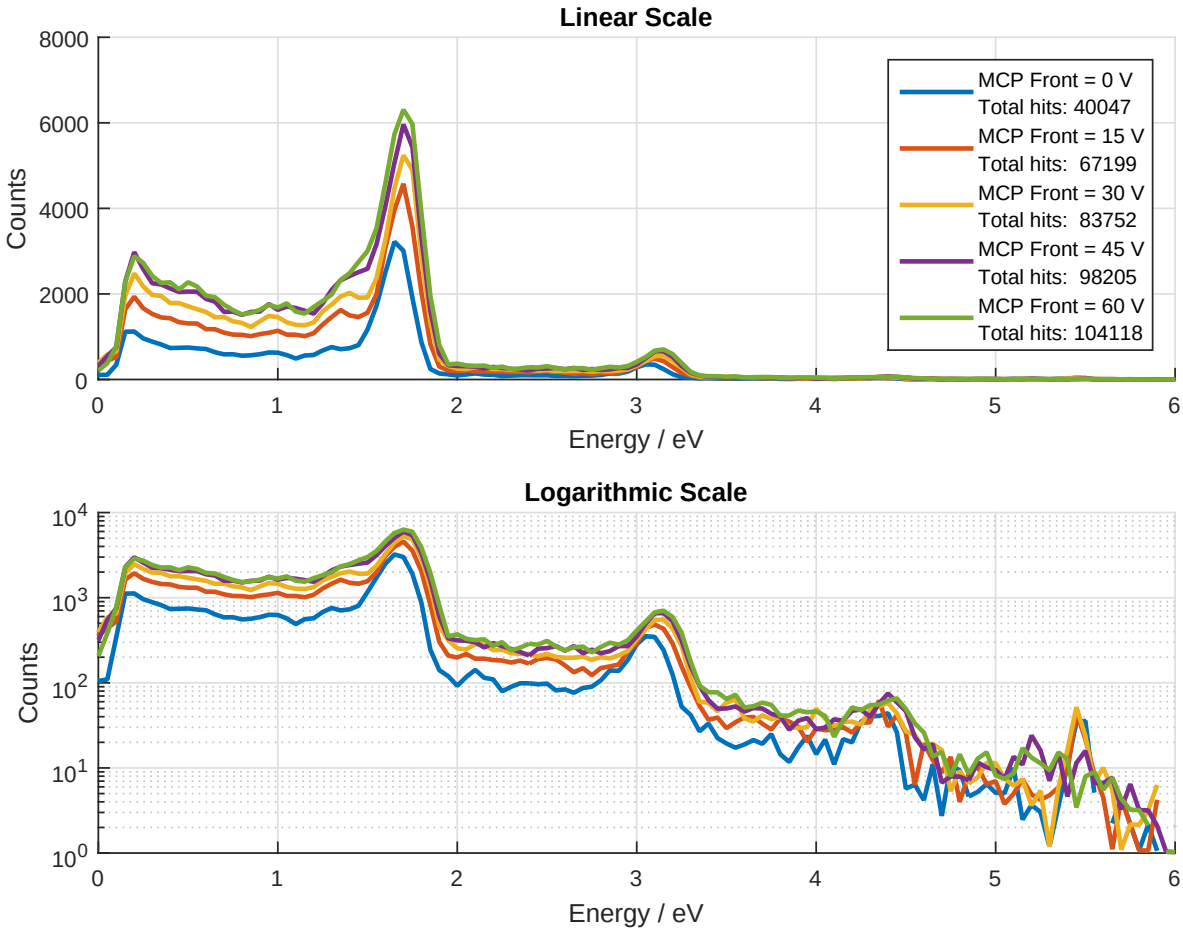

Figure 2.15: Linear and logarithmic plot of electron spectra of argon for several MCP-front voltages. Laser wavelength: 400 nm; Laser power: 200 mW; Solenoid current: 3 A; Pressure: 3.2*10^{-6} mbar argon; Repeller voltage : -3 V; (eiTOF_0924-eiTOF_0928)

Figure 2.15 shows electron energy spectra of argon ionized with 400 nm. This is the

same spectrum as depicted in figure 2.16 in section 2.2.5. The assignment of the peaks was done there. In the legend the number of total hits per measurement is given. The number of hits rises with higher MCP-front voltages. By applying 45 V the electron gain is increased by about 150% compared to 0 V MCP-front voltage as the total hits show (from 40 047 to 98 205). In the logarithmic plot the differences between the spectra taken with the various applied MCP voltages stay about the same over the whole spectrum. So the relative increase of the detection efficiency is equal for the energies visible in this spectrum. The plot also shows that the whole spectrum is shifted to higher energies for higher MCP-front voltages. This effect appears because the electrons are accelerated by the voltage and they therefore need less time to reach the detector. This equals a shorter effective length of the flight tube. These measurements all have been analysed using the same length of the tube to calculate the energy of the electron. This is why the spectra shift to higher energies with higher MCP-front voltages. Increasing the MCP-front voltage from 45 V to 60 V does not increase the electron gain further. 45 V is the optimal MCP voltage. Applying this voltage it is necessary to use batteries and a very short wire. If a long wire to a power supply is used the amplitude of the artifact in the high voltage switch (described in section 2.1.4) mode is increased significantly. With the batteries it rises from 120 mV to 140 mV which does not affect any measurement.

2.2.5 Influence of the Solenoid Current

To investigate the dependence of the weak uniform magnetic field on the electron gain and the electron spectra, measurements were done using different solenoid currents. For these scans argon ($IP_{Ar} = 15.76\,\text{eV}$) was ionized using 398 nm (3.115 eV)pulses. The measured electron energy spectra are depicted in figure 2.16.

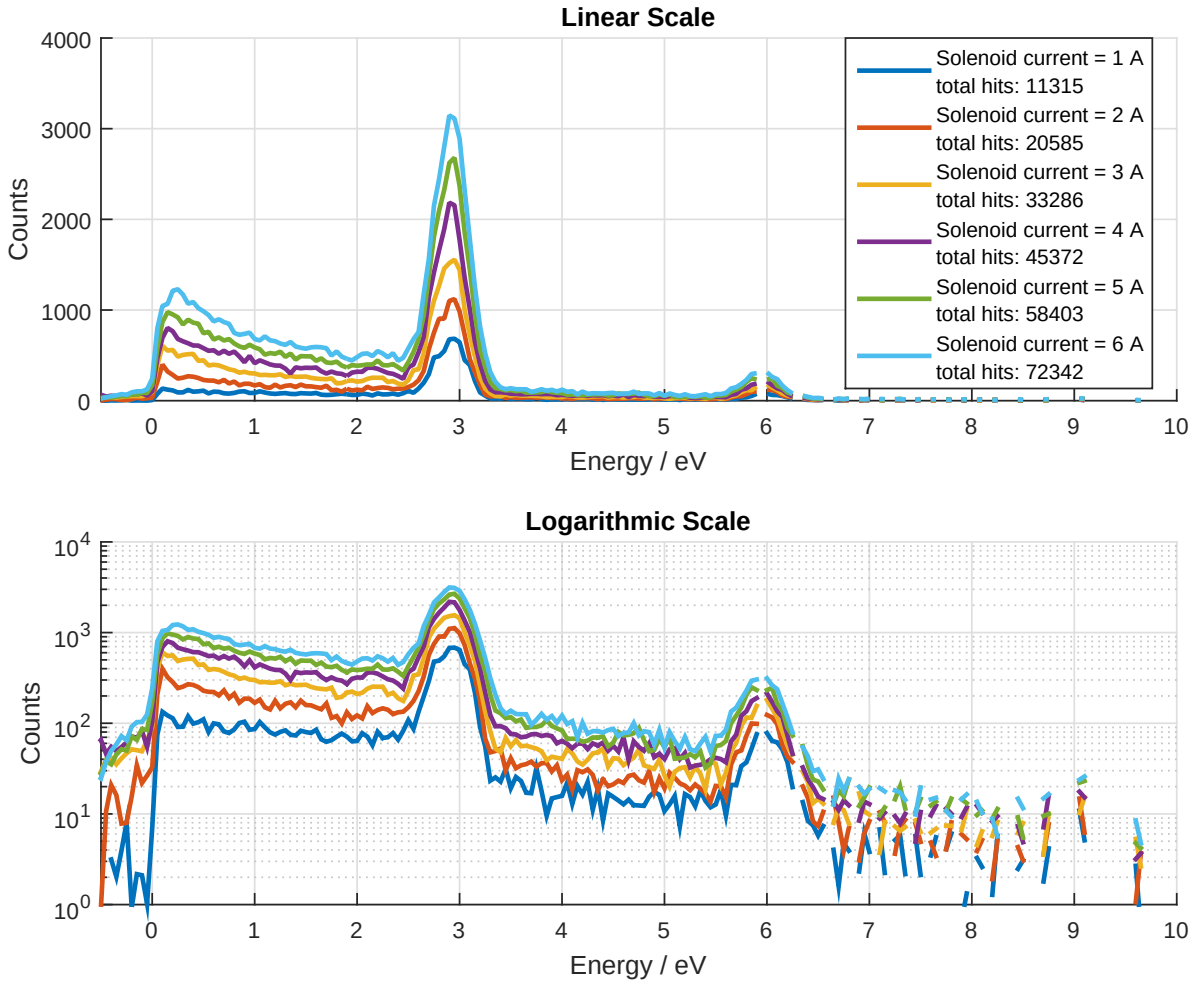

Figure 2.16: Photoelectron spectra of argon ionized with 398 nm using different solenoid currents. (eiTOF_0918-eiTOF_0923)

The spectra in figure 2.16 show one main peak at 2.9 eV. This peak arises from a six photon ionization of argon:

$$6 \cdot \ E_{phot} - IP_{Ar} \ = \ 6 \cdot 3.115\,\text{eV} - 15.760\,\text{eV} \ = \ 2.930\,\text{eV} \tag{2.7}$$

The peak at 6 eV is the first ATI peak. The total number of counts per scan is given in the legend. It increases with higher solenoid currents because the field B_f rises and the detected volume gets bigger as equation 2.1 illustrates. The number of total counts shows a linear dependence on the solenoid current and no saturation effect in the scanned current regime. There were no scans made with a solenoid current higher than 6 A. The reason is the quadratic dependence of the heating power on the current. A higher current would heat up the solenoid very fast. This could cause damage to it The temperature

of the solenoid must no exceed $180°C$. The detection efficiency of low energy electrons is increased disproportionately for rising currents. In the 6 A scan the signal at 0.2 eV is more than 10 times as high as in the 1 A scan while the gain of signal at 2.9 eV is smaller than a factor of 5. These slow electrons are not products of the ionization but arise from the background so this disproportionately increase of signal in the regime is not desirable. A solenoid current of 3 A has been chosen as standard setting. With this current the solenoid heats up exponentially in good approximation.

$$T(t) \;=\; T_\infty + A \cdot exp\left(\frac{-t}{\tau}\right) \tag{2.8}$$

The end temperature T_∞, the time constant τ and the parameter A were determined by Franz Koberg as part of his bachelor's thesis [12]:

$$\begin{aligned} T_\infty &= (45.0 \pm 0.1)^\circ\,\mathrm{C} \\ \tau &= (5500 \pm 14)\,\mathrm{s} \\ A &= (-24.5 \pm 0.1)^\circ\,\mathrm{C} \end{aligned}$$

This end temperature is not dangerous for the apparatus, so measurements that take a lot of time can be done without concerns. Also the detection efficiency with this current is acceptably high and the amount of detected slow background electrons is kept sufficiently low.

2.3 Ion Mode

A high positive repeller voltage ($\approx 2\,\mathrm{kV}$) is applied to push ions towards the detector. The magnetic bottle scheme is not operated. As the electrons are attracted by the repeller if a high positive voltage is applied to it, they cannot be detected in this mode.

2.3.1 Spectra Calibration

The mass to charge ratio of an ion with a certain time of flight is given by:

$$m/q = \frac{2 \cdot U \cdot (t + t_0)^2}{L^2} \cdot \frac{e}{1\,\mathrm{u}} \tag{2.9}$$

m/q...mass to charge ratio / u / e
U... electrical potential at the spot of ionization / V
t... time of flight / s
t_0... time offset of trigger for the digitizer and the time of ionization / s
L... length of the flight tube / m
e... the elementary charge ($1.6 \cdot 10^{-19}\,\mathrm{C}$)
1 u... 1 atomic mass unit ($1.66 \cdot 10^{-27}\,\mathrm{kg}$)

The length of the flight tube and t_0 have been determined in section 2.2.1. The only parameter to calibrate the mass spectrum is the electrical potential at the spot of ionization U. In the ion mode the voltage at the repeller is 2000 V. U is dependent on the distance of the spot of ionization to the repeller. The same consideration have been done in section 2.2.1 of the -3 V repeller voltage in electron mode. As the distance to the repeller may vary due to a beam drift U has to be adjusted to calibrate the mass spectrum. This is done by taking a mass spectrum of a known atom or molecule and shifting characteristic structures to match the known spectrum by varying U. This has been done for xenon using 400 nm pulses for ionization.

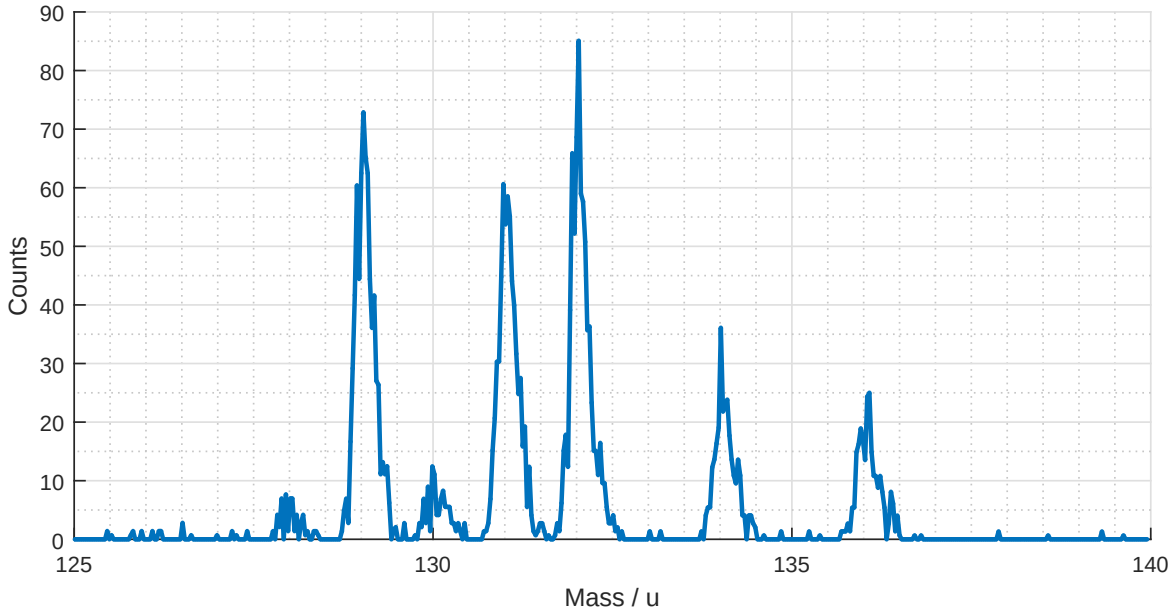

Figure 2.17: Xenon mass spectrum (eiTOF_0985)

Figure 2.17 shows the mass spectrum of xenon ionized with 400 nm pulses. Xenon is ideal for the calibration of the mass spectra. The stable isotopes and their proportions are well known and as it is an atom there is no fragmentation which makes the assignment of the peaks easier.

Table 2.2: Natural abundances of xenon isotopes

Isotopes	Natural Abundance / %
^{124}Xe	0.095
^{125}Xe	syn
^{126}Xe	0.089
^{127}Xe	syn
^{128}Xe	1.91
^{129}Xe	26.4
^{130}Xe	4.07
^{131}Xe	21.2
^{132}Xe	26.9
^{133}Xe	syn
^{134}Xe	10.4
^{135}Xe	syn
^{136}Xe	8.86

Matching the known spectrum yields $U = 1613\,\mathrm{V}$. This is in reasonable agreement with the similar calculations in 2.2.1 and the factor f given in equation 2.3.

$$f \cdot 2000\,\mathrm{V} \;=\; (0.76 \pm 0.09) \cdot 2000\,\mathrm{V} \;=\; (1520 \pm 180)\,\mathrm{V} \tag{2.10}$$

Note that U is dependent on the distance from the interaction area to the repeller. The value $U = 1613\,\mathrm{V}$ only applies for this measurements. It has to be found for every individual measurement to calibrate the mass spectrum.

2.4 PEPICO

Photoelectron spectra and mass spectra often do not reveal the whole picture of an ionization process. To obtain additional information electrons and ions are detected in coincidence. Photoelectron spectra can be associated with certain peaks in a mass spectrum this way. This technique is called photoelectron-photoion-coincidence (PEPICO). The detection of the two products (ion and electron) of one ionization event is realized by a fast switch of the repeller voltage using the device described in section 2.1.4. The switching of the repeller voltage and the temporally separated detection of electrons and ions is schematically illustrated in figure 2.18.

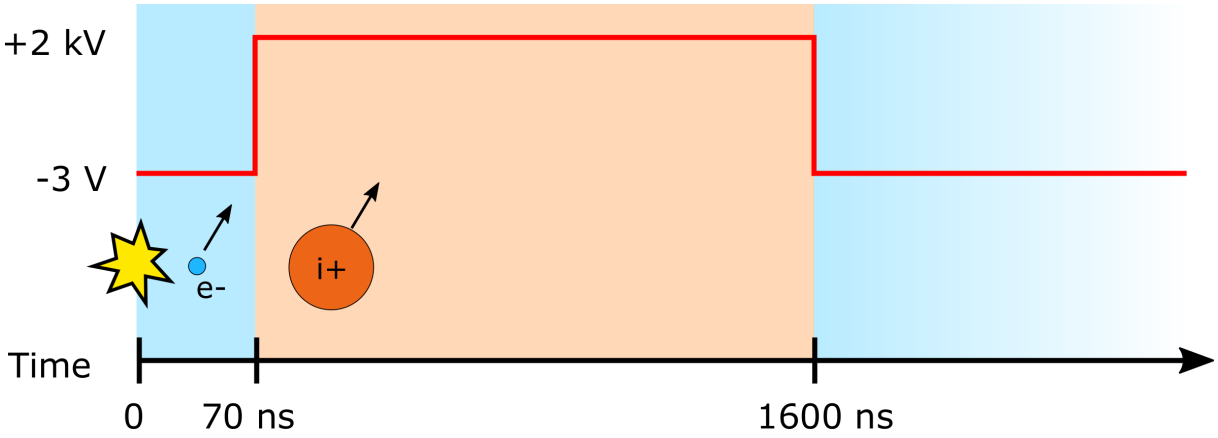

Figure 2.18: Illustration of the time dependent repeller voltage and the temporally separated regimes of electron on ion detection in the PEPICO mode.

At the time the laser pulse is at the focus point and the ionization takes place the repeller voltage is -3 V. The liberated electrons are very light and therefore very fast. Within the first $\approx$ 70 ns after the ionization the electrons pass the entrance of the drift tube and do not feel the voltage applied to the repeller anymore. Approximately 70 ns after the ionization the repeller voltage is switched to 2 kV. The mass of ions is very high compared to the mass of the electrons $\left(\frac{m_{proton}}{m_{electron}} \approx 1836\right)$ so their velocity is much lower. If the timing of the high voltage switching is optimized the distance the ions cover within the time the small negative repeller voltage is applied is negligible. The optimization of this timing is described in section 2.4.1. The high voltage is switched on for $\approx$ 1500 ns. Within that time the ions are pushed into the flight tube. Then the repeller voltage is switched to -3 V again. At a repetition rate of 3 kHz this process is repeated every 0.33 ms.

A schematic wiring diagram of the apparatus in PEPICO mode is depicted in figure 2.19. Delay 4 triggers the measurement. Delay 5 triggers the high voltage switch. The influence of this delay is discussed in 2.4.1. In PEPICO mode the magnetic bottle scheme is active. The applied solenoid current is 3 A (section 2.2.5). The influence of the magnetic field on the ions is negligible. The reason is the already mention high proton mass compared to the electron mass. A more detailed sketch of the optical setup is shown in figure 2.1 and the master's thesis of Paul Maierhofer [1].

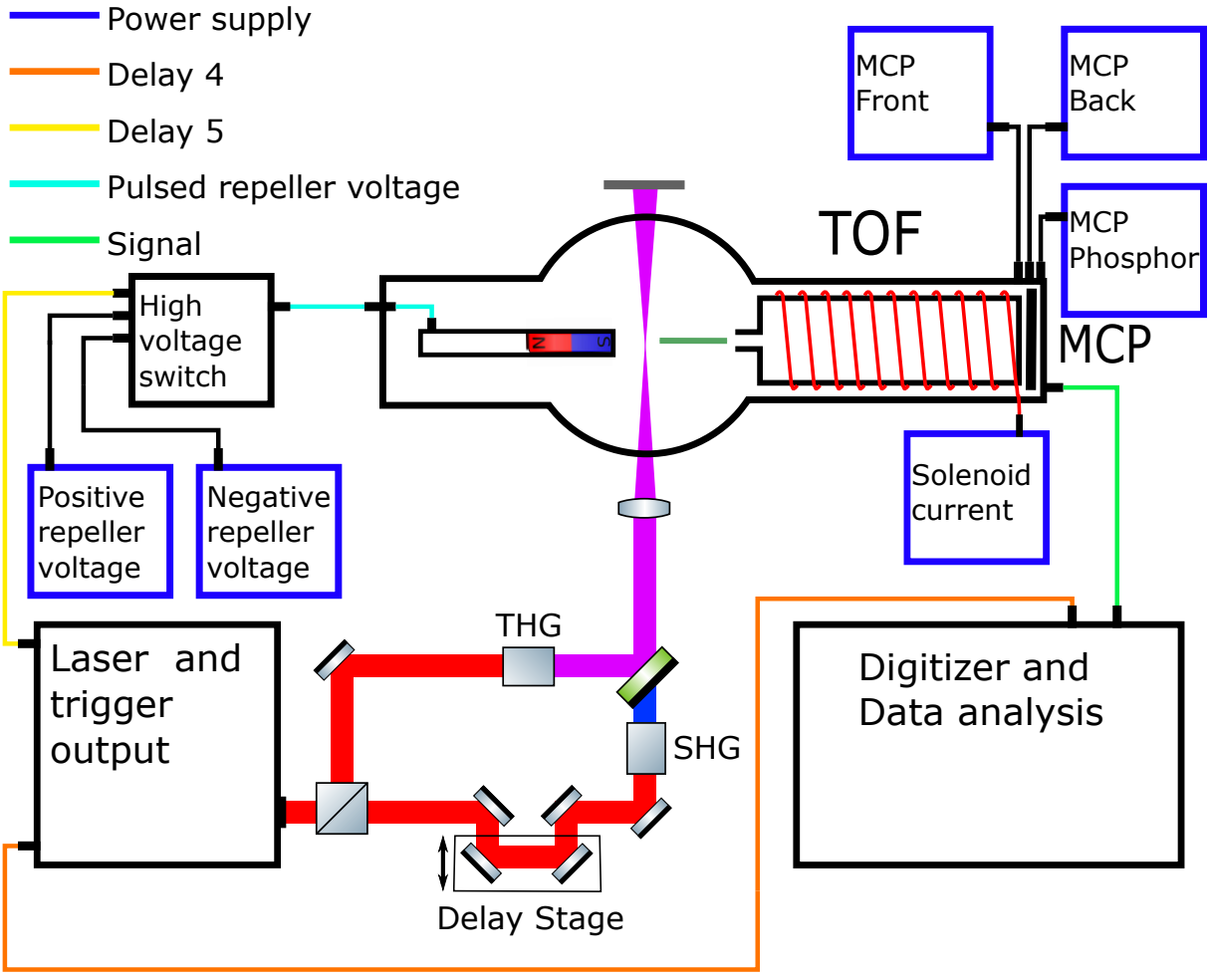

Figure 2.19: Schematic wiring diagram of the apparatus in PEPICO mode.

2.4.1 Influence of the Extraction Voltage Pulse

If the spectrometer is operated in PEPICO mode a high positive voltage is switched on at a certain time after the laser pulse ionizes the molecules or atoms. Delay 5 triggers the HV switch. There is an offset of -3600 ns to the time the start of the measurement is triggered. So if delay 5 is set to 3600 ns the HV is switched on at the time the measurement begins.

On the one hand the HV has to be switched on late enough that the electrons are in the flight tube at the moment the high voltage is switched on so they are not influenced by the electric field. On the other hand the delay has to be short so the ions do not spread to much before they are pushed towards the detector. This would impair the resolution of the mass spectra because the times the ions hit the detector are wider distributed. The peaks get broader if the delay to the HV pulse is increased. Initially delay 5 was set to 4300 ns. The peak width of the acetone parent peak (58 u) was measured using 800 nm and 4300 ns delay 5. The blue line in figure 2.20 shows the result of this measurement.

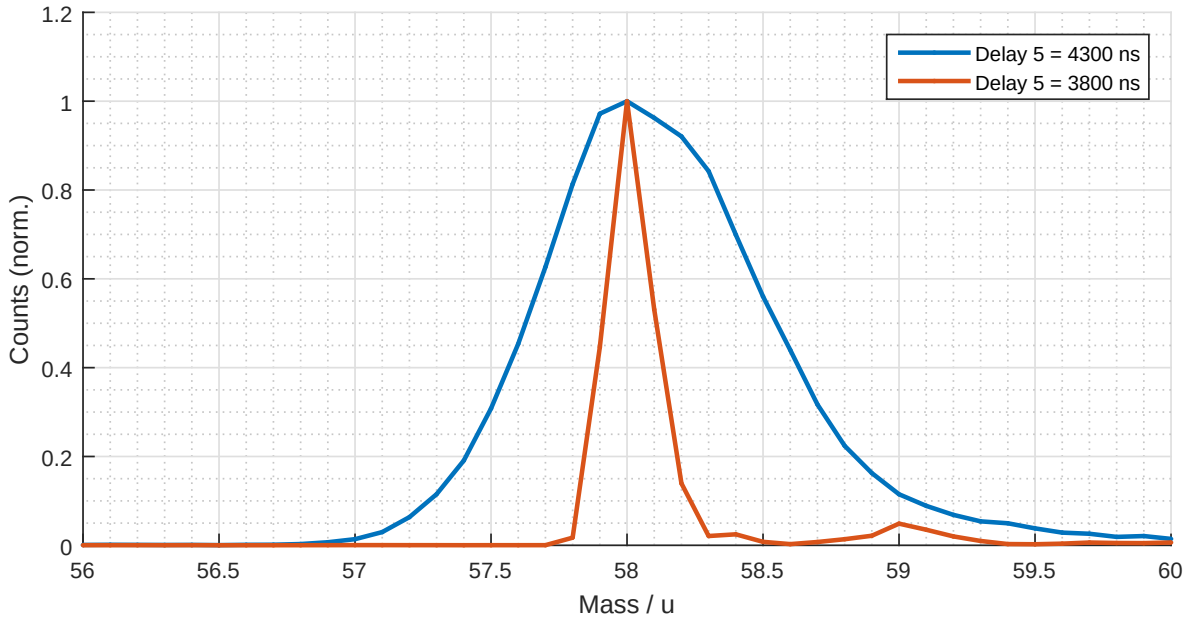

Figure 2.20: Acetone parent peak (58 u) for delay 5 = 4300 ns (blue line) and delay5 = 3800 ns (orange line). The full-width-half-maxima are FWHM = 1 u (blue) and FWHM = 0.25 u (orange) respectively. (eiTOF_0475,eiTOF_0484)

The full width half maximum of the blue peak in figure 2.20 is 1 u. The width of the same peak if a constant repeller voltage is applied amounts to 0.25 u. Hence the resolution of the mass spectrum is impaired significantly if this delay is applied. Spectra have been measured using different delays to see how short delay 5 can be set without distorting the electron energy spectrum.

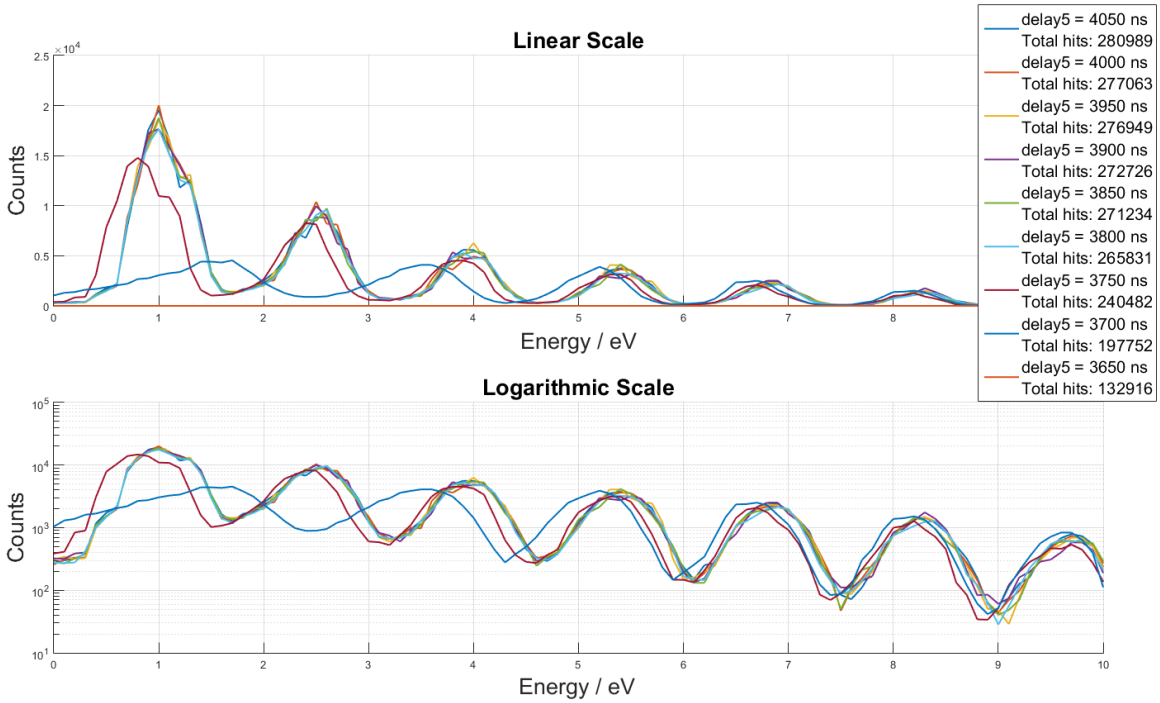

Figure 2.21: Photoelectron energy spectra of acetone ionized with 800 nm for different values of HV switch on times. (eiTOF_0477-eiTOF_0486)

Figure 2.21 shows the electron energy spectrum of acetone ionized with 800 nm for different values of delay5. The number of total hits and the value of delay 5 are given in the legend. The first seven ATI peaks are visible. It can be seen that the influence on the spectra is small if delay 5 is decreased from 4300 ns to 3800 ns. There is only a minor shift to lower energies. At a delay of 3750 ns especially the low energy electrons are significantly decelerated. Very slow electrons have not yet passed the entrance of the flight tube at the moment the high voltage is switched on. This effect can be seen more clearly looking at the spectrum with a delay of 3700 ns. This spectrum looks completely different to the ones taken with longer delays. While the very fast electrons are hardly influenced by the repeller voltage the slow ones are attracted to it and are therefore decelerated or do not even make into the flight tube. Using a delay of 3650 ns there is no electron signal at all. The attraction to the repeller is too strong. The measurements show that delay 5 can be set as low as 3800 ns without distorting the electron spectrum. The orange line in figure 2.20 shows the 58 u acetone parent peak using this delay.

The full width half maximum of the peak in figure 2.20 is 0.25 u which is the same as for a constant repeller voltage. By setting delay 5 to 3800 ns the resolution of the mass spectra in PEPICO mode could be significantly improved without impairing the quality

of the electron spectra. Now a peak can be seen at 59 u. This peak is assigned to acetone molecules with one ^{13}C, one ^{2}H or one ^{17}O isotope. The 59 u peak contains $\approx 6\,\%$ of the counts of the 58 u peak. The natural abundances of carbon, hydrogen and oxygen suggest that it contains $\approx 3\,\%$. The difference is caused by a saturation effect. The count rate was too high to detect all 58 u ions. The 59 u peak cannot be resolved using the initial delay as figure 2.20 shows.

2.4.2 Optimizing the Repeller Position

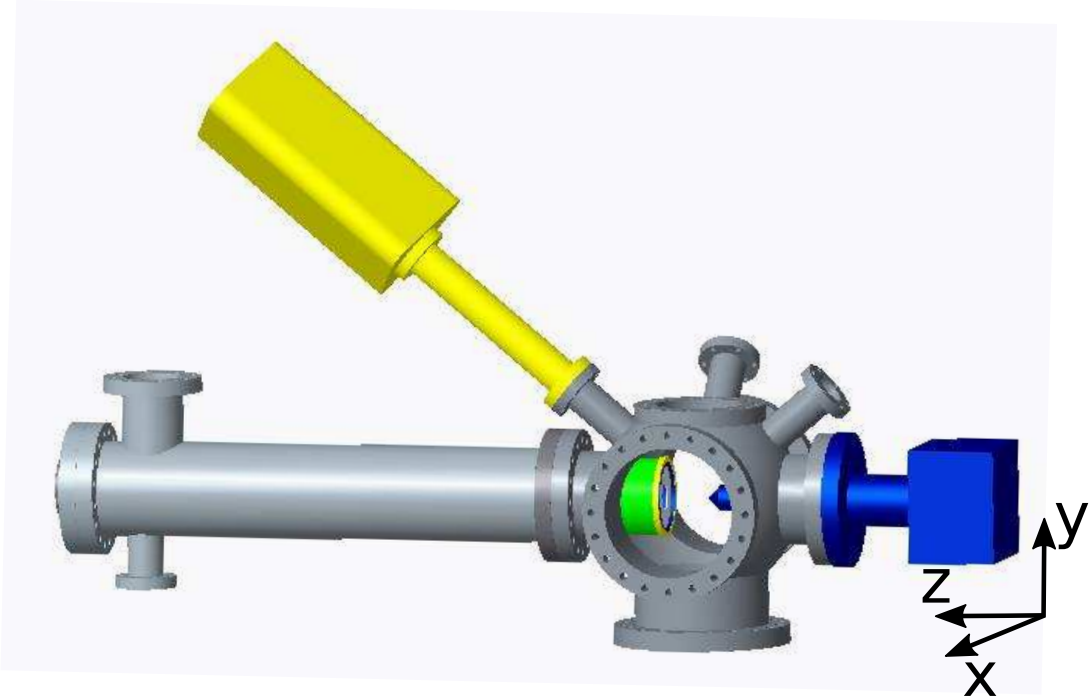

Figure 2.22: CAD drawing of the spectrometer and definition of the repeller coordinate system.

The electron and ion yields with respect to the y-position were measured for various distances of the repeller to the laser focus (z-coordinate). The coordinate system is defined in figure 2.22. The goal of these measurements was to find a repeller position where both the ion and electron yields are optimized. A high number of detected particles is needed because high detection efficiencies result in a high true to false ratio of the coincidences and shorter measuring times for the same signal to noise ratio. Neglecting saturation effects the position dependent electron and ion yields are modeled by the following formula:

$$Y_{e(i)}(\vec{r}) \;=\; \int_{\mathbb{R}^3} f_{e(i)}(\vec{\xi}) I(\vec{r}-\vec{\xi})^N d\xi^3 \tag{2.11}$$

$Y_{e(i)}(\vec{r})$...electron (ion) yield with respect to the repeller position
$f_{e(i)}(\vec{\xi})$... apparatus function for electron (ion) detection
$I(\vec{r}-\vec{\xi})$... intensity distribution of the laser beam
N... order of the ionization process

The apparatus functions for electron and ion detection are different due to different effects that are used to push the particles towards the detector. They are determined by magnetic and electric field distributions and the flight tube geometry. The intensity distribution can be described as a Gaussian beam (figure 2.23).

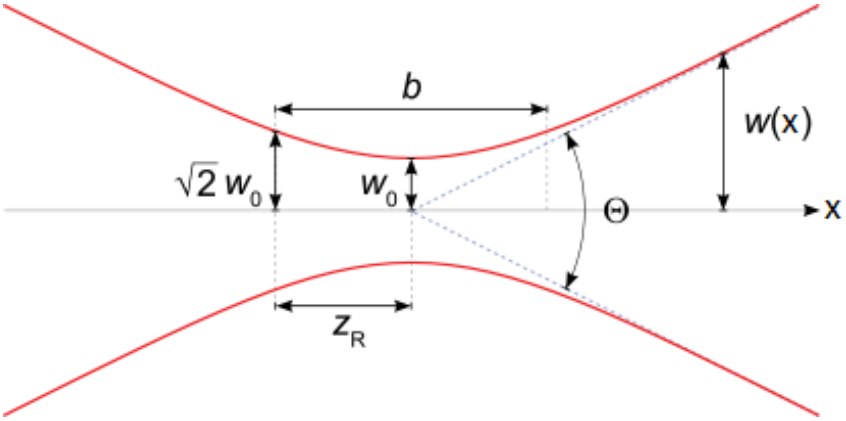

Figure 2.23: Gaussian beam width w(x) as a function of the distance x along the beam. w_0: beam waist; b: depth of focus; z_R: Rayleigh range; Θ: total angular spread. Figure taken from `https://upload.wikimedia.org/wikipedia/commons/thumb/5/53/GaussianBeamWaist.svg/350px-GaussianBeamWaist.svg.png` accessed on 30.04.2016

The laser focus was aligned the way it is very close to but does not the repeller if it is at $z = 5\,\text{mm}$. The distance of the focus to the repeller at $z = 5\,\text{mm}$ is smaller than 1 mm. The electron and ion yields where measured at various z and y-positions. The x-position was not varied. The results of these measurements are depicted in figure 2.24. The measurements were performed using the settings given in the caption of figure 2.24.

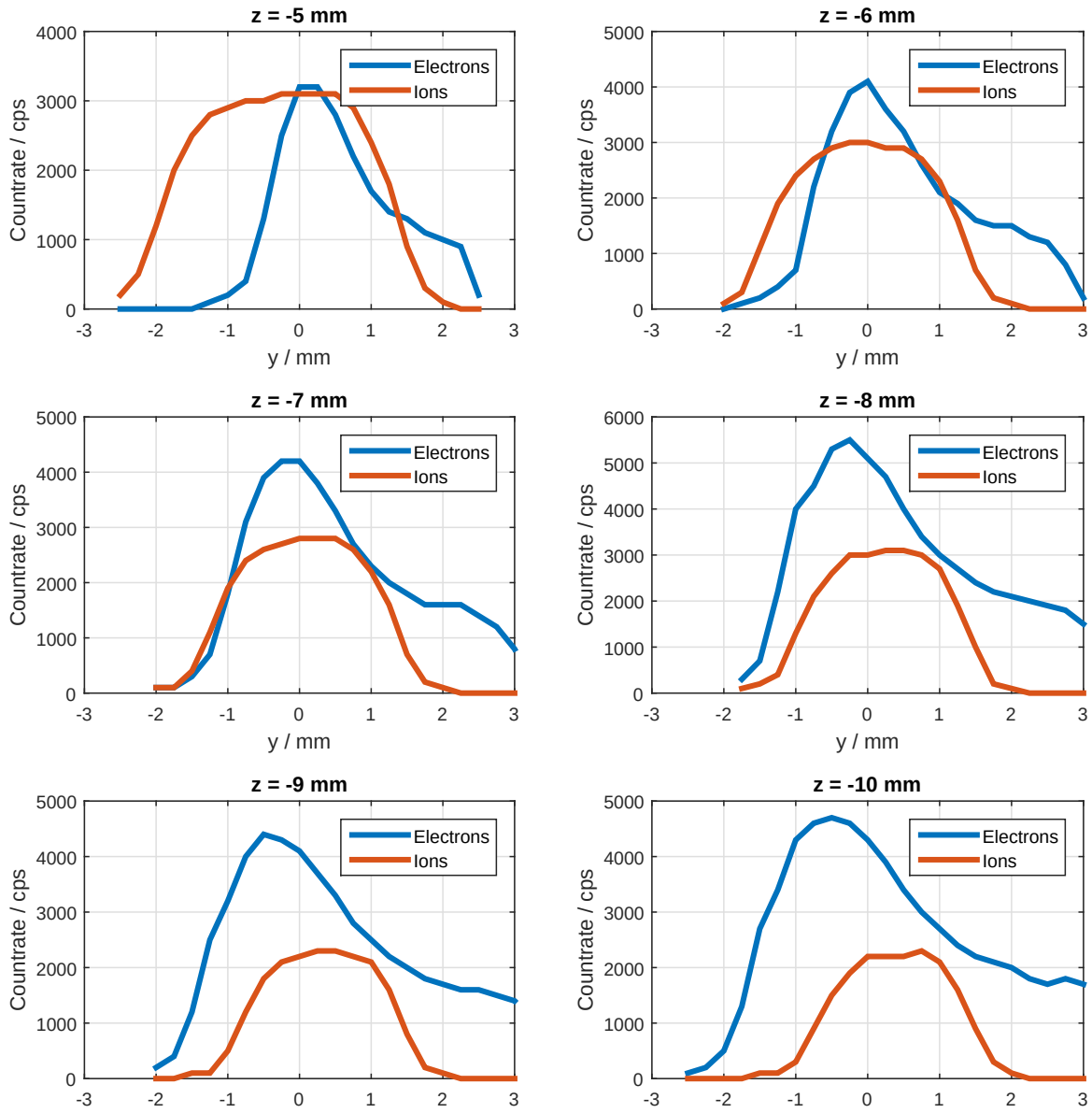

Figure 2.24: Electron and ion yield dependence of the y-position for different z-positions. z-positions in 1 mm steps from -5 mm (top left) to -10 mm (bottom right). Laser wavelength: 800 nm; Laser power: 130 mW; Solenoid current: 3 A; Pressure: $2*10^{-6}$ mbar argon; Repeller voltage electrons: -15 V; Repeller voltage ions: +2 kV; (14.07.2015)

The curves in figure 2.24 show the following influences of increasing distances of the repeller to the laser focus (lower z, because z is always negative in our coordinate system) on the electron and ion yields:

- the position of the maximum electron signal shifts to lower y
- the position of the maximum ion signal shifts to higher y

- the width of the electron peak increases
- the width of the ion peak decreases
- the total electron yield increases
- the total ion yield decreases

The reason for the increase of the electron yield for higher distances of the repeller to the interaction area is that the detection volume gets larger. As the distance to the magnet in the repeller gets higher the magnetic field (B_i) at the interaction area is decreased. So the magnification described in equation 2.1 gets smaller and the size of the detection volume increases. The decrease of the ion signal is explained by a more divergent electric field for high z-positions. Fewer ions are pushed in the direction of the detector. The shoulder of the electron curves at $y \approx 2\,\mathrm{mm}$ exists because the field geometry distorts the ionization volume picture on the detector. If there was no distortion the phosphor screen would show a straight line. The following figure shows the phosphor screen in electron detection mode.

Figure 2.25: Picture of the phosphor screen in electron mode

When the repeller goes up ($+y$) the picture on the screen goes down and vice versa. So it is obvious that the signal decrease is very steep when the repeller goes down because almost the whole pictured ionization volume exits the detection area at the same y-position. When the repeller goes up the decrease doesn't happen so suddenly because even at high y-position there is still that lobe in the center of line that reaches the detection area.

The repeller position $z = -7\,\text{mm}$ (second plot in the first column in figure 2.24 fits our requirements the best. The yields are satisfyingly high and the distance of the repeller to the laser focus ($> 2\,\text{mm}$) is big enough to minimize the risk of focusing on the repeller when the beam path varies. Focussing on the repeller would result in a very high number of ionization events and detected particles which could be harmful for the detector.

A scan of the electron and ion counts along the x-axis was done at $z = -7\,\text{mm}$. The y-position of the repeller was set to the position where the electron yield reaches its maximum. Figure 2.26 shows the count rate for electrons and ions with respect to the x-position.

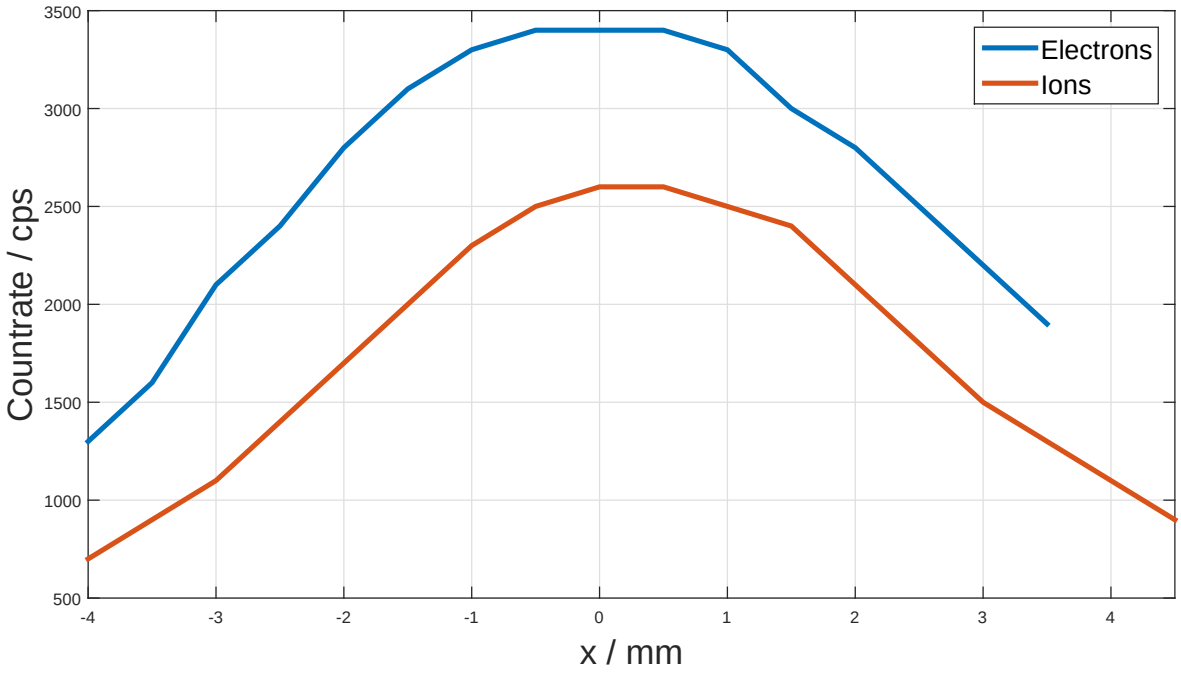

Figure 2.26: Electron and ion countrates with respect to the x-position of the repeller. $z = -7\,\text{mm}$; $y = 0\,\text{mm}$ (13.07.2015)

The electron and ion yields plotted in figure 2.26 show much broader peaks than the y-position scans in figure 2.24. The reason for this behavior is that the laser beam goes along the x-coordinate as figure 2.22 shows. The intensity decay in y-direction is Gaussian. The intensity decrease in x-direction is determined by the spot size with respect to x:

$$w(x) = w_0\sqrt{1+\left(\frac{x}{z_R}\right)^2} \tag{2.12}$$

As this function decreases slower than the Gaussian in y-direction the peaks in figure 2.26 are broader than the ones in the y-scans. The behavior of the ion and electron yields

are very similar. The x-position optimization can be done by optimizing one of the two signals.

2.4.3 Coincidence Detection

One method to associate energies of electrons with their counterpart ions is the coincidence method [19–21]. Here only laser shots where exactly one ion and one electron is detected are used for the data analysis. To obtain electron energy spectra corresponding to an ion mass one analyses the electron energies of the events where one hit at this ion mass occurs. This makes it possible to resolve the electron spectra corresponding to certain ion masses. Figure 2.27 shows an example of an ion mass resolved electron energy spectrum using the coincidence method. This experiment is described in detail in section 2.4.5.

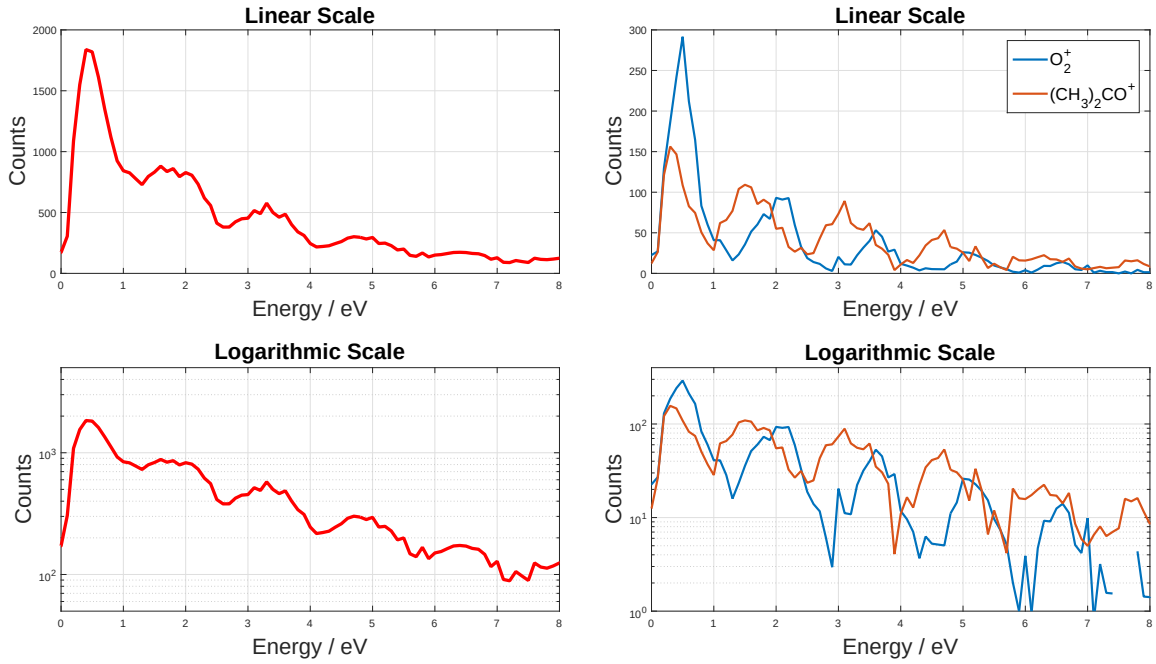

Figure 2.27: An example of a PEPICO plot using the coincidence method. The gas in the vacuum chamber contained air and acetone. **Left**: total electron signal. **Right**: ion mass resolved electron energy spectra. Green line acetone parent ion 58 u. Blue line O_2^+ ion 32 u. This experiment is described in detail in section 2.4.5. (eiTOF_0212-eiTOF_0221)

If the mean number of ionization events per shot $\bar{n}$ is very small the probability that the electron and the ion originate from the same atom or molecule is high. Such an event is called a true coincidence. If there are many ionization events per shot it may happen that one ion and one electron is detected but they do not originate from the same atom

or molecule. This would be a false coincidence. In order to optimize the count rate with respect to save measuring time with a high count rate but still detecting predominantly true coincidences, the following considerations in analogy to [19] have been made:

Both, electrons and ions, are detected with a probability that is smaller than unity. The particles may not find the way to the detector for example due to collisions with the rest gas, hit the mesh in front of the detector or hit the wall of the vacuum chamber at some point. If they find the way to the detector it still might be that they are not detected because the MCP's efficiency is less than unity. The mean number of electrons (ω_e) respectively ions (ω_i) detected per laser pulse is

$$\omega_e = \xi_e \bar{n} \tag{2.13}$$

$$\omega_i = \xi_i \bar{n} \tag{2.14}$$

with ξ_e and ξ_i being the detection probabilities for each species. The probability $p(n)$ that a certain number n of ionization events are caused by a laser shot can be described by a Poisson distribution:

$$p(n) = \frac{\bar{n}^n}{n!} e^{-\bar{n}} \tag{2.15}$$

The number k of electrons or ions detected for a certain number n of created electron-ion pairs is given by the binomial distribution:

$$p_{e(i)}(n,k) = \binom{n}{k} \xi_{e(i)}^k (1-\xi_{e(i)})^{n-k} \tag{2.16}$$

To calculate the probability ω_{11} to detect exactly one ion and one electron, one has to sum the product $p_e(n,1)p_i(n,1)p(n)$ over all n:

$$\omega_{11} = \sum_{n=1}^{\infty} \binom{n}{1} \xi_e (1-\xi_e)^{n-1} \binom{n}{1} \xi_i (1-\xi_i)^{n-1} \frac{\bar{n}^n}{n!} e^{-\bar{n}} \tag{2.17}$$

$$\omega_{11} = \sum_{n=1}^{\infty} n (1-\xi_e)^{n-1} (1-\xi_i)^{n-1} \frac{\bar{n}^{n-1}}{(n-1)!} e^{-\bar{n}} \xi_e \xi_i \bar{n} \tag{2.18}$$

Index transformation $n-1 \to m$

$$\omega_{11} = \sum_{m=0}^{\infty} \left[(m+1)(1-\xi_e)^m (1-\xi_i)^m \frac{\bar{n}^m}{m!} \right] e^{-\bar{n}} \xi_e \xi_i \bar{n} \tag{2.19}$$

$$\omega_{11} = \sum_{m=0}^{\infty} \left[(m+1) \frac{((1-\xi_e)(1-\xi_i)\bar{n})^m}{m!} \right] e^{-\bar{n}} \xi_e \xi_i \bar{n} \tag{2.20}$$

with the two Taylor series

$$\sum_{n=0}^{\infty} \frac{x^n}{n!} = e^x \quad \text{and} \quad \sum_{n=0}^{\infty} \frac{nx^n}{n!} = xe^x \tag{2.21}$$

the following term for ω_{11} is obtained:

$$\omega_{11} \;=\; \xi_e \xi_i \bar{n} \left[1 + \bar{n}(1-\xi_e)(1-\xi_i)\right] e^{-\bar{n}+\bar{n}(1-\xi_e)(1-\xi_i)} \tag{2.22}$$

If n electron-ion pairs are created, the probability to detect one electron and one ion that originate from the same atom or molecule is $\frac{1}{n}$. So to get the probability to detect a true coincidence one has to sum $\frac{p_e(n,1)p_i(n,1)p(n)}{n}$ over all n:

$$\omega_{11}^{(t)} \;=\; \xi_e \xi_i \bar{n} e^{-\bar{n}+\bar{n}(1-\xi_e)(1-\xi_i)} \tag{2.23}$$

The probability to measure a false coincidence is calculated by subtracting $\omega_{11}^{(t)}$ from ω_{11}:

$$\omega_{11}^{(f)} \;=\; \xi_e \xi_i \bar{n}^2 (1-\xi_e)(1-\xi_i) e^{-\bar{n}+\bar{n}(1-\xi_e)(1-\xi_i)} \tag{2.24}$$

The ratio of true coincidences to false coincidences (true-to-false ratio) is an important measure. A desired true-to-false ratio dictates the mean number of ionization events per laser shot.

$$R(\bar{n}) = \frac{\omega_{11}^{(t)}}{\omega_{11}^{(f)}} \;=\; \frac{1}{\bar{n}(1-\xi_e)(1-\xi_i)} \tag{2.25}$$

$\bar{n}$ is dependent on the investigated gas mixture, the pressure inside the vacuum chamber and the laser intensity. As the variation of the laser intensity may change the measured mass and electron energy spectra of a certain gas mixture, varying the gas pressure is the favorable way of manipulating $\bar{n}$ and in further consequence the true-to-false ratio $R(\bar{n})$.

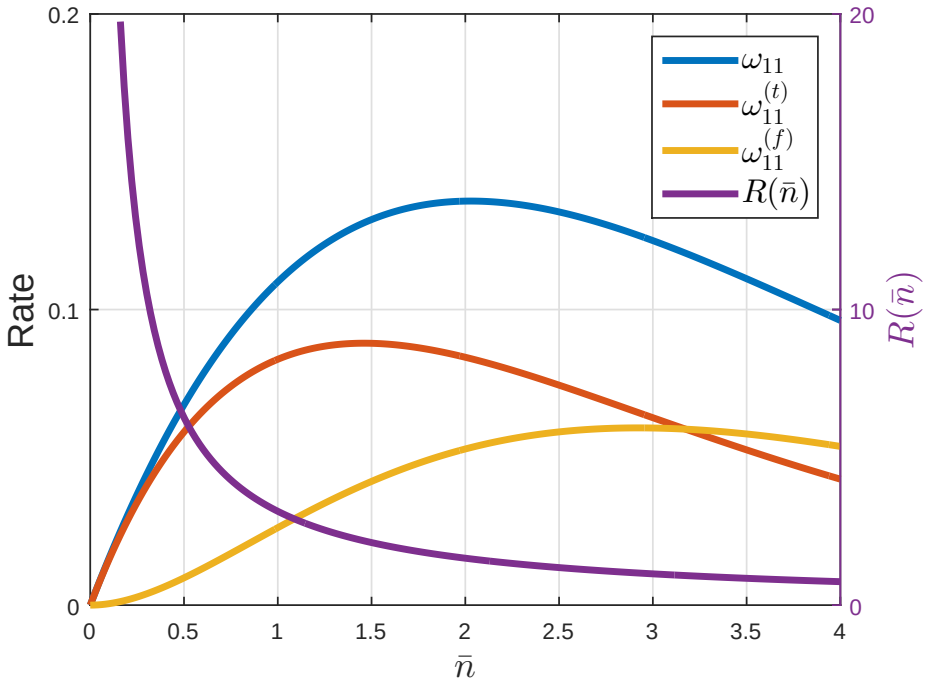

Figure 2.28: Left y-axis: True $\omega_{11}^{(t)}$, false $\omega_{11}^{(f)}$ and total ω_{11} coincidence rates as functions of the mean number of ionization events per laser pulse $\bar{n}$. **Right y-axis**: True-to-false $R(\bar{n})$ as a function of the mean number of ionization events per laser shot $\bar{n}$. The detection efficiencies have been set to typical values of the experiments: $\xi_e = 0.55$; $\xi_i = 0.3$ [19]

The plot in figure 2.28 shows that ω_{11} peaks at $\bar{n} = 2$ for the detection efficiencies given in the caption of the figure. At this point the true-to-false ratio is 1.6. At $\bar{n} = 3.2$ the value of $\omega_{11}^{(f)}$ exceeds the value of $\omega_{11}^{(t)}$ so the true-to-false ratio drops below 1. Calculating the values of ξ_e and ξ_i for a dataset is described below.

The mean numbers of electrons ω_e and ions ω_i detected per shot are given by the numbers of total hits for each species divided by the number of laser shots. These values can easily be calculated for a given dataset. The equations 2.14 and 2.13 can be rearranged so that the efficiencies ξ_e and ξ_i are given as a function of $\bar{n}$:

$$\xi_e = \frac{\omega_e}{\bar{n}} \tag{2.26}$$

$$\xi_i = \frac{\omega_i}{\bar{n}} \tag{2.27}$$

Now ω_e and ω_i are put into equation 2.22 so that ω_{11} is only a function of $\bar{n}$:

$$\omega_{11} = \frac{\omega_e \omega_i}{\bar{n}} \left[1 + \bar{n}\left(1 - \frac{\omega_e}{\bar{n}}\right)\left(1 - \frac{\omega_i}{\bar{n}}\right)\right] e^{-\bar{n}+\bar{n}\left(1-\frac{\omega_e}{\bar{n}}\right)\left(1-\frac{\omega_i}{\bar{n}}\right)} \tag{2.28}$$

ω_{11}, ω_e and ω_i are directly given by the dataset. It is the number of events where one electron and one ion is detected divided by the number of shots. Equation 2.28 is solved numerically using the Matlab routine $fsolve$. Now as $\bar{n}$ is determined, ξ_e and ξ_i are calculated by putting $\bar{n}$ into equations 2.27 and 2.26.

2.4.4 Covariance Detection

Evaluating the covariance of ions with a certain masses and electrons with certain energies is another way to associate electron energies with the corresponding ions [20–23]. This method has one big advantage compared to the coincidence method where only the events where one ion and one electron is detected are treated. As the whole acquired data is used for the evaluation of the covariance, one is not forced to go to very low count rates. This can save up to a factor of 100 in measuring time. The detector limits the count rate. If two ions with the same mass to charge ratio are produced in one laser shot and both hit the detector, they are detected only as one hit if their differences in time-of-flights is below the dead time of the detector. If this happens too often the covariance evaluation does not work accurately. The rate at one mass-to-charge peak should not exceed 0.5 hits per shot to avoid this phenomenon. If the ion signal is widely distributed very high count rates are possible without impairing the accuracy of the covariance. If there are only a few peaks in the mass spectrum the total count rate must be kept relatively low.

The Covariance is defined as:

$$Cov(x,y) \;=\; \langle (X - \langle X\rangle)(Y - \langle Y\rangle)\rangle \;=\; \langle X(x)Y(y)\rangle - \langle X(x)\rangle\langle Y(y)\rangle \tag{2.29}$$

For the evaluation of the acquired data X_i is a vector representing an electron-TOF time trace for the i-th laser shot. Its indices x are equivalent to times-of-flights. The increment is dependent on the settings of the digitizer(usually 1 ns or 0.5 ns). The values of $X_i(x)$ are either 1 if a hit is detected at time x or 0 if no hit is detected at time x. Exactly the same is true for Y_i representing the ion-TOF time trace for the i-th laser shot.
To calculate the covariance of electron-times-of-flights and ion-times-of-flights the expectation values in equation 2.29 are evaluated by summing over the N laser shots:

$$Cov(x,y) \;=\; \frac{1}{N}\sum_{i=1}^{N} X_i(x)Y_i(y) - \left(\frac{1}{N}\sum_{i=1}^{N} X_i(x)\right)\left(\frac{1}{N}\sum_{i=1}^{N} Y_i(y)\right) \tag{2.30}$$

These sums are calculated using matrix multiplications in Matlab. It is possible that covariances <1 occur. These values are set to zero because they make physically no sense. This would mean that the appearance of a certain ion avoids certain electron energies. The resulting covariance of x and y can be plotted as a 2-D covariance map:

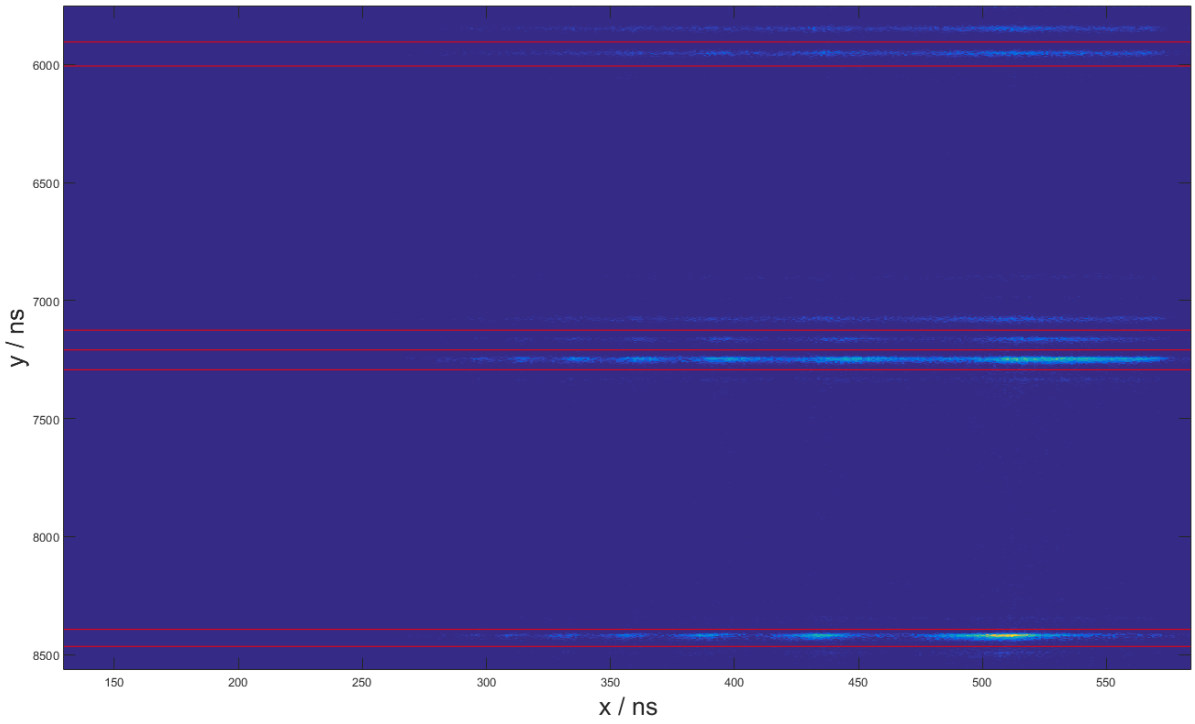

Figure 2.29: A covariance map of a measurement on n-butane ionized with 800 nm. x is the time-of-flight of electrons and y is the time-of-flight of ions. Dark areas represent low covariances, bright areas represent high covariances. The red lines show the boundaries of the mass intervals of interest.

An electron energy spectrum is obtained by summing up the covariances in a certain ion time-of-flight interval corresponding to a mass peak along the y axis. This summing up equals a wider binning and does not cause any errors. This can be done for multiple mass peaks. The red lines in the figure 2.29 show the boundaries of the mass intervals of interest of this measurement.

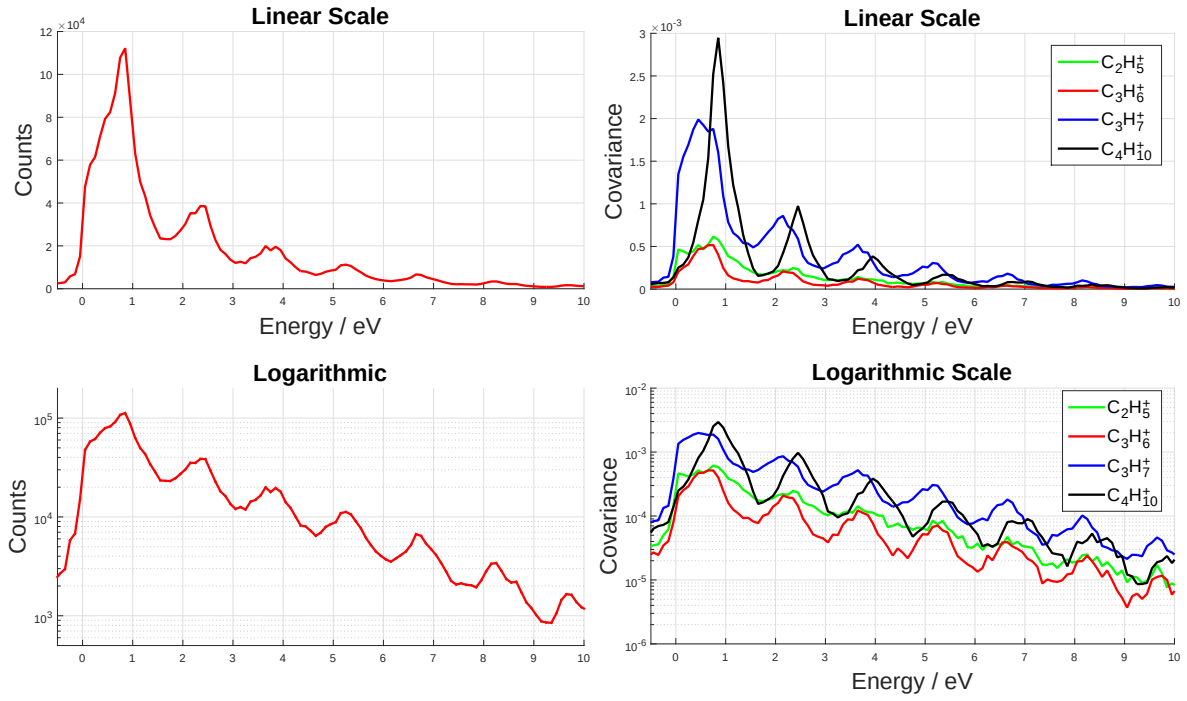

Figure 2.30: Left: integrated photoelectrons spectrum of n-butane ionized with 800 nm. **Right**: PEPICO spectrum of n-butane (covariance mapping was used to process the data). This experiment is described in detail in section 3.1. (eiTOF_0541-eiTOF_0545)

As mentioned above the covariance method has the advantage of a good signal to noise ratio even for small measuring times. If there is a background that has to be subtracted there are difficulties using the covariance method. This can happen in a pump-probe experiment for example. Here the pump only and the probe only signals need to be subtracted to isolate the pump-probe signal. The reason for the difficulties is that a rise of the signal causes a non linear rise of the covariance. So the subtraction of the covariance signals causes an error. The magnitude of this error is difficult to estimate. Calculating this estimate requires a big theoretical effort and a profound knowledge about this topic. This topic is not treated within this thesis. If a subtraction must be done one is forced to measure at very low count rates(<0.3 ionization events per shot). In this case the subtraction works because working at low count rates makes a linear approximation of the rise of the covariance as a function of the signal work. This is necessary for the subtraction not to cause a big error.

An estimate for the error of subtractions at high count rates would be very helpful. Maybe even a correction factor can be introduced in the future to make the subtraction work at high count rates. This would help to make the covariance method's advantage of short

measuring times count for pump probe experiments.

2.4.5 Characterization Measurement on O_2 and Acetone

As a proof that the PEPICO detection and data analysis work, measurements on an air+acetone gas mixture were done to separate the ATI spectra of O_2 ($IP_{0_2} = 12.1\,\mathrm{eV}$) and acetone ($IP_{(CH_3)_2CO} = 9.7\,\mathrm{eV}$). The ionization was done using 800 nm ($E_{\mathrm{phot}} = 1.55\,\mathrm{eV}$). O_2 and acetone are ideal for this kind of experiment because their ATI spectra should be clearly separated according to their ionization potentials:

$$O_2 : 7 \cdot E_{\mathrm{phot}} - IP_{0_2} = -1.25\,\mathrm{eV} \tag{2.31}$$

$$(CH_3)_2CO : 6 \cdot E_{\mathrm{phot}} - IP_{(CH_3)_2CO} = -0.4\,\mathrm{eV} \tag{2.32}$$

These calculations predict a shift of 0.85 eV of the two spectra. A measurement with 10^6 runs was taken using a mean laser power of 65 mW. The data analysis was done using the coincidence method.

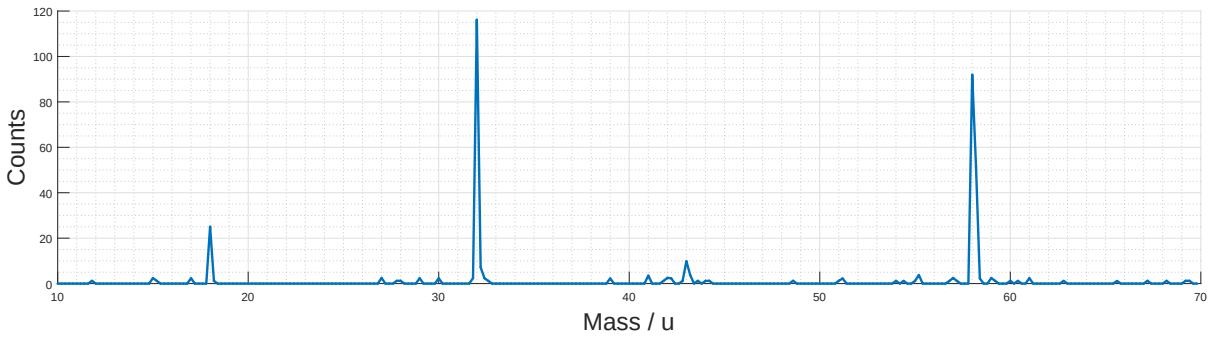

Figure 2.31: Mass spectrum of the air+acetone gas mixture using 800 nm.(eiTOF_0211)

Figure 2.31 shows the mass spectrum of the investigated gas mixture. The amounts of air and acetone in the gas mixture have been chosen the way $(CH_3)_2CO^+$ and O_2^+ are by far the biggest components of the mass spectrum and contain about the same amount of counts. So the signal to noise ratio of the mass resolved electron spectra will be about the same for the two molecules and there only few ionization events of other molecules that could cause false coincidences and therefore force us to go to even lower count rates. The peak at 18 u is assigned to H_2O^+, the one at 32 u to O_2^+ and the one at 58 u to the acetone parent ($(CH_3)_2CO^+$). H_2O^+ and O_2^+ are components of air. There is only a very

small peak at 28 u which is assigned to N_2^+ and CO_2^+. By volume, air contains ≈ 78% nitrogen, which is the vast majority. But still the oxygen peak is about two orders of magnitude higher despite of the fact that air only contains ≈ 21% oxygen. The reason for this behavior is the higher IP of N_2. It amounts to $IP_{N_2} = 15.6\,\text{eV}$. So eleven 800 nm (1.55 eV) photons need to be absorbed to ionize N_2, which is three more than ionizing O_2 ($IP_{0_2} = 12.1\,\text{eV}$) requires. This makes this process much less probable and results in a smaller N_2^+ mass peak compared to the O_2^+ peak. The very small peaks at 15 u and 43 u are assigned to the fragments of acetone.

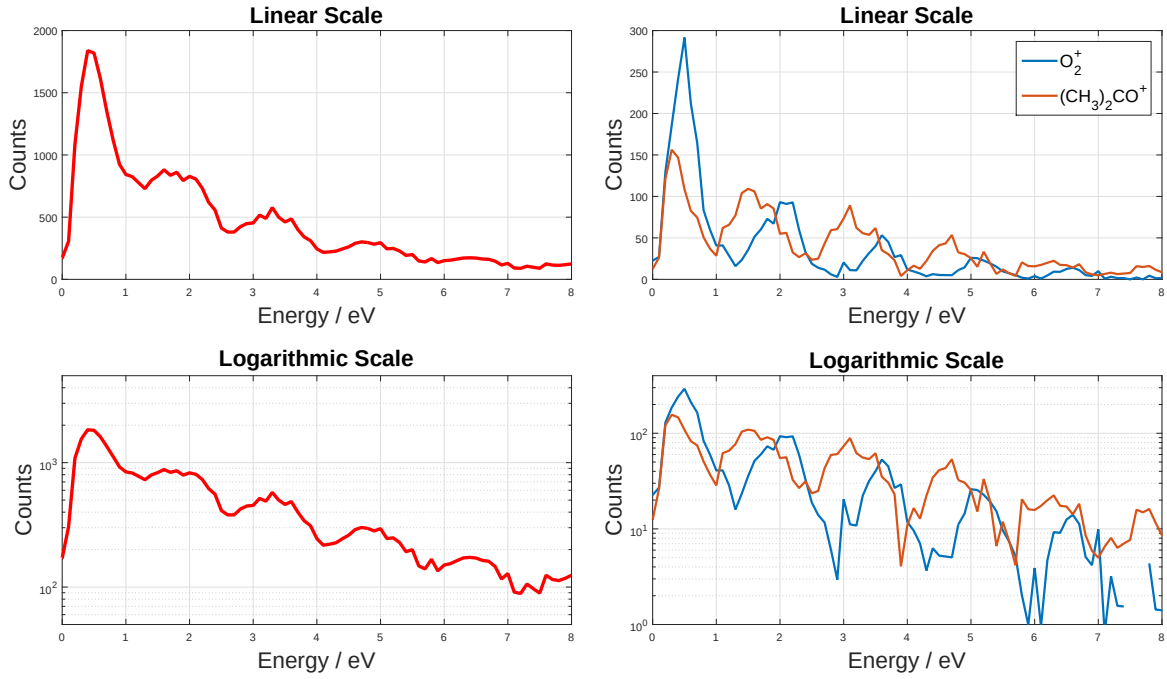

Figure 2.32: Total electron spectrum and PEPICO plot using the coincidence method. The gas in the vacuum chamber contained air and acetone. **Left**: total electron signal. **Right**: ion mass resolved electron energy spectra. Orange line acetone parent ion 58 u. Blue line O_2^+ ion 32 u. (eiTOF_0212-eiTOF_0221)

Figure 2.32 shows that it is possible to resolve the ATI spectra of two different species of ions. The total electron spectrum on the left shows the typical ATI structure of equidistant exponentially decreasing peaks. It is not clearly visible that the spectrum originates from different molecules. The right plot shows the ion mass resolved electron spectra which have been created using the coincidence method. As expected the ATI structures of O_2 and $(CH_3)_2CO$ are shifted to each other. The shift is about 0.8 eV. This matches the predicted value very well. The signal corresponding to O_2 decays faster than the acetone

signal. The reason is that ionizing O_2 is an eight photon process while ionizing acetone is a seven photon process. In the logarithmic plot the two different slopes are easy to see. It has been shown that it is possible resolve the photoelectron spectra of two different molecules with the help of the apparatus and coincidence data analysis.

2.5 Matlab Programs

In this section the Matlab programs that are used to record and process the measurement data are described.

2.5.1 RMT(runs,eOi)

Communicates with the digitizer. It is used to start a measurement. A binary file (eiTOF_xxxx) is created. It contains the time resolved digitized voltage levels for each shot of the measurement.
Input parameters are:

- **runs:** the number of laser shots contributing to the measurement
- **eOi:** defines whether an ion or electron spectrum is measured

Depending on eOi SetupIons.m or SetupElectrons.m is loaded. In these files several measurement parameters are set. SetupIons.m and SetupElectrons.m differ mainly in the segmentsize. It defines the number of data points recorded after one laser shot. As electrons are much lighter than ions the are much faster and therefore hit the detector before the ions do. Thats why a lower segmentsize can be set for electron measurements. The segmentsize defined in SetupIons.m and SetupElectrons.m are 1024 and 20 000 which equals $1.024\,\mu$s and $20\,\mu s$ for a samplerate of $10^9 \cdot \frac{1}{s}$. The samplerate can also be set in the setup files. PEPICO measurements are taken using the ion settings. An info file (eiTOF_info.txt) is created. It contains the settings defined in the setup file.
Output:

- **eiTOF_xxxx.bin:** Binary file containing the time resolved digitized voltage levels for each shot of the measurement
- **eiTOF_info.txt:** Info file where the settings of the digitizer are listed

2.5.2 eiTOF_fileread_02(filename)

applies a peak finder algorithm on ion TOF and electron TOF measurements.
Input:

- **eiTOF_xxxx.bin:** The binary file created by RMT
- **eiTOF_info.txt:** The info file created by RMT

The binary file and the info file created by RMT are loaded. The data from the binary file is read in stacks so the amount of memory needed is sufficiently small. A constant discriminator peak finder is applied to detect the peaks of each trace. If the voltage exceeds the discriminator level a peak is found at the corresponding time.
Output:

- **eiTOF_xxxx_hist .txt:** Contains the total number of hits in each time bin
- **eiTOF_xxxx_list.txt:** For each trace the times where hits appear are listed
- **eiTOF_xxxx_ansum.txt:** Contains the sum of voltages over all traces at each time bin
- **(eiTOF_xxxx_filereadinfo.txt:** the used discriminator level is listed

To process PEPICO measurements eiTOF_fileread_PEPICO_step is applied.

2.5.3 eiTOF_fileread_PEPICO_step(filename,delta_t)

is used to find peaks in data of PEPICO measurements.
Input parameter are:

- **filename:** string, name of the binary file created with RMT for example: 'eiTOF_1234.txt'
- **delta_t:** gives the difference of delay 5 to 4300 ns in ns. For example: if delay5 is 3800 ns delta_t has to be set to 500.

delta_t determines the time the high voltage is switched on (HVon = 700 ns + delta_t) and off (HVoff = 2200 ns + delta_t). The parameter delta_HVoff is set to 150 ns. It gives the time before and after HVoff where no peaks are detected. In this time big spikes appear in the time traces. They are caused by switching off the high voltage. delta_HVoff avoids them from being detected as peaks. A constant fraction discriminator (CFD) peak

finder algorithm is used. The peaks detected before HVoff -delta_HVoff are attributed to electrons. The peaks after HVoff + delta_HVoff are associated with ions. The CFD level in the electron region is set to 0.04. In the ion region it is 0.2. The electron CFD level is higher to avoid spikes caused by switching the HV on from being detected as spikes. As the ions cause lower voltage peaks the CFD level for ions is lower to optimize the detection efficiency. This can be done because in this time regime there are no spikes from artifacts.

Output:

- **eiTOF_xxxx_hist .txt:** Contains the total number of hits in each time bin
- **eiTOF_xxxx_hist_i.txt:** Contains the number of hits in each time bin associated with ions (t> HVoff+ delta_HVoff).
- **eiTOF_xxxx_hist_e.txt:** Contains the number of hits in each time bin associated with electrons (t< HVoff- delta_HVoff).
- **eiTOF_xxxx_list.txt :** For each trace the times where hits appear are listed
- **eiTOF_xxxx_list_i.txt:** For each trace the times are listed where hits appear that are associated with ions
- **eiTOF_xxxx_list_i.txt:** For each trace the times are listed where hits appear that are associated with electrons
- **eiTOF_xxxx_ansum.txt:** Contains the sum of voltages over all traces at each time bin
- **eiTOF_xxxx_filereadinfo.txt:** the used discriminator levels are listed

2.5.4 FRATI_plot_multi_step(filename,U,HVon,intervals,time0)

is used to plot data processed with fileread_pepico_step using the coincidence method 2.4.3. ion mass resolved electron energy spectra are created.

Input parameter are:

- **filename:** is a matrix containing file names,
  for example: ['eiTOF_1000';'eiTOF_1001';'eiTOF_1003']
- **U:** the electric potential at the interaction area for ions [Volts]

- **HVon:** is the time the high voltage is switched on [ns]
- **intervals:** is a matrix where mass windows are defined. the corresponding electron energy spectra to these windows are plotted. The first number in one line defines the lower limit of the window. The second number is the upper limit. for example: [12,14;25,27;57,59]
- **time0:** is the trigger offset described in 2.2.1

The plotted data can be saved for further analysis for example subtracting a background.

2.5.5 Covariance_part(filename,U,HVon,intervals,time0)

is very similar to FRATI_plot_multi_step. The main difference is that covariance mapping is used instead of the coincidence method to process the PEPICO data.
Input parameters are:

- **filename:** is a matrix containing file names,
  for example: ['eiTOF_1000';'eiTOF_1001';'eiTOF_1003']
- **U:** the electric potential at the interaction area for ions / V
- **HVon:** is the time the high voltage is switched on /ns
- **intervals:** is a matrix where mass windows are defined. the corresponding electron energy spectra to these windows are plotted. The first number in one line defines the lower limit of the window. The second number is the upper limit. for example: [12,14;25,27;57,59]
- **time0:** is the trigger offset described in 2.2.1

CHAPTER 3

Results

3.1 n-Butane

Channel-resolved above threshold ionization (CRATI) spectroscopy is a method that is used in the contemporary research field of molecular ionization channels and fragmentation behavior. In the CRATI method, the channel refers to the electronic state of the ion correlated with the continuum electron [6]. The ionic state can be determined indirectly using PEPICO (described in section 2.4) for certain molecules. The requirement is that each ionic state yields a different predominantly occurring fragment. If this is the case the PEPICO method is very suitable for CRATI. The detected masses provide information about the fragments and in further consequence about the populated ionic state and the kinetic energy spectrum of the correlated continuum electrons reveals the involved ionization channel. Fragment resolved photoelectron spectroscopy in the ATI regime automatically yields CRATI. The above threshold ionization is described in section 1.1.5. The kinetic energy of the liberated electrons is given by equation 1.14.

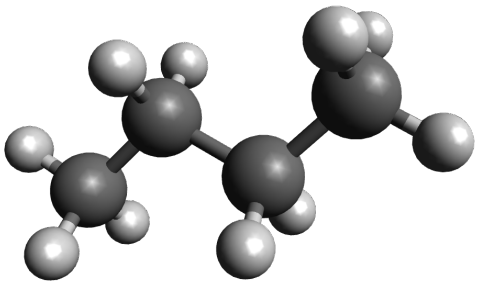

Figure 3.1: Structure of n-butane drawn with Avogadro [24] ,white balls hydrogen, black balls carbon.

N-butane (C_4H_{10}) is an alkane with an unbranched structure (figure 3.1). When n-butane

is ionized with 800 nm several ionization channels are possible. Depending on the channel the molecule fragments in a different way. This fact makes n-butane a good candidate for channel-resolved above threshold ionization spectroscopy using PEPICO. This has been done by the A. Stolow group in 2012 [6]. The result of their measurements on n-butane are shown in figure 3.2.

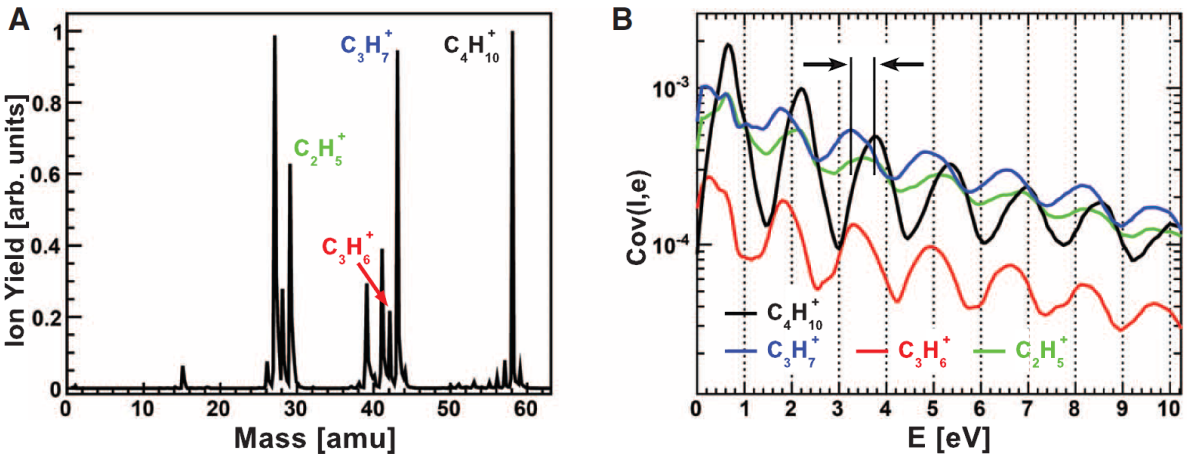

Figure 3.2: **A**: mass spectrum of n-butane ionized with 800 nm. Peak intensity = $1.6{\cdot}10^{13}$ $\frac{\mathrm{W}}{\mathrm{cm}^2}$ **B**: CRATI photoelectron spectra associated with prominent ions (parent and three fragments). Figure taken from [6]

Reproducing these measurements proofs that our spectrometer and PEPICO detection make it possible not only to resolve the electron energy spectra of two different molecules as shown in section 2.4.5 but also to resolve the electron energy spectra of fragments originating from the same molecule.

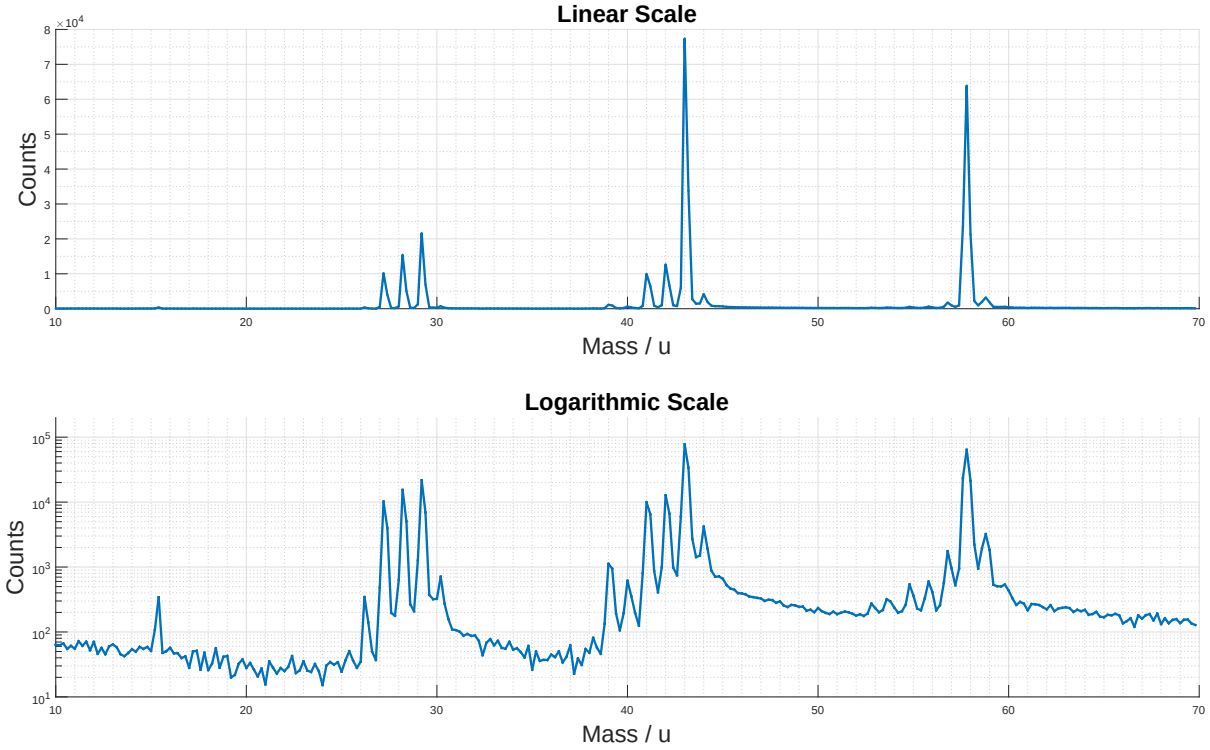

Figure 3.3: Mass spectrum of n-butane ionized with 800 nm. Pressure: $p = 3 \cdot 10^{-6}$ mbar; Laser power: $P = 35$ mW. (eiTOF_0541)

Figure 3.3 shows the mass spectrum of n-butane ionized with 800 nm measured with the apparatus described in chapter 2. The same peaks as in figure 3.2 appear but their heights are different. This can be explained by a different intensity distribution at the interaction area which influences the fragmentation behaviour. The peak at 58 u is associated with the parent ion. The small peaks at 55 u, 56 u, and 57 u are assigned to molecules with double bond and therefore a smaller number of H atoms. The 59 u peak is assigned to the parent ion with one ^{13}C isotopes. The 43 u peak is assigned to the fragment missing one CH_3 group. The 42 u and 41 u molecules miss one respectively two more hydrogen atoms. The small peaks at 39 u, 40 u and 44 u again arise due to a smaller number of H atoms and molecules containing isotopes of carbon. The peaks at 26 u 27 u, 28 u and 29 u correspond to smaller fragment missing another CH_3 group and hydrogen atoms. The 30 u peak again comes from molecules containing ^{13}C. In the paper from the Stolow group the electron spectra correlated with $C_2H_5^+$ (29 u), $C_3H_6^+$ (42 u), $C_3H_7^+$ (43 u) and $C_4H_{10}^+$ (58 u) are investigated (figure 3.2). The same was done here using covariance mapping:

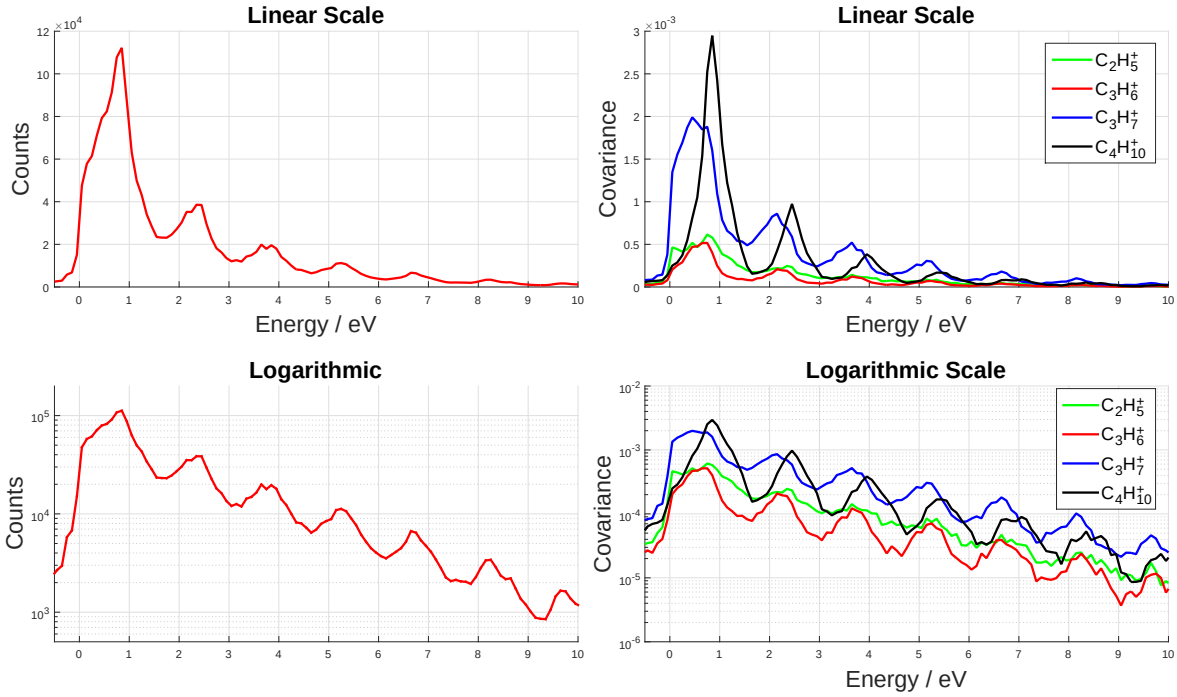

Figure 3.4: Left: Integrated photoelectrons spectrum of n-butane ionized with 800 nm. **Right**: CRATI photoelectron spectrum of n-butane. The same colors as in figure 3.2 were used for the same ions. Pressure: $p = 3 \cdot 10^{-6}$ mbar; laser power: $P = 35$ mW. (eiTOF_0541-eiTOF_0545)

Figure 3.4 shows the integrated photoelectron spectrum and the CRATI spectrum of n-butane ionized with 800 nm. The ATI structure is clearly visible in both the integrated and the mass resolved spectrum. The CRATI spectrum matches the one in figure 3.2 very well. The signal-to-noise ratio is not as good as in figure 3.2 but the data quality is sufficient to proof that the apparatus and the data procession work. The shift of the ATI combs discussed below is clearly visible. A better signal-to-noise ratio could be achieved by longer measuring times. The areas under the curves in the linear CRATI plot correspond to the peak heights in figure 3.3. The areas in the CRATI plot and the mass peak heights are not correlated linearly because the covariance does not rise linearly with the signal so only qualitative statements can be made. The most signal is coming from $C_3H_7^+$ (43 u) followed by $C_4H_{10}^+$ (58 u), $C_2H_5^+$ (29 u) and $C_3H_6^+$ (42 u). All four spectra show the same decay towards higher electron energies, which indicates that all originate from ionizations from the same order (same amount of photons).

The ATI spectra correlated to the different fragments are shifted to each other. The reason is that there are different ionic states within one photon energy above the ionic ground

state (D_0) as table 3.1 shows. The energies of the ionic states are sketched schematically in figure 3.5.

Table 3.1: Ionic states of n-butane. I_p^{FF} are measured values taken from [25]. I_p^{SS} include the calculated Stark shift [6].

Ionic state	Way of determination	Ionization potential
D_0	I_p^{FF}	11.2
	I_p^{SS}	11.0
D_1	I_p^{FF}	11.7
	I_p^{SS}	11.4
D_2	I_p^{FF}	11.7
	I_p^{SS}	11.5
D_3	I_p^{FF}	12.2
	I_p^{SS}	12.2

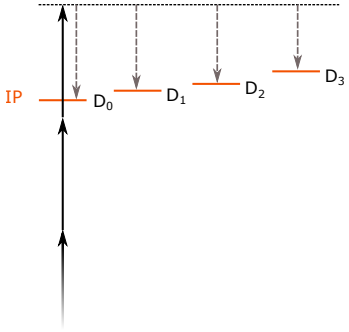

Figure 3.5: Schematic term diagram of Butane ionized with 800 nm.

Depending on which one of the ionic states listed in table 3.1 is populated the molecule fragments differently. The correlated photoelectron energy spectra differ due to the different energies of the ionic states. The parent ion $C_4H_{10}^+$ is associated with the ionic ground state (D_0). $C_3H_7^+$ and $C_3H_6^+$ are associated with the first excited ionic state (D_1) and $C_2H_5^+$ with the third excited ionic state [6].

In conclusion, we were able to reproduce the results from the Stolow group [6]. This shows that the apparatus and the data procession work perfectly. The experiment illustrates the strength of PEPICO in molecular spectroscopy. The combination of the information about the fragmentation behavior and the involved ionization channels from the electron energies provides a deep insight on the molecular processes. The method will be used for single pulse (this work) and time resolved pump-probe [1] experiments to study photoinduced dynamics in molecules.

3.2 Acetone

Acetone is an organic molecule with the formula $(CH_3)_2CO^+$ and an ionization potential of $IP = 9.7\,eV$. It is the simplest ketone. It shows a variety of photoinduced dynamics. Especially the Norrish type I reaction has been studied intensively [26–30]. This reaction is a photoinduced neutral dissociation (described in section 1.2). PEPICO is a very powerful tool in this research as it can be used to investigate the fragmentation behavior. The chemical structure of acetone is depicted in figure 3.6. Single pulse experiments using 400 nm (section 3.2.1), 266 nm (section 3.2.2) and 800 nm (section 3.2.3) pulses were performed in preparation of time resolved pump-probe experiments. The creation of the 400 nm and 266 nm pulses and their application in time resolved experiments are described within the master's thesis of Paul Maierhofer [1].

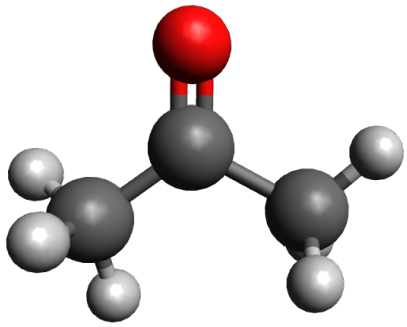

Figure 3.6: Structure of Acetone drawn with Avogadro [24],white balls hydrogen, black balls carbon, red ball oxygen.

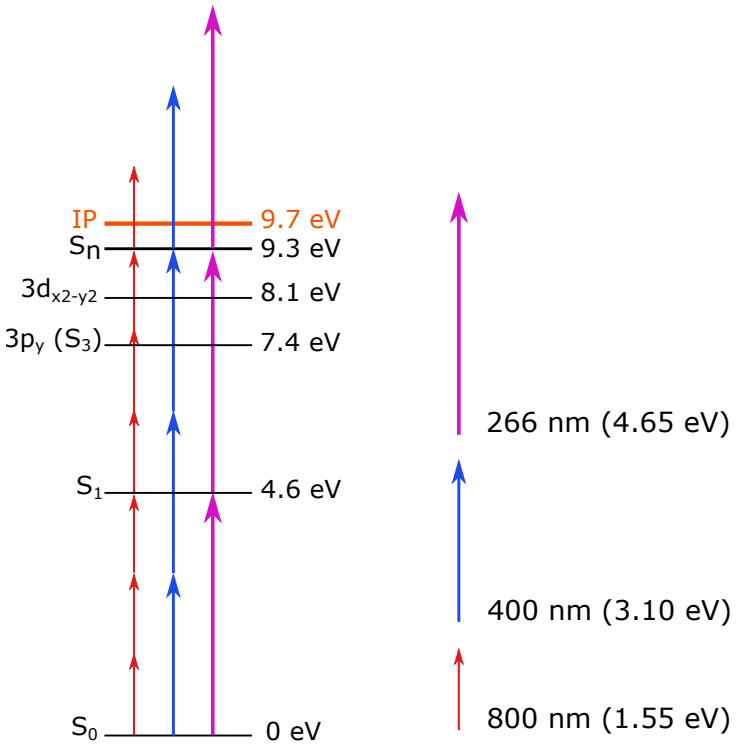

Figure 3.7: Energy level diagram of acetone in the ground state geometry including prominent states. The colored arrows illustrate the photon energies of the 800 nm, 400 nm and 266 nm pulses.

An energy level diagram of acetone in the ground state geometry is depicted in figure 3.7. The diagram includes states that are important for the interpretation of the measured spectra. The colored arrows illustrate the photon energies of the 800 nm, 400 nm and 266 nm pulses.

3.2.1 400 nm MPI

Measurements on acetone have been performed using 400 nm ionization pulses. Figure 3.8 shows the observed mass spectrum.

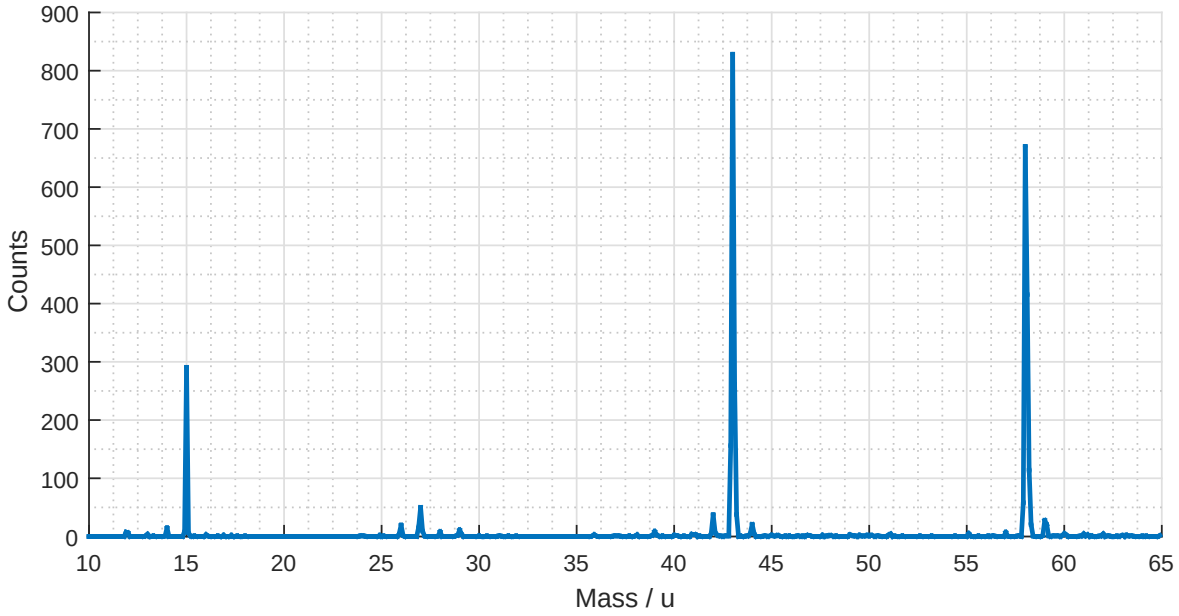

Figure 3.8: Mass spectrum of acetone ionized with 400 nm. Pressure: $p = 2 \cdot 10^{-7}$ mbar; Laser power: $P = 80$ mW. (eiTOF_0762)

There are three major peaks in the mass spectrum depicted in figure 3.8. The peak at 58 u is assigned to the acetone parent ion ($(CH_3)_2CO^+$). The peaks at 43 u and 15 u arise due to fragmentation. For acetone the predominant way of fragmentation is a C-C bond breakage. The resulting fragments are acetyl (CH_3CO) with a mass of 43 u and its counterpart methyl (CH_3) with a mass of 15 u. When an acetone parent ion fragments it is much more likely that the positive charge stays at the bigger acetyl than on the smaller methyl molecule. This is why the 43 u peak is much higher than the 15 u peak. The integrated photoelectron spectrum and the PEPICO spectrum of acetone ionized with

400 nm are shown in figure 3.9.

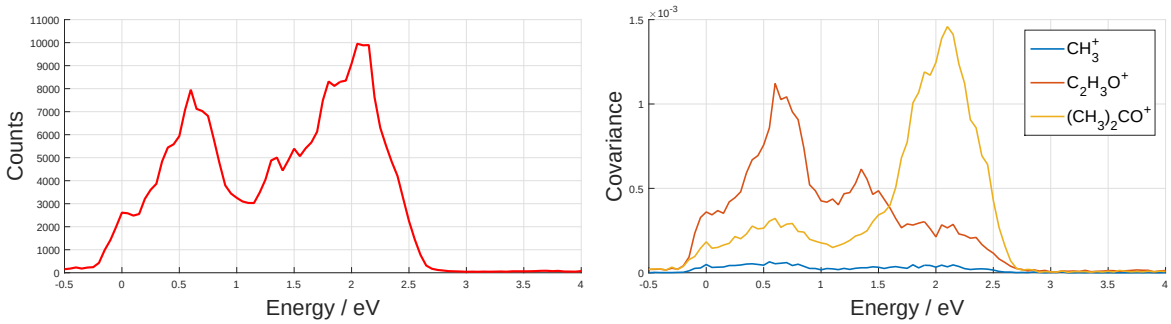

Figure 3.9: Left: Total photelectron spectrum of acetone ionized with 400 nm . **Right**: Fragment resolved photoelectron spectrum of acetone ionized with 400 nm. Pressure: $p = 5 \cdot 10^{-6}$ mbar; Laser power: $P = 40$ mW. (eiTOF_1835)

The integrated photoelectron spectrum in figure 3.9 shows two peaks. The structure at higher energies (onset energy 2.7 eV) is explained by a direct four photon ionization. The energy of four photons (4·3.1 eV = 12.4 eV) minus the IP of acetone in the ground state geometry ($IP = 9.7\,eV$) results in the observed photoelectron energy of 2.7 eV. The structure that peaks at 0.6 eV cannot be explained by the population of a dissociative excited ionic state similar to the behavior of n-butane discussed in section 3.1. The first excited ionic state of acetone has an energy of (12.5 ± 0.1) eV , as measurements on synchrotrons using the threshold PEPICO technique show [31]. If this first excited ionic state was populated with four photons the resulting electron energy would be significantly lower than the observed 0.6 eV. A population of this state with five photons would cause electrons with energies of ≈ 3 eV.

The PEPICO spectrum (data analysis using covariance mapping) in figure 3.9 reveals a third peak at 1.4 eV. This peak and the peak at 0.6 eV are correlated with the acetyl (CH_3CO^+) fragment. The peak at 2.1 eV assigned to the direct ionization correlates with the parent. The reason why the direct ionization leads to parent ions is that there is no conversion of electronic energy to vibrational energy, which would facilitate fragmentation. The ionization happens within a very short period of time. There is no time for any relaxation dynamics of possible resonant intermediate states as the next photon is absorbed very shortly after the state is populated. This is the same effect as in the experiment described in section 1.2 where the photoelectron spectrum is measured for different pulse durations [11]. The ionization takes place on a shorter time scale than the

molecular dynamics.

The fragment structure at 2.2 eV is caused by subsequent excitation. The parent ion is resonantly excited into a higher ionic state. The molecule is not stable in this state and fragments (described in section 1.2).
Figure 3.10 shows a schematic energy level diagram of acetone and excited-state energy curves of acetone along the r(CO) bond-stretching coordinate [28] to illustrate the consideration for the explanation of the fragment structure in the PEPICO plot in figure 3.9.

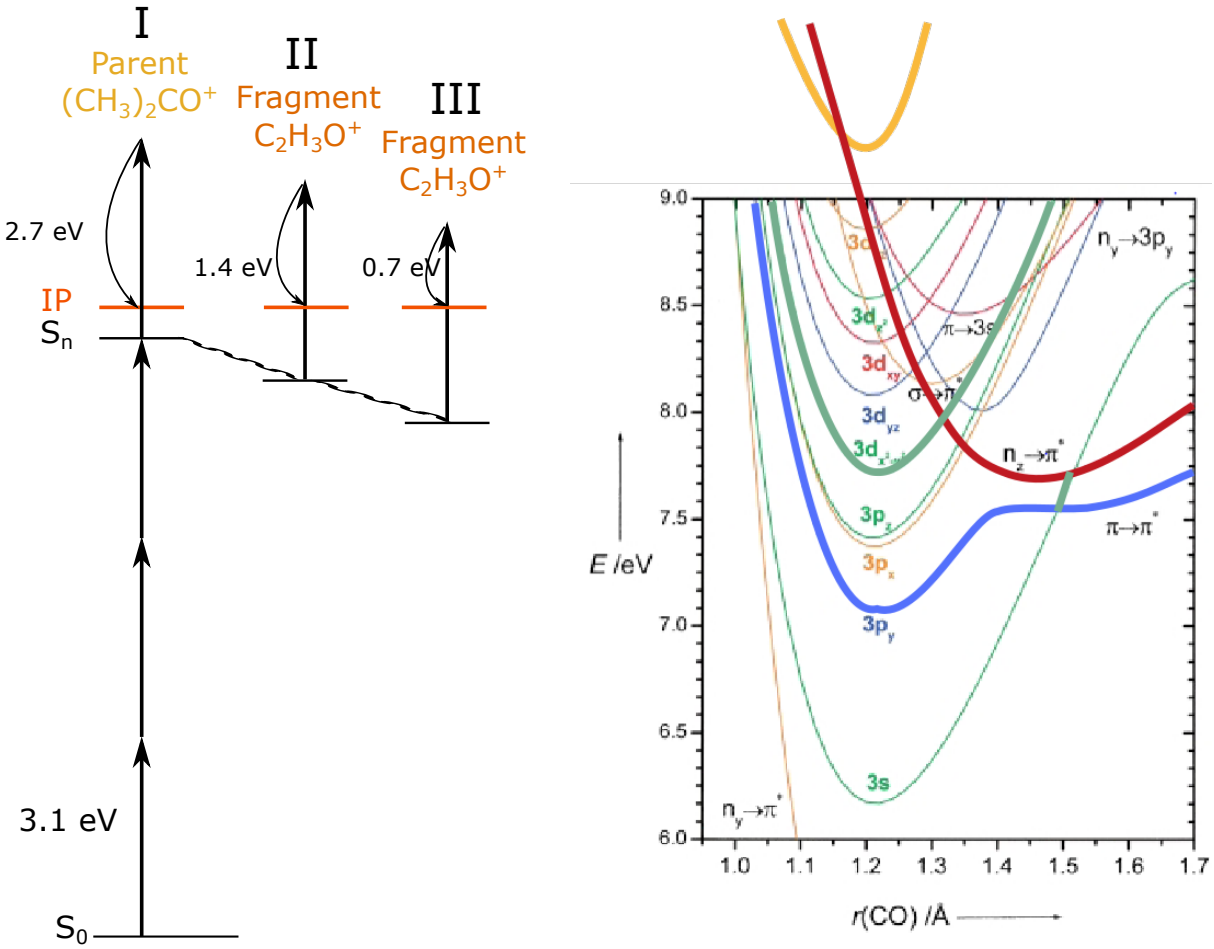

Figure 3.10: Left: Schematic energy level diagram of acetone and suggested relaxation paths. **Right**: This figure was taken from [28]. It shows the potential energy curves of acetone along the r(CO) coordinate relative to the S_0 minimum. The calculations were done using time dependent density functional theory (B3LYP/6-31+G(d)). The different colors represent different symmetries: A_1 blue, A_2 orange, B_1 red, and B_2 green.

A possible explanation for the two parent peaks is suggested by results of time resolved measurements using 266 nm pump 400 nm probe pulses [1]. Here a high lying ensemble

of Rydberg states (S_n at 9.3 eV) is populated by two 266 nm photon, which provide the same amount of energy as three 400 nm photons do. As these high lying states are energetically very close and the laser pulses' spectral distributions (given in table 2.1) are wide, multiple states are populated. The high lying yellow bold line in the right part of figure 3.10 illustrates the S_n ensemble. Similar structures as in the 400 nm experiment described here were observed in time resolved experiments.

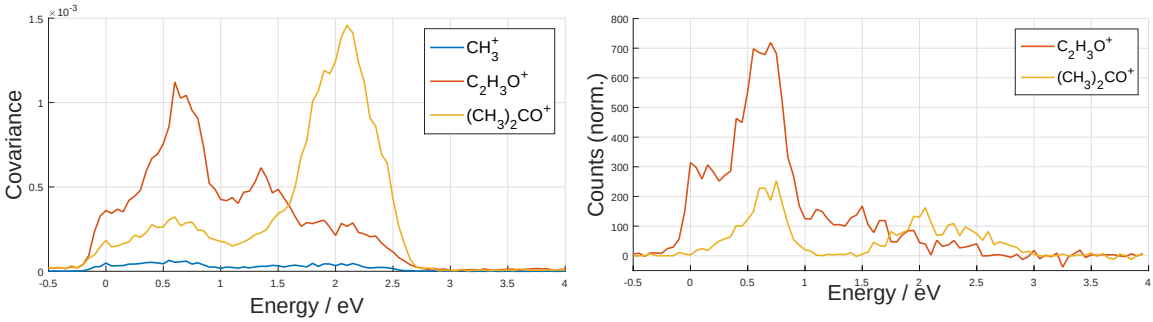

Figure 3.11: Comparison between the 400 nm single pulse experiment data and the 266 nm-400 nm pump-probe data. **Left**: Fragment resolved photoelectron spectrum of acetone ionized with 400 nm (the same as in figure 3.9). **Right**: Fragment resolved pump-probe photoelectron spectrum of acetone. Pump wavelength: 266 nm; Probe wavelength: 400 nm; Timedelay: 300 fs. (eiTOF_1835; eiTOF_1802-eiTOF_1831)

The 400 nm PEPICO spectrum and the 266 nm pump 400 nm probe PEPICO spectrum are depicted next to each other in figure 3.11. The delay between pump and probe pulse is 300 fs. The two spectra show qualitatively the same structures. The parent peak at 2.1 eV is much smaller in the pump-probe spectrum. The reason is that there is much more time between the population of the S_n with two 266 nm photons and the ionization with one 400 nm photon than in the 400 nm single pulse experiment were both processes happen within one pulse. So a lot of the S_n population has vibrationally relaxed at the time the probe pulse ionizes the molecule. The vibrational excitation facilitates fragmentation. A detailed discussion of the time resolved spectra is done by Paul Maierhofer within his master's thesis [1].

The results of the time resolved measurements lead us to the following interpretation of the two fragment peaks: After the population of the S_n (highest lying bold yellow potential energy curve with a minimum at $\approx$ 9.3 eV in the right part of figure 3.10) a relaxation via conically intersecting valence states (bold red curve) takes place. The relaxation yields population of the $3d_{x^2-y^2}$ state (bold green line) and the $3p_y$ state (bold

blue line). These states are also Rydberg states. The energies of these two states fit the observed peak positions the best. These energies where determined in high-resolution VUV photoabsorption spectroscopy experiments using synchrotron radiation [32]. When the molecule relaxes from the S_n state to lower states, electronic energy is converted to vibrational energy. This is why ionizing from $3d_{x^2-y^2}$ or $3p_y$ leads to fragmentation. The fact that the two peaks assigned to ionization paths through these two Rydberg states correlated with the acetyl molecule strongly indicate a relaxation dynamic as suggested here. The parent structure below the fragment peaks can be explained by efficient internal conversion of energy to vibrations that do not facilitate fragmentation.

3.2.2 266 nm MPI

Measurements on acetone have been performed using the frequency tripled output laser pulses (266 nm). The photon energy at this wavelength is 4.65 eV. The 266 nm pulses (>100 fs) are significantly longer than the 800 nm fundamental pulses (<25 fs). The pulses are broadened due to first and second order chirps when they pass the crystals and the lenses. For 266 nm even the influence of air is mentionable [1]. The mass spectrum of acetone ionized with 266 nm pulses is depicted in figure 3.12. It shows that the wast majority of ionized acetone molecules fragments. The acetyl peak (43 u) is clearly dominant. The methyl peak (15 u) and the acetone parent peak (58 u) are much smaller than in the mass spectrum of acetone ionized with 400 nm (figure 3.8).

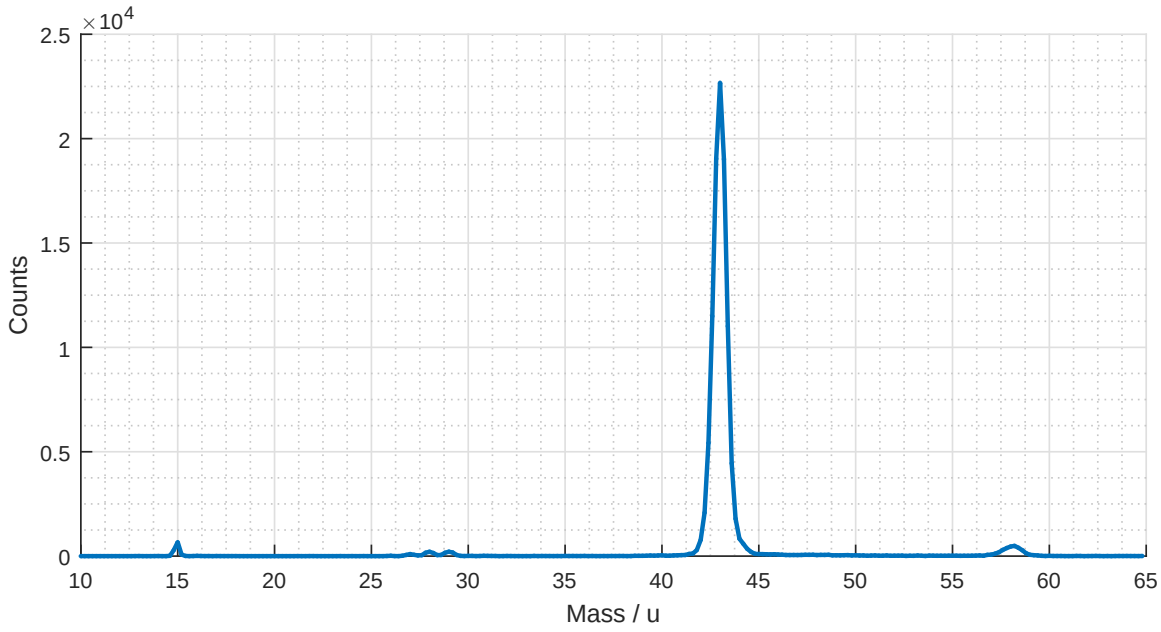

Figure 3.12: Mass spectrum of acetone ionized with 266 nm. Pressure: $p = 5 \cdot 10^{-6}$ mbar ;laser power: $P = 13$ mW. (eiTOF_1036)

The electron background ($p < 5 \cdot 10^{-10}$ mbar) spectrum depicted in figure 3.13 shows a big structure at low energies (<1 eV). These slow electrons originate from scattered 266 nm photons hitting the repeller or the wall of the chamber. The energy of a 266 nm photon is higher than the work function of many materials so electrons can be removed from solids. The total photoelectron spectrum in figure 3.14 also shows this background structure at low energies. The lack of this structure in the PEPICO plot proofs that these slow electrons do not correspond to the ionization of acetone. As mentioned before, two 266 nm have the same energy as three 400 nm photons, so xonsidering the parity section rule similar ionization channels as in the 400 nm experiment (section 3.2.1) should apply here. Either direct ionization takes place which results in the formation of a parent ion or the S_n

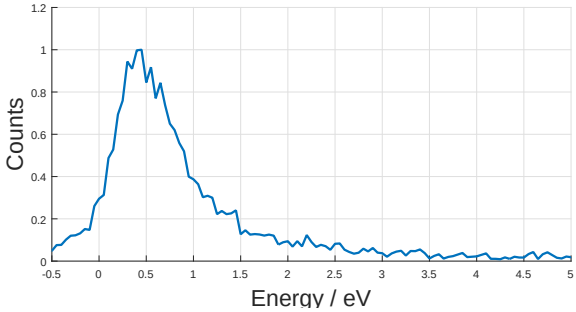

Figure 3.13: Electron background spectrum. Laser wavelength: 266 nm; Pressure: $< 5 \cdot 10^{-10}$ mbar. (eiTOF_0780)

state (9.3 eV) is resonantly populated and relaxation processes take place. The absorption of an additional photon in the relaxed states yields ionization and fragmentation. The 266 nm PEPICO spectrum qualitatively looks very similar to the 400 nm spectrum which supports this theory. The 266 nm spectrum is shifted to higher energies by ≈ 1.55 eV compared to the 400 nm spectrum. This shift is caused by the different amount of energy provided by three 266 nm photons ($3 \cdot 4.65\,\text{eV} = 13.95\,\text{eV}$) compared to four 400 nm photons ($4 \cdot 3.10\,\text{eV} = 12.40\,\text{eV}$) which are required for the ionization of acetone. The much smaller parent signal suggests that the direct ionization channel is less probable than in the 400 nm experiment. This is in line with the fact that the 266 nm pulses are relatively long. So it is unlikely that three photons are absorbed within a short period of time, which is necessary for the direct ionization. The S_n is depopulated due to relaxation dynamics before an ionizing photon is absorbed. So electronic energy is converted into vibrational energy and fragmentation upon ionization gets more probable. The peaks at 2.4 eV and 3.0 eV in the fragment spectrum are assigned to the same processes as the fragment peaks in the 400 nm spectrum described in section 3.2.1. Population of the S_n, relaxation into $3d_{x^2-y^2}$ and $3p_y$ and ionization into the ionic ground state D_0.

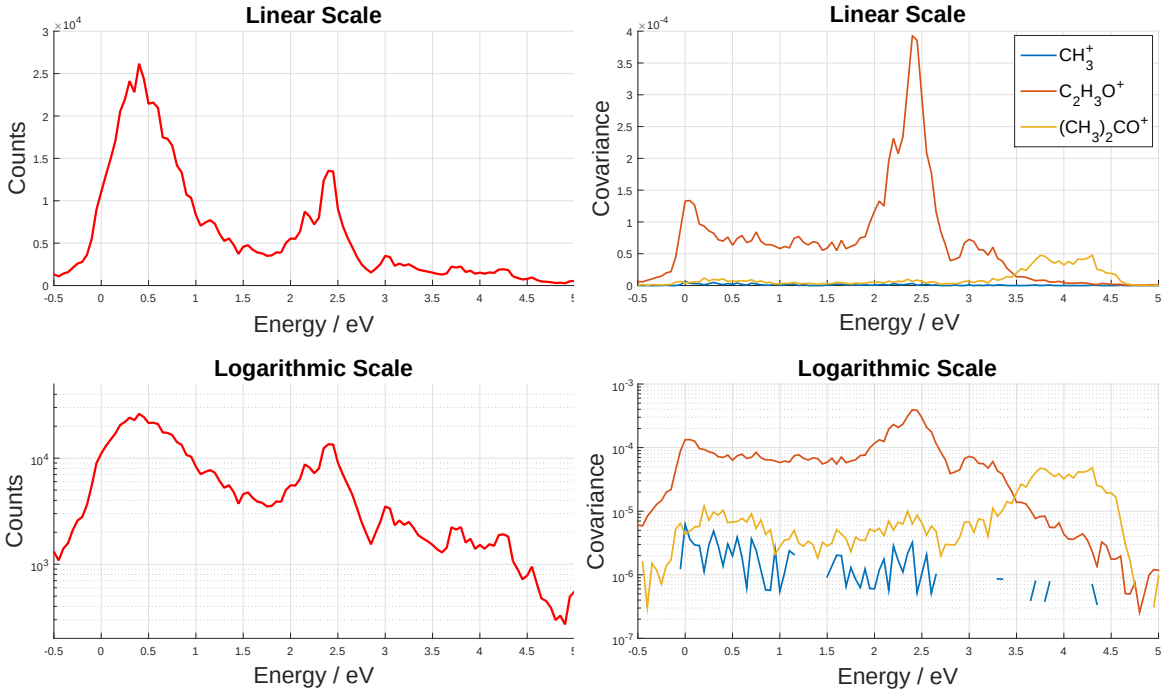

Figure 3.14: Left: Total photelectron spectrum of acetone ionized with 266 nm . **Right**: Fragment resolved photoelectron spectrum of acetone ionized with 266 nm. Pressure: $p = 5 \cdot 10^{-6}$ mbar; Laser power: $P = 13$ mW. (eiTOF_1036-1040)

There is a small peak at very low energies ($< 0.1\,\mathrm{eV}$) in the fragment spectrum. This peak can be interpreted as the population of the first excited ionic state (D_1 at $(12.5 \pm 0.1)\,\mathrm{eV}$ [31]) out of the $3d_{x^2-y^2}$ at 8.1 eV [32]. A photon from the low energy part of the spectrum could resonantly populated this excited ionic state after the relaxation from the S_n into the $3d_{x^2-y^2}$ state. The lack of this peak in the parent spectrum is clearly visible in the logarithmic plot. This strongly indicates that the peak is not caused by any false covariance effect due to the background electrons. If this was the case the structure would be present in both the fragment and the parent spectrum.

3.2.3 800 nm ATI

Acetone has been ionized with 800 nm. The longer wavelength compared to the experiments discussed in section 3.2.1 and 3.2.2 yields a higher U_p and a lower Keldysh parameter γ. This is an ATI-regime-experiment. The measured mass spectrum is depicted in figure 3.15.

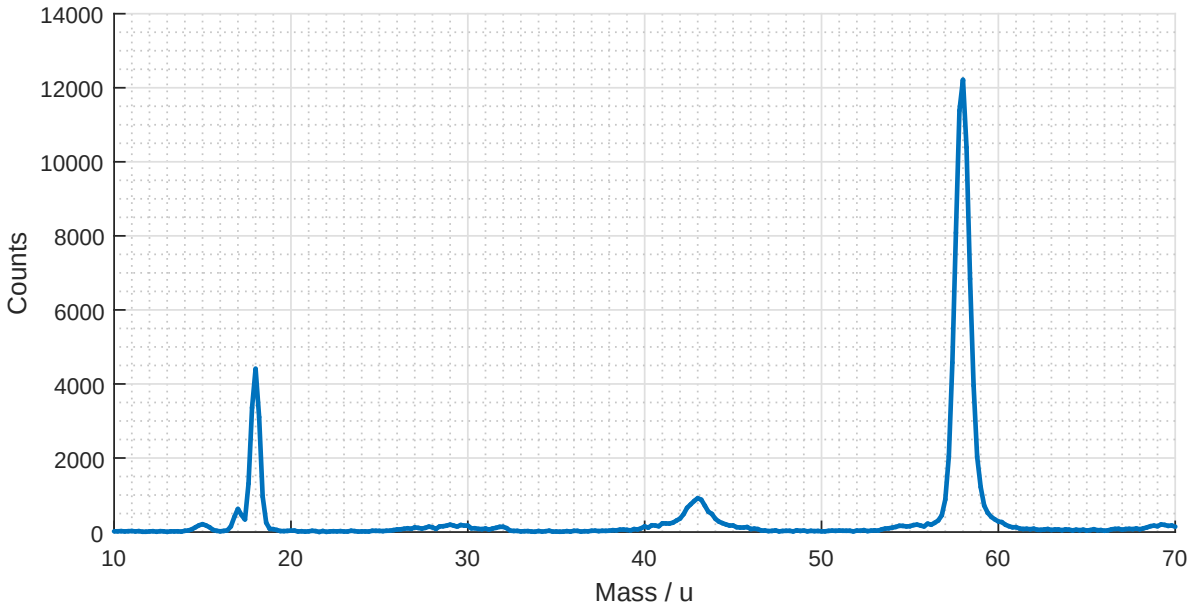

Figure 3.15: Mass spectrum of acetone ionized with 800 nm. Pressure: $p = 5 \cdot 10^{-9}$ mbar ;laser power: $P = 80\,\mathrm{mW}$. (eiTOF_0262)

The parent ion (58 u) is dominant in the spectrum (figure 3.15). The acetyl fragment ion ($C_2H_3O^+$) appears at 43 u. There are about five percent of the parent counts associated

with the acetyl fragment. The signal at 15 u is assigned to the methyl fragment ion (CH_3^+). The methyl signal is even lower than the acetyl signal. The reason for this asymmetry is that the charge tends to stay at the acetyl upon fragmentation. The peak at 18 u is assigned to background from water. Figure 3.16 shows the integrated photoelectron spectrum and the ATI spectra of the different ions on linear and logarithmic scales.

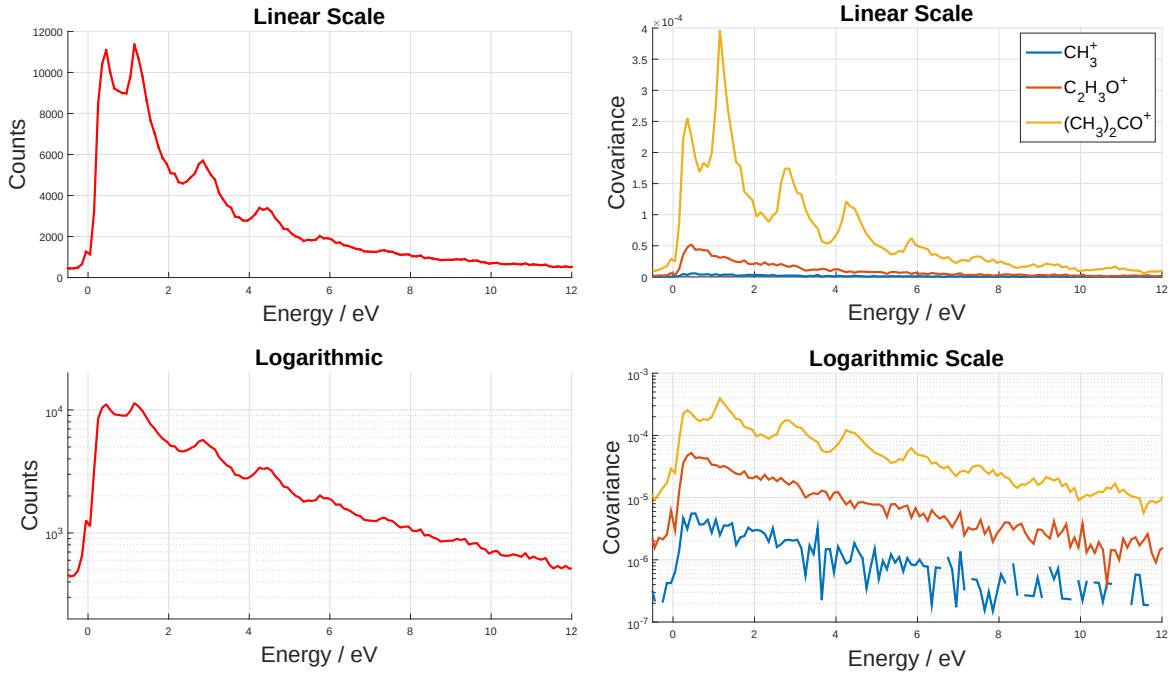

Figure 3.16: Left: Total photelectron spectrum. **Right**: ATI spectra for acetone parent ($(CH_3)_2CO^+$), acetyl fragment ($C_2H_3O^+$) and methyl fragment (CH_3^+). Pressure: $p = 5 \cdot 10^{-9}$ mbar; Laser power: $P = 80$ mW. (eiTOF_0262-eiTOF_0266)

The parent electron energy spectrum in figure 3.16 shows the typical ATI structure. The spectra correlated with acetyl and methyl do not show the ATI typical modulation. There is only an exponential decay. The two peaks in the fragment spectrum of the 400 nm experiment (figure 3.9) could contribute to this effect. The distance of one peak to the other is 0.7 eV, which is very close the one half of the ionization photon energy used here (1.55 eV). If the same relaxation process as in the 400 takes place this is good explanation for the canceling of the ATI peaks. If there are two peaks with the distance of one half photon energy reoccurring at distances that are integer multiples of the photon energy, the contrast of the ATI peaks decreases significantly. It is not sure if this process takes place when ionizing with 800 nm pulses. A different number of photons could populate the S_n state much less efficiently although the energy of six 800 nm photons is the same

as the energy of three 400 nm photons. The 800 nm pulses are much shorter than the 400 nm pulses so it is questionable whether there is enough time for the relaxation process mentioned in section 3.2.1 within one 800 nm pulse. Another reason for the vanishing ATI peaks could be direct multiphoton ionization into the electronically excited states of the parent cation and a wide energy distribution of the final vibrational state after the ionization determined mostly by the Franck-Condon factor. This effect was observed investigating ethanol (C_2H_5OH) [33].

3.3 Perylene

With perylene a more complex organic compound was investigated. Perylene is a polycyclic aromatic hydrocarbon (252 u). Its structure is shown in figure 3.17. It has an excited state 3.1 eV above the ground state and an ionization potential of $IP = 6.96\,\mathrm{eV}$ [34]. It is solid at room temperature so it has to be evaporated to be investigated with the used experimental setup. To evaporate the solid the oven described in [12] was used. Perylene was investigated using laser pulses with a center wavelength of 800 nm and various laser powers. Figure 3.18 shows the mass spectra of perylene for various laser powers. The peak at 252 u is assigned to the parent ion. The molecule fragments in several ways. The structures between 130 u and 250 u are assigned to the products of fragmentation. The peak at 126 u is associated with the double charged parent ion. The 125 u is ascribed to the double charged 250 u fragment. The peaks at lower masses are associated with lighter fragments, multiply charged fragment or parent ions. The plot shows that the mass resolution is sufficiently high to distinguish fragments with one u difference in mass (a split off of one hydrogen atom). To monitor the power dependencies of certain peaks, the counts within one peak (center ± 0.4 u) were integrated and plotted over the power in double logarithmic plots as described in 1.1. These plots are depicted in figure 3.19.

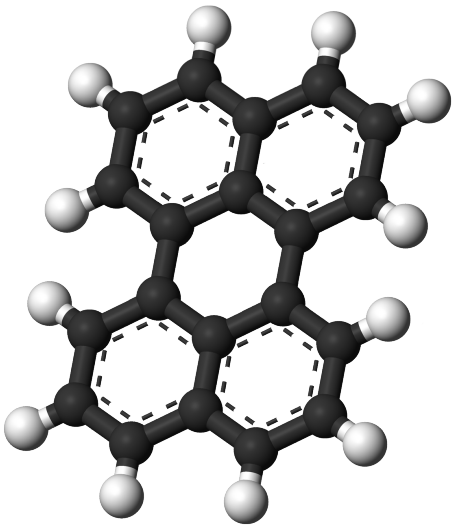

Figure 3.17: Chemical structure of perylene. White balls hydrogen; black balls carbon. Figure taken from `https://en.wikipedia.org/wiki/Perylene`

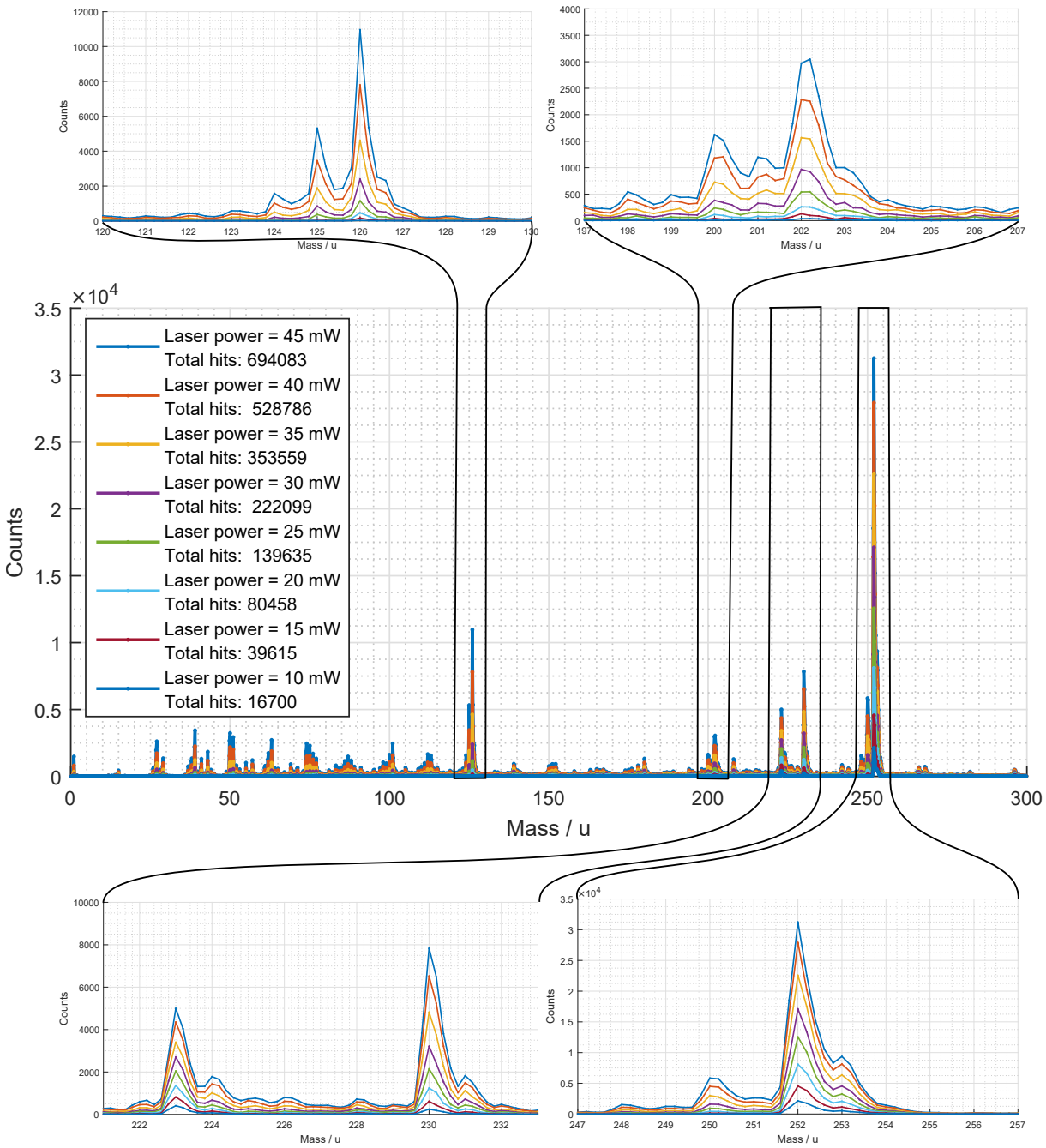

Figure 3.18: Mass spectrum of perylene ionized with 800 nm for various laser powers. The prominent peaks discussed below are illustrated in zoom spectra. (eiTOF_0407-eiTOF_0414)

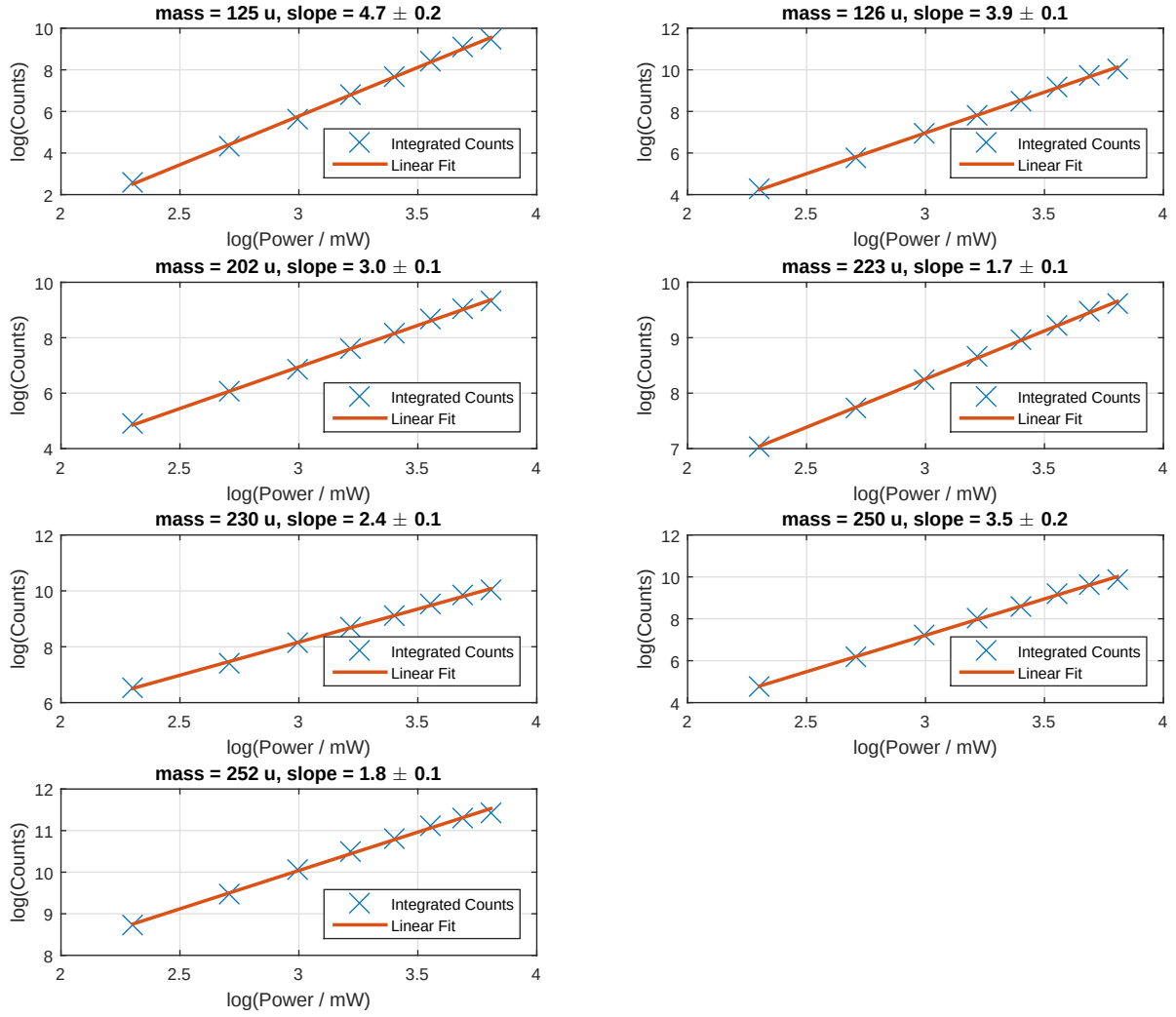

Figure 3.19: Power dependencies of prominent peaks in the perylene mass spectrum. Ionization wavelength is 800 nm.

Figure 3.19 shows the power dependent number of counts of prominent mass peaks in double logarithmic plots. The centers of the peaks and the slopes in the double logarithmic plots are given in the title of the plots. The slopes of the peaks differ strongly between 1.74 for the 223 u peak and 4.68 for the 125 u peak. As the IP of perylene amounts to 6.96 eV the minimum number of 800 nm (1.55 eV) photons required for the ionization is five. The resonant state at 3.1 eV and possible additional resonant higher states cause smaller orders of power dependencies than equation 1.2 would predict. The similar slopes of the 223 u signal and the parent (252 u) signal suggest that these two ions arise from the same process. The slopes of the 202 u, the 230 u and 250 u peaks are significantly higher

and probably correlate with the population of excited ionic states. The peaks which are assigned to double charged ions (125 u and 126 u) show the highest slopes. This fits the expectations because it takes a lot of energy(high number of photons) to form double charged ions.

Photoelectron spectra of perylene have been taken using 800 nm and different laser powers. These spectra are plotted on a linear and on a logarithmic scale in figure 3.20. The laser powers and the total hits are given in the legend. The number of total hits rise with higher powers. The spectra show the typical ATI modulation with distances of one photon energy (1.55 eV). The spectra taken with higher laser powers shift to lower energies. The reason for this shift is the intensity dependent ponderomotive potential U_p described in 1.1.1. The kinetic energy of ATI electrons is given by equation 1.14.

The fragment resolved PEPICO spectra in figure 3.21 reveal that the ATI modulation only appears in the photoelectron spectrum correlated with the 252 u parent ion. The reason for the diffuse structures correlated with the other ions could be similar to the ones for the diffuse acetone fragment structure discussed in section 3.2.3.
Time resolved pump-probe experiments and the wide range of accessible wavelength provided by the OPA will give a deeper insight on the processes that cause the smearing of ATI structures in the photoelectron spectra correlated with fragment ions.

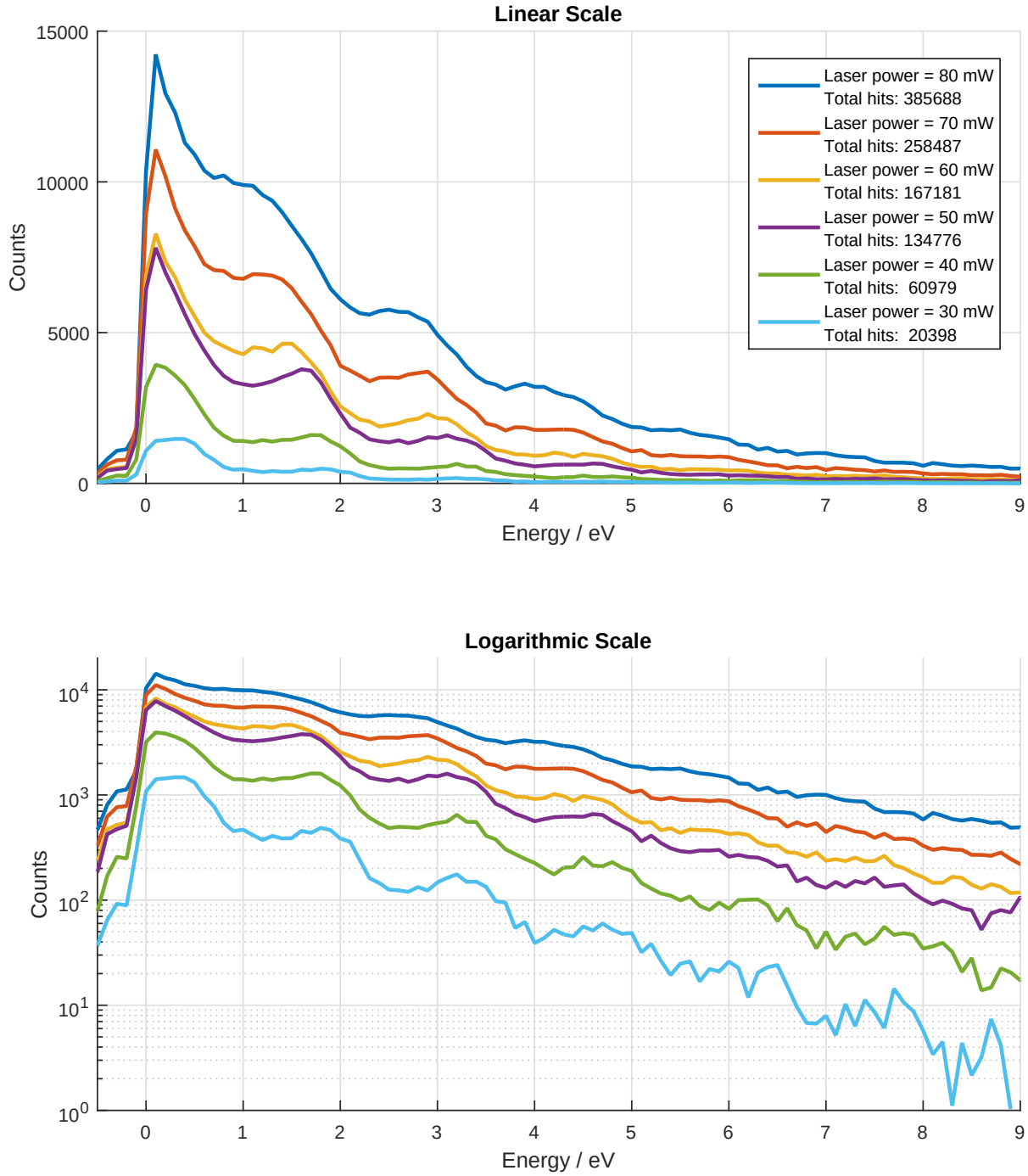

Figure 3.20: Photoelectron spectra of perylene ionized with 800 nm for various laser powers (eiTOF_0547-eiTOF_0553)

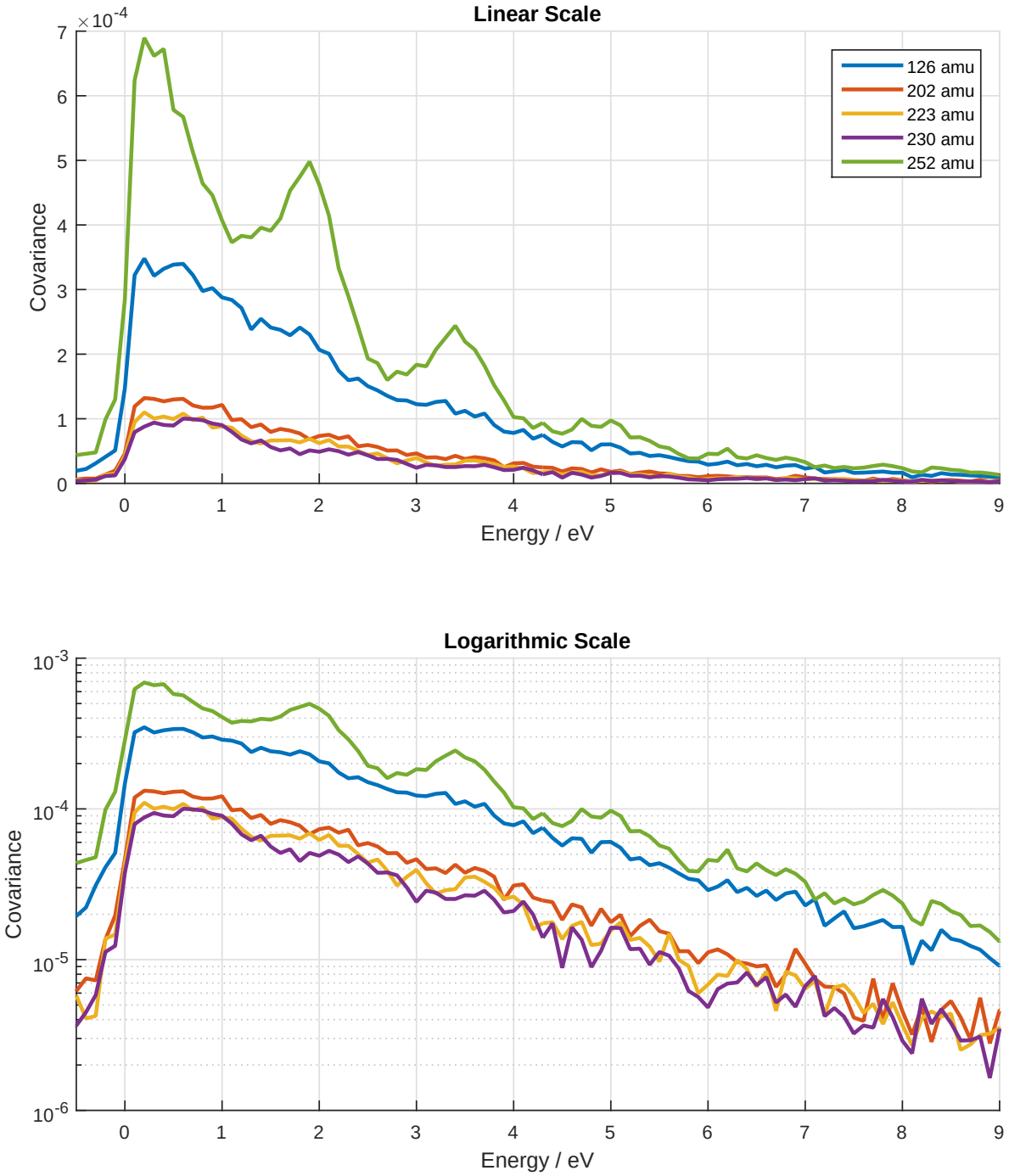

Figure 3.21: PEPICO photoelectron spectra of perylene fragments. Ionization wavelength 800 nm. Laser power: $P = 45\,\mathrm{mW}$. (eiTOF_0440-eiTOF_0444)

Bibliography

[1] P. Maierhofer. Femtosecond Photodissociation Dynamics in Molecules Studied by Time-Resolved Photoelectron-Photoion Coincidence Spectroscopy, 2016. Institute of Experimental Physics, Graz University of Technology

[2] I. V. Hertel, C.-P. Schulz. *Atome, Moleküle und optische Physik 1: Atomphysik und Grundlagen der Spektroskopie.* Springer-Verlag, 2008

[3] S. Larochelle, A. Talebpour, S. Chin. Coulomb effect in multiphoton ionization of rare-gas atoms. *Journal of Physics B: Atomic, Molecular and Optical Physics* **31** (1998) 1215

[4] G. G. Paulus, W. Nicklich, H. Xu, P. Lambropoulos, H. Walther. Plateau in above threshold ionization spectra. *Phys. Rev. Lett.* **72** (1994) 2851.
DOI: 10.1103/PhysRevLett.72.2851

[5] P. B. Corkum. Plasma perspective on strong field multiphoton ionization. *Phys. Rev. Lett.* **71** (1993) 1994.
DOI: 10.1103/PhysRevLett.71.1994

[6] A. E. Boguslavskiy, J. Mikosch, A. Gijsbertsen, M. Spanner, S. Patchkovskii, N. Gador, M. J. Vrakking, A. Stolow. The multielectron ionization dynamics underlying attosecond strong-field spectroscopies. *Science* **335** (2012) 1336

[7] A. Konar, Y. Shu, V. V. Lozovoy, J. E. Jackson, B. G. Levine, M. Dantus. Polyatomic Molecules under Intense Femtosecond Laser Irradiation. *The Journal of Physical Chemistry A* **118** (2014) 11433

[8] P. Sándor, A. Zhao, T. Rozgonyi, T. Weinacht. Strong field molecular ionization to multiple ionic states: direct versus indirect pathways. *Journal of Physics B: Atomic, Molecular and Optical Physics* **47** (2014) 124021

[9] A. Zhao, P. Sándor, T. Rozgonyi, T. Weinacht. Removing electrons from more than one orbital: direct and indirect pathways to excited states of molecular cations. *Journal of Physics B: Atomic, Molecular and Optical Physics* **47** (2014) 204023

[10] J. N. Pitts Jr, F. Blacet. METHYL ETHYL KETONE PHOTOCHEMICAL PROCESSES. *Journal of the American Chemical Society* **72** (1950) 2810

[11] P. Sándor, V. Tagliamonti, A. Zhao, T. Rozgonyi, M. Ruckenbauer, P. Marquetand, T. Weinacht. Strong Field Molecular Ionization in the Impulsive Limit: Freezing Vibrations with Short Pulses. *Physical review letters* **116** (2016) 063002

[12] F. Koberg. *Femtosecond photoelectron and photoion spectrometer*. Bachelor's thesis, Insitute of Experimental Physics, Graz University of Technology, 2015

[13] A. Matsuda, M. Fushitani, C.-M. Tseng, Y. Hikosaka, J. H. Eland, A. Hishikawa. A magnetic-bottle multi-electron-ion coincidence spectrometer. *Review of Scientific Instruments* **82** (2011) 103105

[14] P. Kruit, F. Read. Magnetic field paralleliser for 2π electron-spectrometer and electron-image magnifier. *Journal of Physics E: Scientific Instruments* **16** (1983) 313

[15] T. Tsuboi, E. Y. Xu, Y. K. Bae, K. T. Gillen. Magnetic bottle electron spectrometer using permanent magnets. *Review of scientific instruments* **59** (1988) 1357

[16] M. Koch, T. J. Wolf, J. Grilj, E. Sistrunk, M. Gühr. Femtosecond photoelectron and photoion spectrometer with vacuum ultraviolet probe pulses. *Journal of Electron Spectroscopy and Related Phenomena* **197** (2014) 22

[17] M. Mucke, M. Förstel, T. Lischke, T. Arion, A. M. Bradshaw, U. Hergenhahn. Performance of a short "magnetic bottle" electron spectrometer. *Review of Scientific Instruments* **83** (2012) 063106

[18] P. Lablanquie, L. Andric, J. Palaudoux, U. Becker, M. Braune, J. Viefhaus, J. Eland, F. Penent. Multielectron spectroscopy: Auger decays of the argon 2p hole. *Journal of electron spectroscopy and related phenomena* **156** (2007) 51

[19] V. Stert, W. Radloff, C. Schulz, I. Hertel. Ultrafast photoelectron spectroscopy: Femtosecond pump-probe coincidence detection of ammonia cluster ions and electrons. *The European Physical Journal D* **5** (1999) 97

[20] J. Mikosch, S. Patchkovskii. Coincidence and covariance data acquisition in photoelectron and-ion spectroscopy. I. Formal theory. *Journal of Modern Optics* **60** (2013) 1426

[21] J. Mikosch, S. Patchkovskii. Coincidence and covariance data acquisition in photoelectron and-ion spectroscopy. II. Analysis and applications. *Journal of Modern Optics* **60** (2013) 1439

[22] L. Frasinski, K. Codling, P. Hatherly. Covariance mapping: A correlation method applied to multiphoton multiple ionization. *Science* **246** (1989) 1029

[23] L. Frasinski, M. Stankiewicz, P. Hatherly, G. Cross, K. Codling, A. Langley, W. Shaikh. Molecular H 2 in intense laser fields probed by electron-electron, electron-ion, and ion-ion covariance techniques. *Physical Review A* **46** (1992) R6789

[24] M. D. Hanwell, D. E. Curtis, D. C. Lonie, T. Vandermeersch, E. Zurek, G. R. Hutchison. Avogadro: An advanced semantic chemical editor, visualization, and analysis platform. *J. Cheminformatics* **4** (2012) 17

[25] G. Bieri, F. Burger, E. Heilbronner, J. P. Maier. Valence ionization energies of hydrocarbons. *Helvetica Chimica Acta* **60** (1977) 2213

[26] E. W.-G. Diau, C. Kötting, A. H. Zewail. Femtochemistry of Norrish Type-I Reactions: I. Experimental and Theoretical Studies of Acetone and Related Ketones on the S1 Surface. *ChemPhysChem* **2** (2001) 273

[27] E. W.-G. Diau, C. Kötting, A. H. Zewail. Femtochemistry of Norrish Type-I Reactions: II. The Anomalous Predissociation Dynamics of Cyclobutanone on the S1 Surface. *ChemPhysChem* **2** (2001) 294

[28] E. W.-G. Diau, C. Kötting, T. I. Sølling, A. H. Zewail. Femtochemistry of Norrish Type-I Reactions: III. Highly Excited Ketones-Theoretical. *ChemPhysChem* **3** (2002) 57

[29] T. I. Sølling, E. W.-G. Diau, C. Kötting, S. De Feyter, A. H. Zewail. Femtochemistry of Norrish Type-I Reactions: IV. Highly Excited Ketones-Experimental. *ChemPhysChem* **3** (2002) 79

[30] H. Sakurai, S. Kato. A theoretical study of the Norrish type I reaction of acetone. *Journal of Molecular Structure: THEOCHEM* **461** (1999) 145

[31] E. E. Rennie, A.-M. Boulanger, P. M. Mayer, D. M. Holland, D. A. Shaw, L. Cooper, L. G. Shpinkova. A photoelectron and TPEPICO investigation of the acetone radical cation. *The Journal of Physical Chemistry A* **110** (2006) 8663

[32] M. Nobre, A. Fernandes, F. F. da Silva, R. Antunes, D. Almeida, V. Kokhan, S. V. Hoffmann, N. Mason, S. Eden, P. Limao-Vieira. The VUV electronic spectroscopy of acetone studied by synchrotron radiation. *Physical Chemistry Chemical Physics* **10** (2008) 550

[33] K. Hosaka, R. Itakura, K. Yokoyama, K. Yamanouchi, A. Yokoyama. Photoelectron–photoion coincidence momentum imaging for dissociative ionization of ethanol in intense laser fields. *Chemical Physics Letters* **475** (2009) 19

[34] M. I. Shchuka, A. L. Motyka, M. R. Topp. Two-photon threshold ionization spectroscopy of perylene and van der waals complexes. *Chemical physics letters* **164** (1989) 87

Danksagung

Mein besonderer Dank gilt meinem Betreuer Ass.Prof. Dipl.-Ing. Dr.techn. Markus Koch. Die Art wie ich während der Tätigkeit im Labor und beim Schreiben der Arbeit unterstützt wurde, lässt keine Wünsche offen. Das Abwägen zwischen Kontrolle und Übertragen von Verantwortung beim Bedienen einer sehr komplexen und kostspieligen Apparatur ist ihm aus meiner Sicht perfekt gelungen. Seine Unterstützung im Labor und die ständige Bereitschaft Fragen jedweder Art zu beantworten oder Probleme zu diskutieren waren unerlässlich für das Entstehen dieser Arbeit und machten die Zeit als Diplomand zu dem mit Abstand lehrreichsten Jahr meines bisherigen Lebens.

Für die Möglichkeit am Institut für Experimentalphysik in einem hochmodernen Labor zu arbeiten möchte ich mich bei Herrn Univ.-Prof. Dipl.-Phys. Dr.rer.nat. Wolfgang E. Ernst bedanken. Auch die Einblicke in die aktuelle Forschung auf verschiedensten Gebieten im Zuge der wöchentlichen Forschungsgruppensitzung erweiterten meinen Horizont erheblich.

Einen sehr großen Anteil am Entstehen dieser Arbeit hat mein Laborpartner Paul Maierhofer. Nur durch die Arbeit im Team mit ihm war die Bedienung der Anlage erst möglich. Die Diskussion mit ihm und das gemeinsame Lösen von Problemen in einer sehr harmonischen Atmosphäre ließen die Zeit im Labor wie im Flug vergehen.

Einen weiteren großen Anteil hat Ralf Meyer. Die gute Stimmung im Büro und die Bereitschaft Probleme zu diskutieren und zu deren Lösung beizutragen waren eine große Hilfe.

Bedanken möchte ich mich auch bei Pascal Heim und Bernhard Thaler für deren Hilfsbereitschaft und die gute Atmosphäre im Büro.

Im gesamten Verlauf des Studiums konnte ich mich immer auf eine sehr starke Gemeinschaft von Studienfreunden verlassen. Ohne sie wäre es mir wohl nur sehr schwer möglich gewesen das Studium mit Erfolg zu beenden. Neben den bereits erwähnten Paul Maierhofer und Ralf Meyer möchte ich hier Michael Draxler, Christian Platzer, Michael Rumetshofer, Alexander Schiffmann und Alexander Schossmann nennen und mich für eine sehr schöne Zeit bedanken.

Auch meinen Mitbewohnern während der Studienzeit möchte ich meinen Dank aussprechen. Die Gesellschaft von Eva Platzer, Alexander Robia, Alexander Schiffmann, Christian Strametz sowie Georg Edegger und Katharina Reich trug maßgeblich zu meinem seelischen und körperlichen Wohl in dieser Zeit bei.

Abschließend möchte ich mich bei meiner Familie bedanken. Meine Eltern Angela und Peter sowie meine Schwestern Antonia und Johanna unterstützten mich immer bedingungslos und ermöglichten mir erst das Studium.